Experimental and Modeling Study of Ferrimagnetic Rare-Earth Transition-Metal Thin Films

A Dissertation

Presented to

the faculty of the School of Engineering and Applied Science

University of Virginia

in partial fulfillment

of the requirements for the degree

Doctor of Philosophy

by

Xiaopu Li

May

2017

APPROVAL SHEET

The dissertation

is submitted in partial fulfillment of the requirements

for the degree of

Doctor of Philosophy

AUTHOR

The dissertation has been read and approved by the examining committee:

Prof. S. Joseph Poon
Advisor

Prof. Petra Reinke

Prof. Jiwei Lu

Prof. Leonid V. Zhiglei

Prof. Utpal Chaterjee

Accepted for the School of Engineering and Applied Science:

Craig H. Benson, Dean, School of Engineering and Applied Science

May

2017

CONTENTS

LIST OF TABLES

LIST OF FIGURES

ACKNOWLEDGEMENTS

First and foremost, I would like to express my sincere gratitude to my advisor Prof. S. Joseph Poon for his continuous guidance and outstanding mentorship throughout my graduate study. He has been extremely supportive and encouraging, providing me valuable feedback on my work. Moreover, I have learned a lot from his leadership and enthusiasm for physics, which will benefit me significantly for my future career.

Second, I would like to thank Prof. Jiwei Lu for his stimulating discussions and professional advices. It is his help that makes it possible for me to complete this thesis.

Third, I want to show my gratitude to Prof. Petra Reinke for her selfless service for the Engineering Physics program. I enjoyed the EP program so much and will always be proud of being one of the EP students.

Fourth, I would like to thank the rest of my dissertation committee: Prof. Leonid V. Zhiglei and Prof. Utpal Chatterjee. Thank you for your insightful comments and inspiring questions.

Fifth, my special thank goes to Ms. Kimberly Fitzhugh-Higgins for her ongoing encouragements and timely helps, which make my life and study in UVa much easier.

Sixth, I would like to thank all of the past and present members in Poon’s and Wolf/Lu’s labs, including Dr. Manli Ding, Dr. Di Wu, Dr. Yishen Cui, Dr. Ryan B. Comes, Dr. Nattawut Anuniwat, Dr. Salinporn Kittiwatanakul, Dr. Man Gu, Long Chen, Linqiang Luo, Alex Peterson, Andrew Cheung, Chung T. Ma, Yuhan Wang, Sheng Gao and Xixiao Hu, for making our labs such an enjoyable place to work every day.

Seventh, I am also very grateful to our collaborators Dr. Arun Devaraj and Dr. Steven R. Spurgeon at the Pacific Northwest National Laboratory, and Prof. Howard Sheng from George Mason University.

Eighth, I appreciate the unconditional support from my parents, Hongyan Li and Yujie Zhang, who always encourage me to pursue my dreams bravely.

Finally, my greatest thank goes to my wife, Changji Cao, who accompanied me during the most difficult time. Her love turned my years in Charlottesville into unforgettable memories.

ABSTRACT

As an important class of magnetic materials, ferrimagnets include a variety of substances, ranging from the oldest magnetite (Fe_3O_4) to yttrium-iron garnet (YIG), rare-earth transition-metal (RE-TM) alloy, and compensated Heusler compound. The existence of two or more antiferromagnetically coupled sublattices provides a pathway to tune magnetization via temperature, composition, crystal structure, or even ultrafast laser pulses. This freedom makes ferrimagnetic materials critical components in the state-of-the-art spintronic devices.

In this study, ferrimagnetic thin films, particularly the amorphous RE-TM alloys, were deposited by a magnetron sputtering system. By tuning their compositions, the RE-TM thin films (RE = Gd, Tb, Sm) could effectively exhibit room-temperature compensation and perpendicular magnetic anisotropy (PMA). A thickness dependence of the compensation was revealed experimentally, which implies an existence of growth-induced heterogeneity within the amorphous samples. More interestingly, exchange bias (EB) and bistable magnetoresistance (MR) states have been uncovered in the co-sputtered amorphous Tb(Sm)FeCo thin films. Growth-induced nanoscale phase separation was proposed based on the characterization of transmission electron microscopy (TEM) and atom probe tomography (APT).

With an increasing power of computers, numerical modeling has become an important tool for scientific research that examines physics in complex systems, especially the magnetic systems. In this study, an efficient magnetic modeling package (MMP) was designed and programmed in C++ from the ground up. This modeling package incorporates the atomistic magnetic modeling functionality based on both the Monte Carlo Metropolis sampling and the stochastic Landau-Lifshitz-Gilbert (LLG) equation. Moreover, the package has been extended with the parallel tempering algorithm and the micromagnetic Landau-Lifshitz-Bloch (LLB) algorithm to accommodate larger scale problems.

With the help of the MMP, this study provides more insights into the static properties of the ferrimagnetic RE-TM heterostructures. For example, examination of a depth profile of short-range order, i.e. the relative ratio of RE-TM pairs, generated results consistent with experimental magnetization measurements. Additionally, tunable EB has been demonstrated in the atomistic ferrimagnetic core-and-matrix structure with compatible temperature dependence. Furthermore, a nanoscale phase-separated system has been modeled in the frame of micromagnetism, and this offers agreement with the experimental observations.

Meanwhile, motivated by the recent discovery of all-optical switching (AOS) and Skyrmions in the RE-TM system, the ultrafast magnetization dynamics of the GdFe system was investigated by a phenomenological two-temperature model numerically. Quantitative dependence of the magnetization reversal probability was established in terms of laser fluence, atomic concentration, and Gd-Fe pair ratio. A deterministic reversal was confirmed within a window of these conditions achieving a reversal probability as high as 97%. Finally, an increasing laser fluence threshold has been demonstrated numerically in GdFe multilayers with increasing layer periods. This dynamic study implies a new platform for future ultrafast spintronic devices.

CHAPTER 1 INTRODUCTION

1.1 Motivation

Spintronics, compared to conventional electronics, is the study of manipulating the intrinsic spin of conduction electrons and the associated magnetic moment of solid state devices. Spintronics has grown into one of the most productive areas in modern solid state physics, since its emergence from the discovery of the giant magnetoresistance (GMR) by Albert Fert and Peter Grünberg in 1988.[1,2] By the GMR effect, the relative magnetoresistance (MR) change is as large as 50% compared with the 2-3% change in the anisotropic MR (AMR).[1] The discovery of GMR not only provides a new platform of storage media for industries, but also has inspired further efforts focusing on the investigation of spintronics. One of the most significant results is the tunnel magnetoresistance (TMR) in the early 2000s.[3] With MgO as the tunneling barrier, the TMR of $Co_{20}Fe_{60}B_{20}$/MgO/$Co_{20}Fe_{60}B_{20}$ magnetic tunnel junction (MTJ) can reach as high as 604% at room temperature, which greatly improves the scalability of memory devices. Meanwhile, the concept of the magnetic random access memory (MRAM) was proposed to combine high-speed, non-volatile and ultimate-endurance together using spintronic components, for example MTJs.[4] However, as the demand of storage areal density increases over time, the scalability of MRAM is no longer compatible with the traditional switching mechanism via a magnetic field.

Instead of using magnetic field, a breakthrough within the concept of spin-torque transfer (STT)[5] has been executed by directly applying a spin-polarized current to transfer the spin-torque to the free layer of MTJ and thus rotate its magnetization. Based on this idea, the STT-MRAM can realize higher areal density (1 Gb/cm^2) with much smaller current compared to conventional MRAM.[6] The main challenge for implementing both high-density and fast-speed STT-MRAM is the substantial reduction of the intrinsic current density required to switch the magnetization of the free layer while maintaining enough thermal stability required for long-term data retention. For example an anisotropy energy of $K_u{\sim}40\ k_BT$ is required for a typical 10-year storage.[7] To achieve these goals, materials possessing low magnetization, high spin polarization, low damping constant and high perpendicular magnetic anisotropy (PMA) energy density are highly desired.[8] These necessary elements and needed tests motivate the present research inquiry and applied experimentation of ferrimagnetic thin films.

On the other hand, recent progress of ultrafast magnetization dynamics driven by femtosecond laser pulses provides another switching mechanism in addition to magnetic field and STT. In 1996, Beaurepaire et al. discovered such ultrafast demagnetization.[9] Since then, heat-assisted magnetic recording (HAMR) was proposed to overcome the large magnetic anisotropy of the hard magnetic recording media that has been applied to achieve high areal density and beat the superparamagnetic limit.[10,11] Recently, a completely different idea, all-optical switching (AOS), has been demonstrated in RE-TM alloys.[12–14] Because of the broken symmetry of the ferrimagnetic RE-TM sublattices, especially, due to their distinct demagnetizing time, the magnetization of the RE-TM alloy can be switched solely by femtosecond laser pulses. This interesting phenomenon implies a new pathway for future ultrafast spintronic devices.

Finally, other spintronic techniques have been proposed such as racetrack memory[15] and Skyrmion meory[16–18] for applications of even lower power consumption. For example, as topological-protected solitons, Skyrmions were proved to be stable in two dimensional surfaces. Moreover, it was demonstrated that it is possible to drive them using an ultralow current.[16,17] Very recently, Skyrmions were also discovered in the ferrimagnetic RE-TM alloys, i.e. the GdFe thin films.[18] This discovery opens opportunities to explore new physics as well as ultralow-power spintronic devices.

1.2 Dissertation Outline

This dissertation is composed of eight chapters introduced below. The first chapter introduced the study and offered background information and motivation for this research. Chapter 2 delves further into theory behind ferrimagnetic materials, exchange bias and ultrafast magnetization dynamics. Chapter 3 focuses on experimental techniques related to this study, such as magnetron sputtering, structural characterization, photolithography, and the measurement of magnetic property. In Chapter 4, fundamentals of numerical modeling are introduced including the classical Heisenberg model, Monte Carlo methods, atomistic Landau-Lifshitz-Gilbert algorithm and micromagnetic Landau-Lifshitz-Bloch algorithm. Hereafter, a magnetic modeling package will be introduced to employ in the current study. Test results for amorphous GdFe alloys will be presented and compared to past and current research in the field.

Chapter 5 and 6 will cover both experimental and modeling research progresses on RE-TM thin films in this study. Chapter 5 will focus on the experimental results relating to magnetic anisotropy and magnetization of the RE-TM thin films. A thickness dependence of the saturation magnetization in sputtered TbFeCo films will be highlighted here. Findings here motivates numerical studies based on depth profiles of the short-range order in the sputtered amorphous thin films. Chapter 6 will report on experimental evidence of exchange bias in co-sputtered TbFeCo films due to a nanoscale phase separation. A numerical study of the exchange bias will be demonstrated based on an atomistic ferrimagnetic core-and-matrix structure.

Chapter 7 will provide a modeling research employed in this study for the ultrafast magnetization dynamics of the RE-TM system, in particular, the GdFe thin films. A phenomenological two-temperature model will be introduced in order to characterize the material’s response to ultrafast laser pulses. The reversal probability will then be quantitatively explored for the amorphous GdFe alloys in terms of laser fluence, atomic concentration and Gd-Fe pair ratio. Additionally, Chapter 7 will close with a presentation of numerical results of the GdFe multilayers.

Chapter 8 will finalize the study with a summary of findings and suggestions for future inquiry.

CHAPTER 2 BACKGROUND

2.1 Ferrimagnetic Materials

A ferrimagnet, just like the ferromagnet, is an important class of magnetic materials for practical applications. Historically a ferrimagnet has been understood to represent the oldest magnetic material called *ferrites*, also known as “lodestone.” Ferrimagnetism first got its name in 1948 from the pioneering work of L. Néel.[19] Similar to a ferromagnet, it has spontaneous magnetization and magnetically saturated domains below a certain critical temperature, namely Curie temperature T_C. Magnetic hysteresis also exists in a ferrimagnet by scanning external magnetic fields. However, different from a ferromagnet, a ferrimagnet contains two unequal sublattices that are antiferromagnetcally coupled with each other. This coupling gives rise to unique magnetic properties of ferrimagnets. The most notable feature is the compensation phenomenon. The overall saturation magnetization reduces to zero at a certain temperature T_{comp} because of a complete cancellation of the antiparallel contributions from the two sublattices. Not only for its static magnetization, as will be discussed later, but also T_{comp} is a critical factor for ultrafast magnetization dynamics. Due to the distinct relaxation time of the two sublattices, it is possible to manipulate the ultrafast magnetization behavior and realize all-optical switching (AOS) by femtosecond laser pulses.[14]

Magnetic oxides such as ferrites and garnets are one group of essential ferrimagnets. Perhaps, the most famous ferrite is magnetite (Fe_3O_4), which consists of a spinel structure with iron ions (Fe^{2+} and Fe^{3+}) in two different cation sites, that is, tetrahedral sites and octahedral sites. All Fe^{2+} and half of Fe^{3+} occupy octahedral sites, while the other half of Fe^{3+} occupy tetrahedral sites. There is one uncompensated Fe^{2+} per formula with a moment of 4 μ_B at 0 K.[20] Yttrium-iron garnet (YIG) $Y_3Fe_5O_{12}$ is another example; the five iron ions (Fe^{3+}) occupy two octahedral and three tetrahedral sites coordinated by oxygen. A single uncompensated Fe^{3+} ion per formula exists, which results in a net moment of $5\,\mu_B$ per formula at 0 K.[20] YIG has a very narrow ferromagnetic resonance linewidth, making YIG an excellent material for magneto-optics[21] and ultrafast magnetization dynamics.[22]

Ferrimagnetic phases also occur in several alloy systems, including rare-earth transition-metal (RE-TM) alloys and compensated Heusler compounds. In amorphous RE-TM alloys (RE = Gd, Tb, Dy, Ho, Er, or Tm), the RE and TM sublattices are antiparallel oriented due to their antiferromagnetic coupling.[23,24] However, RE-TM alloys that have a light RE element, for example the well-known permanent magnetic material $SmCo_5$[25], are ferromagnetic where all moments are parallel. Intrinsic perpendicular magnetic anisotropy (PMA) has been observed in amorphous RE-TM thin films. On the other hand, there are many ferrimagnetic compensated Heusler compounds that are desirable for spintronics, for example Mn_3Ga.[26,27] The Mn_3Ga of $L2_1$ Heusler structure is theoretically predicted to be a fully compensated half-metallic ferrimagnet. However, the tetragonal distortion from synthesis results in a net magnetic moment of $1.7\,\mu_B$ per formula. Furthermore, this tetragonal distortion also induces PMA in the epitaxial Mn_3Ga thin films, which makes it promising for low-current spintronic devices.

The present study primarily focuses on the ferrimagnetic RE-TM alloys. These materials have been actively examined for their applications in the magneto-optical recording due to the intrinsic PMA in thin films.[28] Recently, the RE-TM alloys have been investigated for the perpendicular magnetic random access memory (p-MRAM), which is considered to be a universal memory technology due to low-power consumption and the non-volatility.[29] For example, it has been reported the amorphous TbFeCo has been used in a perpendicular magnetic tunnel junction (p-MTJ).[30] However, the origin of the intrinsic PMA in RE-TM alloys remains under debates. Various structural characteristics have been proposed including columnar textures[31], micro-crystallinity[32], and local bonding anisotropy[33–35]. Harris and Pokhil suggest that PMA energy increases exponentially with the pair-order anisotropy, i.e. the difference in the number of Fe-Fe pairs between the in-plane and out-of-plane directions.

2.2 Exchange Bias Effect

Exchange bias (EB), first discovered by Meiklejohn in 1956[36], explains a phenomenon in which the hysteresis loop is shifted with respect to the zero magnetic field axis. This effect is associated with an exchange anisotropy, which is created at the interface.[37] Generally, the exchange anisotropy can be induced by an uncompensated exchange coupling between antiferromagnetic (AFM) and ferromagnetic (FM) material, e.g. Co/CoO[38] and Co/IrMn[39]. In a very intuitive picture, when the FM/AFM material is cooled through the Néel temperature of the AFM, the uncompensated interfacial moment of AFM will create an additional unidirectional anisotropy, i.e. the exchange anisotropy. However, experimental observation differs from the predictions of this simple model by orders of magnitude. In order to overcome such a discrepancy, interfacial domains have been proposed to weaken AFM coupling.[40] Moreover, the existence of induced ferromagnetism in the AFM layer has been experimentally revealed in various EB systems.[41–43]

In addition to the FM/AFM systems, the EB effect has also been reported in FM/ferrimagnetic (FI)[44,45], FI/AF[46], and FI/FI systems[47], where a magnetically compensated material is usually involved. For example, exchange-biased hysteresis loops have been observed in compensated ferrimagentic Heusler alloys, e.g. Mn-Pt-Ga.[48] The compensated $Mn_{2.41}Pt_{0.59}Ga$ provides an effective AFM matrix, where FM clusters are embedded due to the compositional fluctuation. A similar example can be found in the compounds of Ni-Mn-X (X = Sn, In, Sb), which also shows an intrinsic EB caused by FM and AFM regions within the material.[49,50]

The EB effect has been employed in many areas, such as with permanent magnets[51], magnetic recording media/head[52], and more importantly, giant magnetoresistance (GMR) multilayers[1,53]. As an example, typical GMR multilayers or a spin-valve structure consists of a FM free layer, e.g. NiFe, a non-magnetic interlayer, e.g. Cu, and another FM pinning layer, e.g. NiFe, that is pinned by a strong exchange anisotropy resulted from an adjacent AFM layer, e.g. FeMn. The exchange-biased pinning effect makes it possible to observe the GMR in a reduced saturation field, which is highly desirable for technological applications. Therefore, a robust and tunable EB becomes crucial for spintronic devices, e.g. MRAM.

The present study focuses on ferrimagnetic RE-TM systems, where the EB effect has been observed in layered thin films. For example, an exchange-biased training effect was reported in the TbFe/GdFe bilayers, where a soft GdFe layer is antiferomagnetically coupled to a hard TbFe layer.[54] Moreover, a tunable perpendicular EB was found in $DyCo_5/Ta/Gd_{24}Fe_{76}$ by varying the thickness of the sandwiched Ta layer.[55] Both of them demonstrate a flexibility of RE-TM materials in controlling EB at room temperature for practical spintronic devices.

2.3 Ultrafast Magnetization Dynamics

Ultrafast magnetization dynamics induced by femtosecond laser pulses has been studied intensively since the discovery of subpicosecond demagnetization by a 60 fs laser pulse by Beaurepaire et al.[9] The demands for ultrafast information process and storage have triggered research of new methods to control magnetization by means other than magnetic field and spin-polarized current. The time scale of magnetization dynamics ranges from billions of years for geological events to femtosecond regime of spin exchange interaction. As demonstrated in Figure 2.1, given that the magnetic precession has a time scale of 100-1000 ps, the ultrafast interaction induced by femtosecond laser pulses provides possibilities to manipulate spins in a time shorter than the processional period.[56]

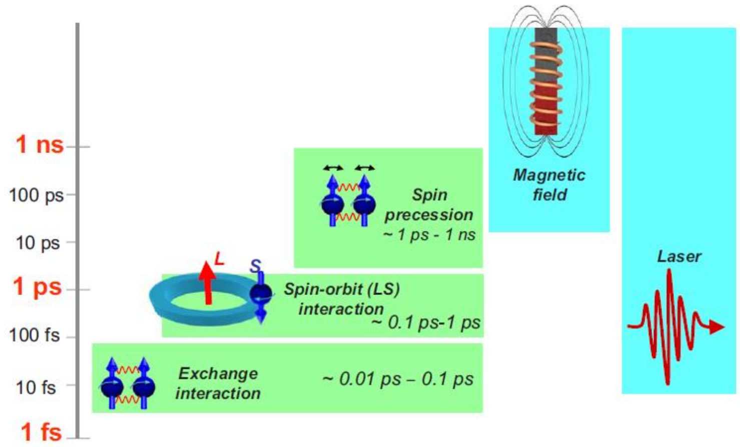

Figure 2.1. Time scales in magnetism as compared to magnetic field and laser pulses. From Kirilyuk et al.[56]

A remarkable feature of the femtosecond time regime is that the whole magnetic system can be divided into dynamically isolated reservoirs of spins, electrons and phonons. The dynamic problem is to investigate energy and angular momentum transfer among different thermodynamic reservoirs.[57] Further research has revealed that excitation caused by a femtosecond laser pulse kicks a magnetic system into a highly non-equilibrium state, where the conventional thermodynamics is no longer valid. When the time scale becomes shorter, stronger interactions such as spin-orbit coupling or even exchange interaction should be considered time-dependent.

The thermal effect of an ultrashort laser pulse on metals can be distinguished across four stages as shown in Figure 2.2. Laser energy is absorbed by the conduction band electrons in the first stage, leading to a deviation from the equilibrium density of states of Fermi-Dirac distribution. In the second stage, immediately after the laser excitation thermalization of the electron reservoir starts through the collisions of the excited electrons. Thermal equilibrium of electrons can be established within tens of femtoseconds. Electron-phonon coupling then becomes effective in the third stage due to a strong non-equilibrium between electron and lattice temperature, leading to energy transfer from electrons to lattice or phonons. The third stage can last tens of picoseconds depending on the electron-phonon coupling strength. Transition metals generally have greater electron-phonon coupling than that of noble metals.[58] After the thermal equilibrium of electrons and lattice, heat energy will finally be transferred from surface to deeper part of the sample. This transfer happens as a result of temperature gradient during the last cooling stage.

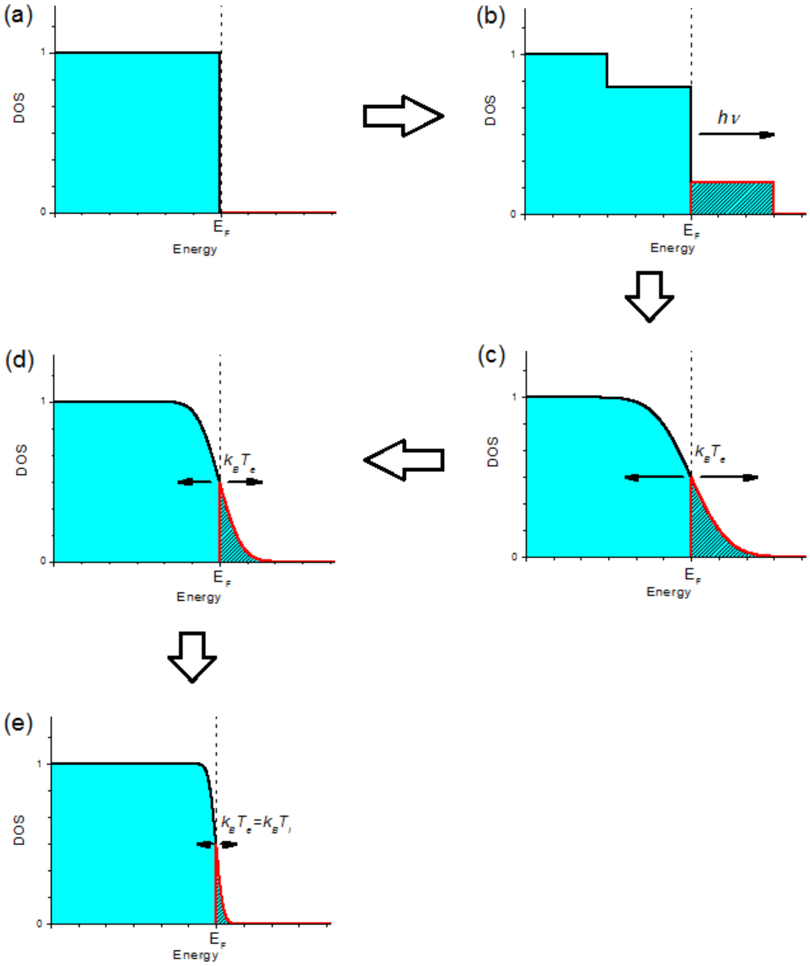

Figure 2.2. Four stages of the relaxation of electrons in metals irradiated by a femtosecond laser pulse. Schematic drawing is replotted from Wu et al.[59], and based on the discussion of Hohlfeld et al.[60]

For elementary metallic ferromagnets, ultrafast demagnetization has been studied by femtosecond laser pulses experimentally.[9,61,62] For example, Ni has a sub-100 fs demagnetizing time, which was first discovered by the time-resolved magneto-optical Kerr effect (TRMOKE)[9], and latterly confirmed by other alternative techniques, such as time- and spin-resolved photoemission (TSPE)[63] and X-ray magnetic circular dichromism (XMCD)[64]. A similar demagnetizing time has been found for all other elementary ferromagnetic transition metals including Co and Fe. Theoretically, a phenomenological three-temperature model was introduced by Beaurepaire et al. to better understand the microscopic mechanism of rapid demagnetization.[9] On the other hand, the ferromagnetic Gd exhibits a contrasting time scale of 40 ps by TSPE.[65] The discrepancy was further examined by Koopmans et al., who proposed another relaxation mechanism based on electron-phonon-mediated spin-flip scattering.[66]

More importantly, another area, namely all-optical switching (AOS), has been triggering intensive interests in the field of the ultrafast magnetism. Within concept of AOS, magnetic information is controlled purely by a femtosecond laser without any magnetic field or switching current. AOS was first demonstrated in the amorphous GdFeCo thin film by a circularly polarized laser in 2007 by Stanciu et al.[67] As previously discussed, this phenomenon has been explained by the broken symmetry of the ferrimagnetic RE-TM system, where the Gd and FeCo sublattices have significantly different demagnetizing time scales. AFM coupling, non-equivalent sublattices and PMA have been highlighted as practical rules for designing AOS devices.[68] Moreover, AOS has also been revealed in several synthetic ferrimagnets, e.g. $[\mathrm{Co/Ir/Co}]_N$ and $[\mathrm{Co/Ir/CoNiPtCo/Ir}]_N$, which provides examples for engineering AOS in a general way.[14] Most recently, a breakthrough was made by Lambert et al.[69], who found AOS to be exhibited in the state-of-art granular FePt hard disc material. The large PMA of FePt offers potential for future high-density AOS memory devices.

CHAPTER 3 EXPERIMENTAL TECHNIQUES

3.1 Introduction

This chapter outlines a brief description of experimental techniques used for the development and characterization of amorphous thin films. All the films in the present study were deposited using a radio frequency (RF) magnetron sputtering system. The sputtering tool provides rapid and repeatable depositions of amorphous thin films. The film thickness was determined by X-ray reflectometry (XRR). Atomic force microscopy (AFM) was employed to characterize the film surface morphology. Structural characterization of these sputtered films were performed by high resolution transmission electron microscopy (HRTEM) and atom probe tomography (APT). Both vibrating sample magnetometer (VSM) and magneto-optical Kerr effect (MOKE) were used to characterize magnetic properties of the films. Furthermore, Hall bar devices were fabricated on the films through photolithography. Magneto-transport properties were measured by anomalous Hall effect (AHE) and magnetoresistance (MR) of the Hall bar devices.

3.2 Magnetron Sputtering Deposition

Magnetron sputtering is one of the most commonly used physical vapor deposition (PVD) approaches for thin film fabrication. It is similar to other basic sputtering systems, which initiate sputtering by applying an electric field between the target (cathode) and the substrate (anode). Specifically, stray electrons near the target are accelerated toward the substrate under an electric field. Process gas atoms are ionized with accumulated charges while they collide with electrons. Meanwhile, as the ions collide with the target, secondary electrons are ejected contributing to charge multiplication, which plays an important role in maintaining plasma. A discharge finally occurs with a large avalanche current. Stable sputtering is established when enough ions begin to bombard the target.

Unlike the basic sputtering systems, in magnetron sputtering, a magnetic field is employed in close proximity to the target surface parallelly to achieve better secondary electron confinement.[70] The ionization efficiency of the gas atoms is greatly improved by the helical motion of the trapped electrons in the magnetic field during sputtering. Compared with other sputtering techniques, magnetron sputtering operates at lower operating pressure (~ 10^{-3} mbar) thus avoiding intense gas collisions and scatterings. Therefore, a stable plasma with a moderate growth rate can be maintained with a relatively low target voltage (~ 500 V).[71]

In the present study's magnetron sputtering system, as shown in Figure 3.1, the main process chamber is connected to a cryo-pump to maintain a base pressure below 1×10^{-6} Torr. The main chamber accommodates four targets, three of which are operated with a RF power supply while the fourth one can be applied with both a direct current (DC) and RF bias. Argon is used as the process gas and the process pressure falls within the range of a few millitorrs. The power of each target can be adjusted to control the growth-rate of the corresponding material or to modify the film composition in a co-sputtering process. A load lock chamber is connected to a turbo pump.

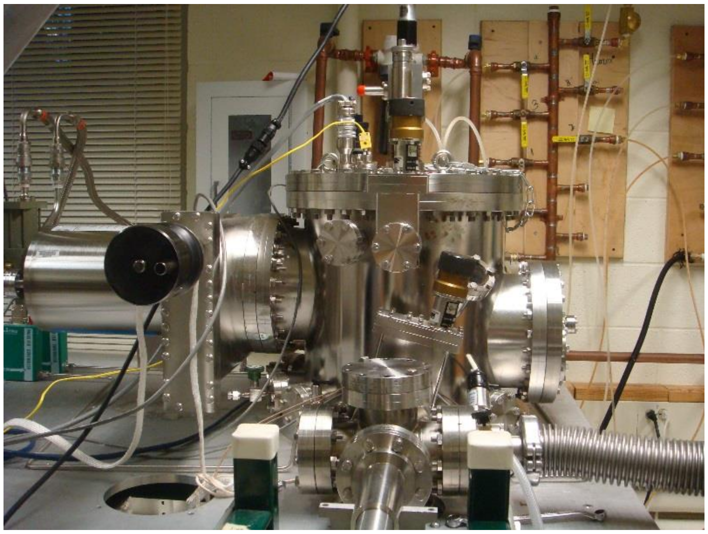

Figure 3.1. The magnetron sputtering system used in the present study.

In the present study, standard single-side thermal oxide silicon wafer was generally used as sputtering substrate. To provide amorphous as-deposited films, all depositions were proceeded with water-cooled substrate holder at an ambient temperature. The growth-rates for various materials at different sputtering conditions were determined by depositing fairly thick films for the thickness measurement, and X-ray reflectometry was used to measure the thickness. Once sputtering rates were calculated from these thicknesses, the deposition time for various films were then calculated for the same power and pressure condition. Finally, a 5 nm thick Ta layer was capped on film surface to protect it from oxidation.

3.3 Structural Characterization Tools

3.3.1 X-Ray Reflectometry (XRR)

X-ray reflectometry (XRR) is a widely used analytical technique for thin film characterization. XRR can be performed by most standard X-ray diffraction (XRD) systems. During an XRR measurement, a small-angle incident X-ray beam is reflected by the flat surface of the sample film, and its intensity (or reflectivity) is measured by an X-ray detector in the specular direction (i.e. symmetric incident and reflected angles). Theoretically, the specular profile of the reflectivity is a combination of Fresnel reflectivity and Kiessig interference fringes.[72] By fitting experimental reflectivity profile, several useful structural parameters can be obtained, such as interfacial roughness, layer thickness, and material density, as is shown in Figure 3.2.

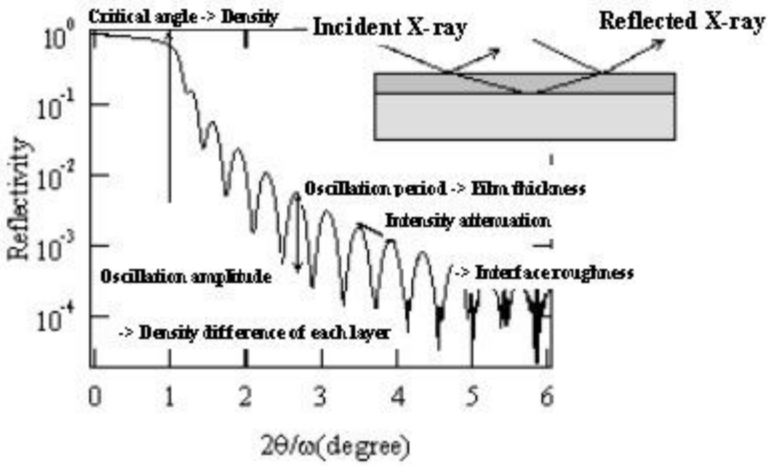

Figure 3.2. Relationship between a profile of X-ray reflectivity and structural parameters. From Rigaku.

A Rigaku SmartLab® XRD system was used for all XRR characterizations in this research. The X-ray source was operated at an accelerating voltage of 44 keV and 40 A. Cu *K*α radiation was used with a wavelength of 1.541 Å. A Ge(2×220) crystal mirror monochromator was used for high resolution X-ray experiments.

3.3.2 Transmission Electron Microscopy (TEM)

Transmission electron microscopy (TEM) is a microscopy technique in which a high-energy electron beam is transmitted through an ultra-thin specimen. TEM is capable of imaging at a significant high resolution, e.g. 0.2 nm, owing to the small de Broglie wavelength of electrons. In this study, high-resolution (HR) TEM was performed by FEI’s Titan S/TEM at 300 keV to characterize structures of sputtered thin films.

Cross-sectional TEM samples were prepared through the following procedure:

1. Cut two plates out of original thin film with a dimension of 10 mm × 3 mm × 0.69 mm.

2. Bond these two plates face-to-face using Hardman DOUBLE/BUBBLE® Red Epoxy. Cure the epoxy for two days.
3. Cut the “sandwich” plate in to 1 mm × 3 mm × 1.4 mm pieces by a wired saw.
4. Mount one of the small pieces onto a Fischione grinding stage with Krazy® Glue.
5. Grind the specimen down to 200 µm using a Fischione specimen grinder Model 160.
6. Remove the specimen from the stage by immersing it in Acetone for about 40 minutes.
7. Bond the specimen to a TEM copper grid using Hardman DOUBLE/BUBBLE® Red Epoxy. Cure the epoxy for 8 hours.
8. Mount the copper grid to a Fischione grinding stage with a tiny amount of Krazy® Glue.
9. Continue to polish the specimen until it reaches 30 µm.
10. Dimple the center of the specimen by a Fischione dimpling Grinder Model 200.
11. Remove the copper grid from the stage by immersing it in Acetone for about 40 minutes.
12. Ion-mill the center until penetration at low kV at -170 ° C using a Gatan 691 Ion Mill.

Cross-sectional specimens were also shipped to the research collaborators at the Pacific Northwest National Laboratory (PNNL) for further scanning TEM (STEM) studies. Specifically, the specimen were plasma-cleaned for 2 - 5 minutes prior to being inserted in the microscope. High-angle annular dark field (STEM-HAADF) images were collected using an aberration-corrected JEOL ARM 200CF STEM operating at 200 keV with a 27.5 mrad convergence angle and a 54 mrad collection angle. STEM-EDS maps were collected at 256 × 192 resolution with a 2 ms dwell time. The maps were then processed using the JEOL Analysis Station software to remove background and deconvolute peaks.

3.3.3 Atom Probe Tomography (APT)

Atom probe tomography (APT) is the only material analysis technique that offers extensive capabilities for both 3D imaging and chemical composition measurements at the atomic scale (0.1 - 0.3 nm in depth and 0.3 - 0.5 nm laterally).[73–75] The specimen is prepared by being shaped into a very sharp tip. During the process of APT, the tip is cooled down to a low temperature and biased by a high DC voltage, which induces a significant electrostatic field just below the point of atom evaporation. Then, one or more atoms is evaporated out of the tip surface by an external laser pulse and projected onto a position-sensitive detector. Finally, the tomography is reconstructed based on the detected position and the time-of-flight for each of the atoms, as shown in Figure 3.3.

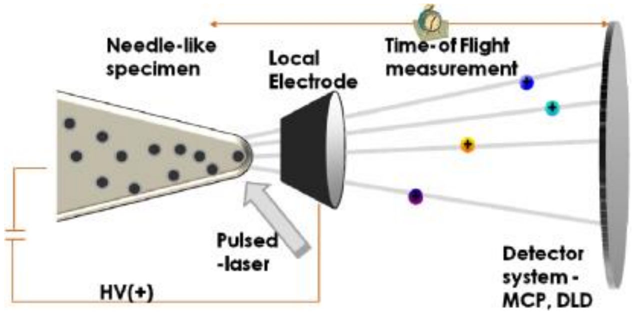

Figure 3.3. Atom probe tomography flow diagram. From Kuchibhatla et al.[76]

APT measurements in this study were completed by research collaborators at PNNL. Specifically, needle-shaped specimens for APT was prepared using a conventional lift-out method and annular milling using an FEI Helios Nanolab 600 dual-beam focused ion beam system. Laser-assisted APT experiments were conducted using a CAMECA LEAP4000XHR system with 20 pJ laser pulse energy, 200 KHz pulse repetition rate, 0.005 atoms per pulse evaporation rate and a 40 K specimen temperature. APT results were reconstructed using IVAS 3.6.6 reconstruction software.

3.4 Photolithography Techniques

The present study employed photolithography techniques including photoresist patterning and dry/wet Etching to fabricate Hall bar devices on thin films. These procedures were performed at the University of Virginia Microfabrication Laboratories (UVML), which serves as the university's center for research and development in solid-state materials, devices and circuits.

3.4.1 Photoresist Patterning

In photolithography, a geometric pattern is transferred from a photomask to a layer of photoresist on the sample surface. Two types of photoresist were used in this study: positive photoresist AZ® 4210 and negative photoresist AZ® nLOF2020. Photoresist that is sensitive to ultraviolet (UV) light was exposed by a SUSS MicroTec Mask Aligner. After being exposed, it was developed by certain chemicals to either maintain (positive) or remove (negative) the exposed patterns.

3.4.2 Dry / Wet Etching

After patterning photoresist, thin films have to go through an etching procedure to remove materials that are not protested by photoresist. This is the most critical part in the Hall bar fabrication process. In this study, a combination of dry and wet etching was performed to effectively remove the Ta capping layer.

During dry etching, the unprotected pattern is removed by a bombardment of ions. All dry etching in the present study were performed by Trion dry etching equipment. Both inductively coupled plasma (ICP) and reactive ion etching (RIE) were used to obtain the optimal removal. Tetrafluoromethane (CF_4) was selected to be used as the reactive gas. After dry etching, a wet etching was used to remove the remaining materials. In this study, a diluted hydrochloride (HCl) acid was selected to react with RE-TM thin films within a reasonable amount of time.

3.4.3 Hall Bar Fabrication Recipe

To study magneto-transport properties of RE-TM thin films, Hall bar devices were fabricated based on the following recipe:

1. Clean the thin film sample by isopropanol (IPA), methanol and deionized (DI) water.
2. Spin positive photoresist AZ® 4210 on the sample at 4000 rpm for 30 seconds.
3. Bake the photoresist at 100° C for 1 minute.
4. Expose the photoresist for 36 seconds using an UV of 275 W.
5. Develop the photoresist using AZ® 400K (1:4 by DI water) for about 40 seconds.
6. Dry-etch the sample using a Trion ICP/RIE etching tool. An example of etching parameters are listed in Table 3.1.

Table 3.1. Dry etching parameters by Trion ICP/RIE etching tool. Use the default units displayed by the Trion ICP/RIE etching tool.

Pressure	**ICP**	**ICP Ref**	**RIE**	**RIE Ref**	**DC**	**CF_4**	**Time**
150	41	2	70	3	-105	50	15 minutes

7. Wet-etch the sample with diluted HCl acid. Examples of dilution and etching time are listed in Table 3.2.

Table 3.2. Dilution of HCl acid and etching time during wet etching.

Sample thickness (nm)	Dilution by DI water	Time (s)
103 (TbFeCo)	1:300	270
102 (TbSmFeCo)	1:300	330
15 (TbFeCo)	1:9600	20

8. Wash the sample using Acetone, IPA and DI water.
9. Spin negative photoresist AZ® nLOF2020 on the sample at 5500 rpm for 30 seconds.
10. Bake the photoresist at 100° C for 1 minute.
11. Expose the photoresist for 6 seconds using an UV of 275 W.
12. Bake the photoresist again at 110° C for 1 minute.
13. Develop the photoresist using AZ® 300 MIF for about 30 seconds.
14. Electron-beam evaporate 20 nm of Ti at a deposition rate of 2 Å/s and 150 nm gold at 2 Å/s.

Figure 3.4 shows an example of the fabricated Hall bar device.

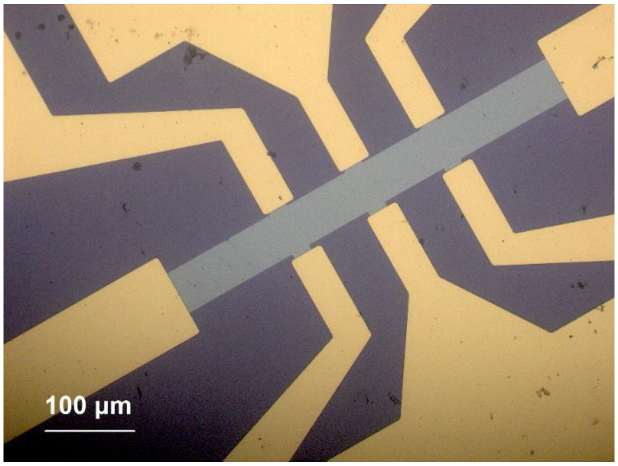

Figure 3.4. Optical microscopy image of a fabricated Hall bar device on a 15 nm TbFeCo thin film.

3.5 Measurements of Magnetic Properties

3.5.1 Vibrating Sample Magnetometer (VSM)

A vibrating sample magnetometer (VSM), invented in 1955 by Simon Foner at Lincoln Laboratory MIT[77], has been widely used to accurately measure magnetic moments of a small sample. As demonstrated in Figure 3.5, the sample is placed and vibrated sinusoidally inside a uniform magnetic field generated by either an electromagnet or a superconducting magnet. The induced voltage signal collected by the pickup coils is proportional to the sample's magnetic moment.

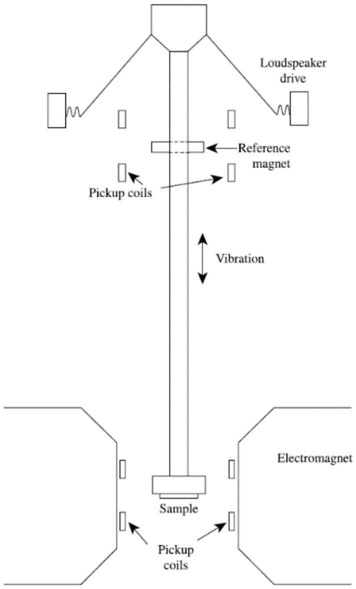

Figure 3.5. Vibrating sample magnetometer (schematic). From Cullity et al.[78]

Considering the acuity of Foner's VSM, the VSM functionality of the Quantum Design VersaLab™ system was used to measure magnetic moment of the thin film samples in the present study. This particular model is capable of a maximum field of 3 Tesla and a large temperature range from 50 K to 400 K. Both in-plane and out-of-plane hysteresis loops were respectively measured with specially designed in-plane and out-of-plane sample holders.

3.5.2 Magneto-Optical Kerr Effect (MOKE)

Based on the magneto-optical Kerr effect (MOKE), a phase difference exists between the incident-polarized laser beam and that which was reflected from a magnetic surface. In the present study, the sputtered sample has a flat and smooth surface. With these specifications, MOKE, especially the polar MOKE has been used to quickly characterize the hysteresis loop shape of the samples with perpendicular magnetic anisotropy at room temperature. As shown in Figure 3.6, a home-made equipment was used to measure MOKE on an optical stage.

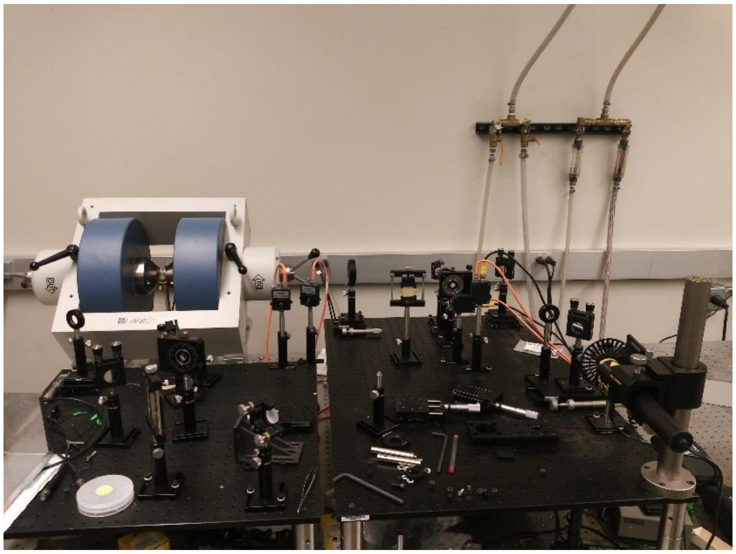

Figure 3.6. A home-made equipment for MOKE measurements.

3.5.3 Magneto-Transport Measurements

As an alternative way to characterize magnetic properties, magneto-transport measurements are generally performed on small scale solid-state devices such as Hall bars and magnetic tunnel junctions. Two types of magneto-transport properties were characterized on the Hall bar devices in this study: anomalous Hall effect (AHE) and magnetoresistance (MR).

Based on AHE, the Hall resistivity consists of an ordinary Hall component and an additional Hall component. The latter directly depends on the magnetization of the magnetic material and is often much larger than the ordinary Hall component. This extraordinary large Hall resistivity or AHE, provides an alternative method to characterize magnetization of the micron-size Hall bar device.

In this study, both AHE and MR were performed by the electrical transport option (ETO) of the Quantum Design VersaLab™. As shown in Figure 3.7, the current was supplied through Contact A and Contact B. The external magnetic field was exerted in a manner perpendicular to the sample surface. In a typical AHE measurement, the voltage difference between Contact C and Contact D was detected to calculate the Hall resistivity. On the other hand, Contact E and Contact F were selected for a typical MR measurement.

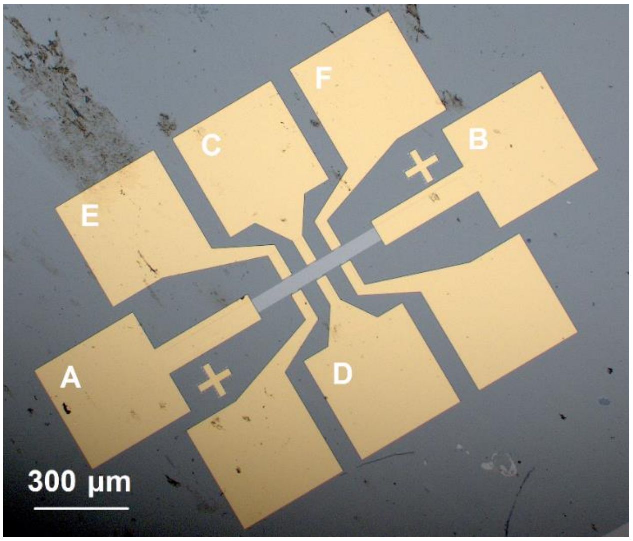

Figure 3.7. Optical microscopy image of a Hall bar device and contact arrangement.

CHAPTER 4 MODELING METHODS

4.1 Introduction

With the growing power of modern computers, numerical modeling has become an essential tool for scientific research, especially when handling systems as complex as magnetic devices. For magnetic modeling, there are many methodological choice in terms of different dimensions and time scales. This chapter will first introduce the theoretical basics of magnetic modeling. Next, it will introduce the classical atomistic Heisenberg model. The third section will then describe algorithms based on Monte Carlo sampling, which is very efficient for simulating static magnetic properties. The next two sections will provide an outline of the fundamentals of the dynamical atomistic Landau-Lifshitz-Gilbert (LLG) and micromagnetic Landau-Lifshitz-Bloch (LLB) algorithms. The last two sections will focus on the empirically programmed Magnetic Modeling Package (“MMP”) used for this study and testing cases on the amorphous GdFe system.

4.2 Classical Atomistic Heisenberg Model

4.2.1 Ising Model

The simplest magnetic model is the Ising model[79], where each spin is represented by a scalar with only two discrete values of +1 and -1. A typical Ising Hamiltonian is expressed as

$$\mathcal{H}(\sigma) = -\frac{1}{2}\sum_{\langle i,j\rangle} J_{ij}\sigma_i\sigma_j - \sum_i \mu_i h_i \sigma_i \tag{4.1}$$

Where J_{ij} is the nearest neighbor exchange constant between the site i and j, σ_i is the spin scalar at the site i, μ_i is the local magnetic moment, and h_i is the external magnetic field. Despite the Ising model’s simplicity, it successfully describes the physics of magnetic phase transitions and is thus an important model theoretically speaking. However, due to the binary quantization of spin states, the Ising model treats magnetic anisotropy as infinity equivalently, which limits its application in modeling real materials.

4.2.2 Classical Atomistic Heisenberg Model

Another traditional model is the classical atomistic Heisenberg Hamiltonian, or Heisenberg model for short, demonstrated in the following equation.[80]

$$\begin{aligned}\mathcal{H}(\boldsymbol{S}) = -\frac{1}{2}\sum_{\langle i,j\rangle} J_{ij}\boldsymbol{S}_i\cdot\boldsymbol{S}_j - \sum_i D_i(\boldsymbol{S}_i\cdot\boldsymbol{n}_i)^2 \\ -\frac{1}{2}\sum_{i\neq j}\frac{\mu_0\mu_i\mu_j}{4\pi R_{ij}^3}\left(3(\boldsymbol{S}_i\cdot\widehat{\boldsymbol{R}}_{ij})(\boldsymbol{S}_j\cdot\widehat{\boldsymbol{R}}_{ij}) - \boldsymbol{S}_i\cdot\boldsymbol{S}_j\right) \\ -\sum_i \mu_0\mu_i\boldsymbol{S}_i\cdot\boldsymbol{H}\end{aligned} \tag{4.2}$$

$\boldsymbol{S}_i$ represents the spin at site i and is normalized to a unit vector. There are four terms within the Hamiltonian in total. The first term describes the exchange interaction between all nearest neighbors. J_{ij} is the isotropic exchange constant between the site i and j. For ferromagnetic coupling ($J_{ij} > 0$), neighboring spins tend to align parallel with each other, whereas, for antiferromagnetic coupling ($J_{ij} < 0$), anti-parallel spin pairs are more preferable with lower interaction energy. Compared to the Ising model, the second term of the Heisenberg model considers the magnetic anisotropy in a more realistic way. Here, a standard uniaxial anisotropy is treated with a local uniaxial anisotropy constant (D_i) and its orientation $\boldsymbol{n}_i$. The third term provides the effect of the dipolar interaction of atomic moments, where μ_i is the atomic moment and $\boldsymbol{R}_{ij}$ is the displacement from site i to site j. Since the demagnetizing field is usually relatively small, this term is generally ignored in atomistic simulations. The last term addresses the Zeeman energy of the system in an external field ($\boldsymbol{H}$).

4.2.3 Mean Field Theory of Ferromagnetic System

Consider a simplified ferromagnetic Hamiltonian with only exchange and Zeeman interaction as:

$$\mathcal{H} = -\frac{1}{2}\sum_{\langle i,j\rangle} J_{ij}\boldsymbol{S}_i \cdot \boldsymbol{S}_j - \mu\boldsymbol{H} \cdot \sum_i \boldsymbol{S}_i \tag{4.3}$$

Define an average spin or spin polarization as $\boldsymbol{m} \equiv \langle \boldsymbol{S} \rangle$ and the difference between the spin vector and spin polarization as $\delta\boldsymbol{S} \equiv \boldsymbol{S} - \boldsymbol{m}$. The Hamiltonian can be further simplified by employing a mean field assumption:

$$\mathcal{H} = -\frac{1}{2}\sum_{\langle i,j\rangle} J_{ij}\left(\boldsymbol{m}_i \cdot \boldsymbol{m}_j + 2\boldsymbol{m}_j \cdot \delta\boldsymbol{S}_i\right) - \mu\boldsymbol{H} \cdot \sum_i \boldsymbol{S}_i \tag{4.4}$$

By defining an effective mean field or mean field as:

$$\boldsymbol{H}_{eff}^{i} \equiv \frac{1}{\mu}\sum_{j=i\ n.n.} J_{ij}\boldsymbol{m}_j + \boldsymbol{H} \tag{4.5}$$

A new Hamiltonian can be derived that only depends on the mean field and spin polarization:

$$\mathcal{H}_{MFT} = \frac{1}{2}\sum_{\langle i,j\rangle} J_{ij}\boldsymbol{m}_i \cdot \boldsymbol{m}_j - \mu\sum_i \boldsymbol{S}_i \cdot \boldsymbol{H}_{eff}^{i} \tag{4.6}$$

Since the spins interact with each other only via the mean field, the original many body problem is now reduced to a combination of single body problems. The partition function of each single body problem is written as:

$$Z_i = \int d^3S_i \exp\left(\beta\mu\left(\boldsymbol{S}_i \cdot \boldsymbol{H}_{eff}^{i}\right)\right) = \frac{4\pi\sinh\left(\beta\mu H_{eff}^{i}\right)}{\beta\mu H_{eff}^{i}} \tag{4.7}$$

Furthermore, the spin polarization is thermodynamically calculated as:

$$\boldsymbol{m}_i = Z_i^{-1}\int d^3S_i\boldsymbol{S}_i \exp\left(\beta\mu\left(\boldsymbol{S}_i \cdot \boldsymbol{H}_{eff}^{i}\right)\right) = B(\beta\mu H_{eff}^{i})\frac{\boldsymbol{H}_{eff}^{i}}{H_{eff}^{i}} \tag{4.8}$$

Where the Langevin function is defined as $B(x) \equiv \coth(x) - \frac{1}{x}$. For a homogeneous system at equilibrium, the ferromagnetic mean field is expressed as:

$$\boldsymbol{H}_{eff} = \frac{zJ}{\mu}\boldsymbol{m} + \boldsymbol{H} \tag{4.9}$$

Where z is the coordination number of this system. If substituting Equation 4.9 to 4.8, a self-consistent equation has to be satisfied:

$$m = B(\beta(zJm + \mu H)) \tag{4.10}$$

Particularly, spontaneous polarization can be calculated with a zero external field. The Curie temperature is theoretically predicted as:

$$T_C^{MFT} = \frac{zJ}{3k_B} \tag{4.11}$$

However, it should be noted that the mean field assumption overestimates the value of the Curie temperature due to an inaccuracy in the consideration of the correlations between spins. Other approaches such as the classical spectra density method and the high temperature expansion method can provide further corrections, for example in simple cubic (SC) and face-centered cubic (FCC) lattices:

$$T_C^{SC} = 1.44\frac{J}{k_B} \tag{4.12}$$

$$T_C^{FCC} = 3.18\frac{J}{k_B} \tag{4.13}$$

4.2.4 Effective Field of Classical Atomistic Heisenberg Model

Similar to the mean field theory, an effective field should be calculated at a specific site for the Heisenberg model. As is well-known, the effective field is generally defined as the negative first derivative of Hamiltonian to a specific spin or magnetic moment. In this study, the effective field of the Heisenberg model is written as:

$$\boldsymbol{H}_{eff}^{i} = \frac{1}{\mu_0 \mu_i} \sum_{j=nn.\ of\ i} J_{ij} \boldsymbol{S}_j + \frac{2D_i(\boldsymbol{S}_i \cdot \boldsymbol{n}_i)\boldsymbol{n}_i}{\mu_0 \mu_i} + \boldsymbol{H}_D^i + \boldsymbol{H} \tag{4.14}$$

Where $\boldsymbol{H}_D^i$ is the demagnetizing field due to the dipolar interaction.

4.3 Monte Carlo Algorithms

4.3.1 Monte Carlo Metropolis Sampling

Based on the Hamiltonian of the Heisenberg model in Equation 4.2, static magnetic properties can be numerically calculated by the Monte Carlo Metropolis sampling method.[81] The Monte Carlo Metropolis sampling algorithm for a classical spin system proceeds as follows:

1. Start with an arbitrary spin configuration $\alpha_k = \{\boldsymbol{S}_1, \boldsymbol{S}_2,\ \ldots,\ \boldsymbol{S}_N\}$.
2. Generate a trial configuration α_{tr}.
3. Calculate the energy $E(\alpha_{tr})$ of the trial configuration.
4. Examine whether $E(\alpha_{tr}) \leq E(\alpha_k)$, accept by setting $\alpha_{k+1} = \alpha_{tr}$.
5. If $E(\alpha_{tr}) > E(\alpha_k)$, accept with relative probability:

$$P = \exp\left(-\frac{\Delta E}{k_B T}\right) \tag{4.15}$$

Practically, choose a uniform random number r_j where $0 \leq r_j \leq 1$

$$\alpha_{k+1} = \begin{cases} \alpha_{tr}, & if\ P \geq r_j\ (accept) \\ \alpha_k, & if\ P < r_j\ (reject) \end{cases} \tag{4.16}$$

For each Monte Carlo sweep (MCSWP), the program goes through from Step 1 to 5 and repeats the process for N times, where N is the total number of spins in the system.

There are two important features of the Metropolis algorithm: ergodicity and reversibility. First, for ergodicity, the algorithm should, in theory, sample all possible configurations to provide unbiased static properties. For the Metropolis algorithm, the trial configuration is created in Step 2. Generally, there are ways to pick up a new orientation for a specific $\boldsymbol{S}_i$: (1) flip-over, (2) Gaussian distribution, and (3) uniform distribution. In this study, the trial spin is generated by a combined manner, determined by:

$$\boldsymbol{S}_{trial} = \frac{\boldsymbol{S} + \sigma\boldsymbol{\Gamma}}{|\boldsymbol{S} + \sigma\boldsymbol{\Gamma}|} \tag{4.17}$$

Where $\boldsymbol{\Gamma}$ is a random unit vector following spherical uniform distribution, and the parameter σ sets the displacement limit of each MC iteration. Obviously, the ergodicity is satisfied by Equation 4.17. Finally, the reversibility can be verified given the probability Equation 4.15 in Step 5, which is discussed in detail in APPENDIX A.

4.3.2 Monte Carlo Parallel Tempering

The Metropolis algorithm is usually quite efficient for modeling static thermodynamic properties. However, running time for reaching equilibrium grows rapidly for a large-scale atomistic simulation. To accelerate the calculation, a parallel tempering scheme can be adopted by using a high performance computing cluster.[82] In the parallel tempering algorithm, a series of copies of the system or “replica” are simulated at different temperatures independently. During the simulation two types of transitions are used: the Metropolis transition, and the replica transition. The Metropolis transition happens within each temperature copy in the same way as the simple Metropolis sampling. Additionally, after each MCSWP, the replica transition is executed by swapping copies between two neighboring temperatures with a certain acceptance probability as shown in Equation 4.18. This probability is selected satisfying a detailed balance requirement. More details can be found in APPENDIX A.

$$P[\,(E_i,T_i)\to(E_{i+1},T_{i+1})\,] = \min\left\{1,\exp\left[\frac{(E_{i+1}-E_i\,)}{k_B}\left(\frac{1}{T_{i+1}}-\frac{1}{T_i}\right)\right]\right\} \tag{4.18}$$

The replica transition effectively generates a random walk in the temperature space and helps the system to overcome energy barriers and escape local energy minima. This enables the parallel tempering algorithm to be able to sample over larger phase space than the simple Metropolis sampling. For optimized efficiency, the replica's temperatures have to be carefully selected. In this study, temperatures were selected by a geometric progression[83], for example:

$$T_i \equiv T_{low}r^i, \quad i = 0, 1, \dots, N_{replica}-1 \tag{4.19}$$

Where r is defined as:

$$r \equiv \left(\frac{T_{high}}{T_{low}}\right)^{\frac{1}{N_{replica}-1}} \tag{4.20}$$

4.4 Atomistic Landau-Lifshitz-Gilbert Algorithm

4.4.1 Atomistic Landau-Lifshitz-Gilbert Equation

The Landau-Lifshitz-Gilbert (LLG) equation is introduced to describe the precession of magnetic magnetization with a phenomenological damping parameter.[84] Generally, the LLG equation is written in the following form:

$$\frac{d\boldsymbol{M}}{dt} = -\frac{\mu_0\gamma}{1+\alpha^2}\boldsymbol{M}\times\boldsymbol{H} - \frac{\alpha\mu_0\gamma}{(1+\alpha^2)M}\boldsymbol{M}\times(\boldsymbol{M}\times\boldsymbol{H}) \tag{4.21}$$

Where $\boldsymbol{M}$ is magnetization, $\boldsymbol{H}$ is magnetic field, μ_0 is vacuum permeability, γ is gyromagnetic ratio, and α is damping parameter. As shown in Equation 4.21, the first term describes an out-of-plane torque that drives $\boldsymbol{M}$ to precess around $\boldsymbol{H}$. The second term provides an in-plane damping torque towards the precession axis. Consequently, this LLG equation implies precessional dynamics of magnetization in an external field. For an atomistic model, $\boldsymbol{M}$ can be substituted by a single spin $\boldsymbol{S}$, thus expressing the dynamic LLG equation for the Heisenberg model as:

$$\frac{d\boldsymbol{S}}{dt} = -\frac{\mu_0\gamma}{1+\alpha^2}\boldsymbol{S} \times \boldsymbol{H}_{eff} - \frac{\alpha\mu_0\gamma}{1+\alpha^2}\boldsymbol{S} \times (\boldsymbol{S} \times \boldsymbol{H}_{eff}) \tag{4.22}$$

Where $\boldsymbol{H}_{eff}$ is the effective field for each spin, defined in Equation 4.14. With Equation 4.22 and 4.14, the dynamics of a spin system can then be examined in a deterministic way, or equivalently at zero temperature.

4.4.2 Stochastic Landau-Lifshitz-Gilbert Equation

In order to capture the physics at a finite temperature, a formal thermal fluctuation term is introduced to the effective field.[85]

$$\boldsymbol{H}_{eff}^{i} = \boldsymbol{H}_{eff0}^{i} + \boldsymbol{\xi}^{i}(t) \tag{4.23}$$

Where $\boldsymbol{\xi}^{i}(t)$ is the thermal fluctuation or white noise term. It should be noted that $\boldsymbol{\xi}$ is not an independent parameter for a specific system. Actually, $\boldsymbol{\xi}$ depends on other parameters such as T, α, γ, μ_i and integration time step Δt. This relationship can be derived by either the fluctuation-dissipation theorem or alternatively by projecting the thermodynamic equilibrium solution into the Fokker-Planck equation (FPE) of the stochastic atomistic LLG equation. Details can be found in APPENDIX B. As a result, $\boldsymbol{\xi}$ satisfies the equations as follows:

$$\langle \xi_\mu^i(t) \rangle = 0 \tag{4.24}$$

$$\langle \xi_\mu^i(t)\xi_\nu^j(t') \rangle = 2\kappa_i \delta_{ij}\delta_{\mu\nu}\delta(t-t') = \frac{2\alpha k_B T}{\mu_0^2 \gamma \mu_i \Delta t}\delta_{ij}\delta_{\mu\nu}\delta(t-t') \tag{4.25}$$

4.5 Micromagnetic Landau-Lifshitz-Bloch Algorithm

Even though the atomistic LLG algorithm considers all of the dynamics of a classical Heisenberg model, the large scale of real problems makes the atomistic approach very slow and usually not applicable. In order to simulate a large system in a reasonable amount of time, a micromagnetic approach based on the dynamics of submicron spin blocks is necessary. As an analogy of atomistic LLG algorithm, micromagnetic dynamics can be described directly using the LLG Equation 4.21, which has been known as the micromagnetic LLG algorithm. However, there is a strong restriction on this micromagnetic LLG approach. Particularly, the fixed saturation magnetization is no longer valid in high temperature regime, especially when approaching the Curie temperature (T_C). This effect results in a seriously overestimated T_C via the micromagnetic LLG algorithm.[86] To correct this error, the saturation magnetization must have the freedom to vary its value, which is the most remarkable feature of the Landau-Lifshitz-Bloch (LLB) algorithm as described below.

4.5.1 Landau-Lifshitz-Bloch Equation

The LLB equation is derived in the current research based on the Fokker-Planck equation (FPE) of stochastic atomistic LLG equation.[87] The FPE can be found in APPENDIX B.

First, for the simplest system of only a single spin, the dynamic equation of the spin polarization, as shown in 4.26, can be derived by integrating both sides of the FPE after multiplied with a spin vector:

$$\frac{\partial \boldsymbol{m}}{\partial t} = -\frac{\gamma\mu_0}{1+\alpha^2}\boldsymbol{m}\times\boldsymbol{H} - \frac{\alpha\gamma\mu_0}{1+\alpha^2}\langle \boldsymbol{S}\times(\boldsymbol{S}\times\boldsymbol{H})\rangle - \frac{2\alpha\gamma k_B T}{(1+\alpha^2)\mu}\boldsymbol{m} \tag{4.26}$$

Equation 4.26 naturally provides a longitudinal relaxation by its last term. In order to obtain a explicit equation that only depends on $\boldsymbol{m}$, the second term has to be evaluated based on a certain spin distribution. One possible distribution has been proposed by Garanin et al.[87]

$$P(\boldsymbol{S},\tau) = \frac{\exp(\boldsymbol{w}\cdot\boldsymbol{S})}{Z(w)}\delta(|\boldsymbol{w}|-1) \tag{4.27}$$

Here $\boldsymbol{w}$ is a distribution parameter and the partition function $Z(w) = 4\pi\sinh w/w$. Note that, the distribution of Equation 4.27 is consistent with the mean field spin distribution of a ferromagnet as shown in Equation 4.7. Based on this distribution, Equation 4.26 can be evaluated to the following form. Detailed derivation is available in APPENDIX C.

$$\begin{aligned}\frac{\partial \boldsymbol{m}}{\partial t} = -\frac{\gamma\mu_0}{1+\alpha^2}\boldsymbol{m}\times\boldsymbol{H} - \frac{\alpha\gamma\mu_0}{1+\alpha^2}\left(1-\frac{m}{w}\right)\frac{\boldsymbol{m}}{m}\times\left(\frac{\boldsymbol{m}}{m}\times\boldsymbol{H}\right)\\ - \Lambda_{\mathrm{N}}\left(1-\frac{\boldsymbol{w}_0\cdot\boldsymbol{m}}{wm}\right)\boldsymbol{m}\end{aligned} \tag{4.28}$$

or equivalently as:

$$\begin{aligned}\frac{\partial \boldsymbol{m}}{\partial t} = -\frac{\gamma\mu_0}{1+\alpha^2}\boldsymbol{m}\times\boldsymbol{H} - \frac{\alpha\gamma\mu_0}{1+\alpha^2}\left(1-\frac{3m}{w}\right)\frac{\boldsymbol{m}}{m}\times\left(\frac{\boldsymbol{m}}{m}\times\boldsymbol{H}\right)\\ - \Lambda_{\mathrm{N}}\left(\boldsymbol{m}-\frac{m}{w}\boldsymbol{w}_0\right)\end{aligned} \tag{4.29}$$

Where w is given by the implicit Langevin equation $B(w) = m$. The Néel attempt frequency Λ_N and the reduced magnetic field $\boldsymbol{w}_0$ are defined in the following equations:

$$\Lambda_N \equiv \frac{2\alpha\gamma k_B T}{(1+\alpha^2)\mu} \tag{4.30}$$

$$\boldsymbol{w}_0 \equiv \frac{\mu_0 \mu \boldsymbol{H}}{k_B T} \tag{4.31}$$

When the temperature is low, $\Lambda_N \to 0$, $m \to 1$, $w \to +\infty$, Equation 4.28 reduces to the same form as the LLG Equation 4.21; whereas the temperature is high, $m \to 0$, $\frac{m}{w} \to \frac{1}{3}$, Equation 4.29 reduces to the Bloch equation as:

$$\frac{\partial \boldsymbol{m}}{\partial t} = -\frac{\gamma \mu_0}{1+\alpha^2} \boldsymbol{m} \times \boldsymbol{H} - \Lambda_{\mathrm{N}} \left(\boldsymbol{m} - \frac{\boldsymbol{w}_0}{3} \right) \tag{4.32}$$

Therefore, Equation 4.28 or 4.29 connects both the LLG equation and Bloch equation, which is known as the LLB equation. Furthermore, the effective field is generally redefined as:

$$\boldsymbol{H}' \equiv \boldsymbol{H} - \frac{k_B T w}{\mu_0 \mu m} \boldsymbol{m} \tag{4.33}$$

The new LLB equation is thus given by:

$$\frac{\partial \boldsymbol{m}}{\partial t} = -\frac{\gamma \mu_0}{1+\alpha^2} \boldsymbol{m} \times \boldsymbol{H}' - \frac{\alpha_\perp \gamma \mu_0}{1+\alpha^2} \frac{\boldsymbol{m}}{m} \times \left(\frac{\boldsymbol{m}}{m} \times \boldsymbol{H}' \right) + \frac{\alpha_\parallel \gamma \mu_0}{1+\alpha^2} \frac{(\boldsymbol{m} \cdot \boldsymbol{H}')\boldsymbol{m}}{m^2} \tag{4.34}$$

Where $\alpha_\perp$ and $\alpha_\parallel$ are defined in the following equations:

$$\alpha_\perp \equiv \alpha \left(1 - \frac{m}{w} \right) \tag{4.35}$$

$$\alpha_\parallel \equiv \frac{2\alpha m}{w} \tag{4.36}$$

Now, the trivial single-spin system will be extended to a complicated multiple-spin system. Unfortunately, since the multi-spin FPE contains contributions from all the spins, a similar integration of both sides of the multi-spin FPE cannot provide any simple formulation. To arrive at a similar form as Equation 4.26, a mean field assumption has to be introduced, which decouples the total probability density into a product of single spin probability densities. Following the derivation in APPENDIX D, a multi-spin FPE finally reduces to the same form as in Equation 4.26, only substituting $\boldsymbol{H}$ to $\boldsymbol{H}_{eff}$. This simplification also implies that the mean field assumption is essentially built-in for the LLB equation of a multi-spin system.

4.5.2 Stochastic Landau-Lifshitz-Bloch Equation

As previously derived, the LLB equation provides a deterministic solution of the spin polarization at a finite temperature. Note that, it generates an averaged path of the system because it originates from the FPE. To simulate a particular path, similar stochastic terms should be added to the deterministic LLB equation. As suggested by Evans et al[88], the stochastic LLB equation can be formulated by introducing Gaussian random field and Gaussian random torque:

$$\begin{aligned}\frac{\partial \boldsymbol{m}}{\partial t} = -\frac{\gamma\mu_0}{1+\alpha^2}\boldsymbol{m}\times\boldsymbol{H}'_{eff} - \frac{\alpha_\perp\gamma\mu_0}{1+\alpha^2}\frac{\boldsymbol{m}\times\left(\boldsymbol{m}\times\left(\boldsymbol{H}'_{eff}+\boldsymbol{\xi}_\perp(\tau)\right)\right)}{m^2} \\ + \frac{\alpha_\parallel\gamma\mu_0}{1+\alpha^2}\frac{\left(\boldsymbol{m}\cdot\boldsymbol{H}'_{eff}\right)\cdot\boldsymbol{m}}{m^2} + \boldsymbol{\xi}_\parallel(\tau)\end{aligned} \tag{4.37}$$

Where the white noise terms satisfy:

$$\langle\xi^i_\alpha(t)\rangle \equiv 0 \tag{4.38}$$

$$\langle\xi^i_\alpha(t)\xi^j_\beta(t')\rangle \equiv 2\kappa_\alpha\delta_{\alpha\beta}\delta_{ij}\delta(t-t') \tag{4.39}$$

Where $\alpha,\beta=\perp,\parallel$, and $i,j=x,y,z$, and κ_α are constants determined by multiple parameters. A detailed derivation in APPENDIX E leads to the equations as follows:

$$\kappa_\parallel = \frac{\gamma\mu_0}{1+\alpha^2}\frac{\alpha_\parallel k_B T}{\mu N} \tag{4.40}$$

$$\kappa_\perp = \frac{1+\alpha^2}{\gamma\mu_0}\frac{(\alpha_\perp-\alpha_\parallel)k_B T}{\mu N} \tag{4.41}$$

Where N is the number of spins in each micro-cell.

4.6 Magnetic Modeling Package

4.6.1 Modeling Package Design

Several magnetic modeling packages exist, for example the atomistic magnetic simulation package VAMPIRE of University of York and the micromagnetic modeling package OOMMF of NIST. However, a new program package is still imperative in order to have a thorough understanding of algorithms, and more importantly, enough freedom to integrate both static and dynamic simulations with all possible methods ranging from Monte Carlo to stochastic LLG/LLB as introduced in previous sections. For this study, a numerical magnetic modeling package (MMP) was designed from ground up. C++ was chosen as the programming language in order to make MMP more efficient, readable, extendable and portable. The code was initially written on an Ubuntu 16.04 Linux system, and successfully runs on both Linux/Unix and Windows 7 platforms.

The whole program consists of different functionalities such as amorphous structure generation, simulation condition setup, atomistic calculation, micromagnetic calculation, and result analysis. At the cores of the MMP, the atomistic and micromagnetic calculation functionalities were object-oriented programmed (OOP), similar to the well-known package OOMMF. For example, as building blocks, atoms in atomistic modeling were defined in a class named “Atom”. Higher than the level of atoms, parameters and operations of the whole simulation space were incorporated in a class named “Lattice.” This simplifies the process of adding new operations and thus makes the whole program less prone to bugs.

Another designing feature that is worth mentioning is the library of useful functions such as a random number generator, 3D vector, spherical histogram, and special mathematical functions, e.g. the Langevin function. The library is separately located in the root folder of the MMP. These elements were designed to assist all other functionalities and creating a concise code.

4.6.2 Scientific Constants and Unit System

This study deals with a list of scientific constants, which are summarized in Table 4.1. Moreover, to simulate properties of nanoscale structures, tedious units are omitted and the system dimensions are simplified. The unit values of different physical quantities for this study are listed in Table 4.1.

Table 4.1. Scientific constants and unit system used in the MMP.

Name	**Value**	**Name**	**Value**
μ_B	9.2740×10^{-24} J T^{-1}	Unit energy E_0	8.601×10^{-24} J
N_A	$6.022140857 \times 10^{23}$ mol^{-1}	Unit length δ_0	10^{-10} m = 1 Å
k_B	$1.38064852 \times 10^{-23}$ J K^{-1}	Unit field B_0	0.92740 T
γ_e	$1.760859644 \times 10^{11}$ rad T^{-1} s^{-1}	Unit time τ_0	1.226×10^{-11} s
$\hbar$	$1.054571800 \times 10^{-34}$ J s	Unit temperature θ_0	0.623 K

4.6.3 Random Number Generator

A random number generator is an integral numerical tool, especially for a large-scale simulation using Monte Carlo methods or stochastic algorithms. As is well-known, computers can only generate pseudo random numbers, which means that the random number sequence is not perfect and its period is a finite number. In this study, the period length should be long enough to cover all possible calculations during the whole simulation time. The pseudorandom number generator from *Numerical Recipe*[89] is employed in the MMP due to its elegant language, long period and high efficiency. Additionally, a standard normal distribution generator is built on the pseudorandom number generator. The program follows a Ziggurat algorithm suggested by Marsaglia G and Tsang W-W.[90] The code of the random number generator can be found in APPENDIX F.

4.6.4 Dipolar Interaction and Demagnetizing Field

Even though the dipolar interaction is weak, it is included in the MMP as the third term of the Heisenberg Hamiltonian in Equation 4.2. Based on the unit system in this study, the dimensionless dipolar interaction can be simplified as:

$$E_{dip} = -\frac{1}{2}\sum_{i\neq j}\frac{\mu_i\mu_j}{r_{ij}^3}\left(3(\boldsymbol{S}_i\cdot\hat{\boldsymbol{r}}_{ij})(\boldsymbol{S}_j\cdot\hat{\boldsymbol{r}}_{ij})-\boldsymbol{S}_i\cdot\boldsymbol{S}_j\right) \tag{4.42}$$

Where μ_i is the dimensionless atomic moment, and the dimensionless displacement is defined as $\boldsymbol{r}_{ij}\equiv\boldsymbol{R}_{ij}/\delta$. $\hat{\boldsymbol{r}}_{ij}$, a unit vector, is defined as $\boldsymbol{r}_{ij}/r_{ij}$. A demagnetizing tensor is defined as:

$$K^{\alpha\beta}(\boldsymbol{r})\equiv-\frac{\partial}{\partial r_\alpha}\left(\frac{r_\beta}{r^3}\right)=\frac{3\hat{r}_\alpha\hat{r}_\beta-\delta_{\alpha\beta}}{r^3}=\frac{1}{r^3}\begin{bmatrix}3\hat{r}_x^2-1 & 3\hat{r}_x\hat{r}_y & 3\hat{r}_x\hat{r}_z\\ 3\hat{r}_x\hat{r}_y & 3\hat{r}_y^2-1 & 3\hat{r}_y\hat{r}_z\\ 3\hat{r}_x\hat{r}_z & 3\hat{r}_y\hat{r}_z & 3\hat{r}_z^2-1\end{bmatrix} \tag{4.43}$$

Where $\alpha,\beta=x,y,z$. It is easy to verify that $K^{\alpha\beta}=K^{\beta\alpha}$ and $K(\boldsymbol{r})=K(-\boldsymbol{r})$. Equation 4.42 is thus rearranged into the following form:

$$\begin{aligned}E_{dip} &= -\frac{1}{2}\sum_{i\neq j}\frac{\mu_i\mu_j}{r_{ij}^3}\left(3S_i^\alpha\hat{r}_{ij}^\alpha S_j^\beta\hat{r}_{ij}^\beta-S_i^\alpha\delta_{\alpha\beta}S_j^\beta\right)\\ &= -\frac{1}{2}\sum_{i\neq j}\mu_i\mu_j S_i^\alpha K^{\alpha\beta}(\boldsymbol{r}_{ij})S_j^\beta\\ &= -\frac{1}{2}\sum_i\mu_i S_i^\alpha\left(\sum_{j,j\neq i}\mu_j\,K^{\alpha\beta}(\boldsymbol{r}_{ij})S_j^\beta\right)\end{aligned} \tag{4.44}$$

Now, the dimensionless demagnetizing field can be expressed as:

$$h_D^\alpha(\boldsymbol{x})=\sum_i\mu_i K^{\alpha\beta}\left(\frac{\boldsymbol{x}-\boldsymbol{x}_i}{\delta}\right)S_i^\beta \tag{4.45}$$

The definition is also confirmed by:

$$h^{\alpha}_{D,i} = -\frac{1}{\mu_i}\frac{\partial E_{dip}}{\partial S^{\alpha}_i} = \sum_{j \neq i} \mu_j K^{\alpha\beta}\left(\frac{\boldsymbol{x}_i - \boldsymbol{x}_j}{\delta}\right) S^{\beta}_j \tag{4.46}$$

As Equation 4.46 shows, the calculation of demagnetizing field requires a convolution of the demagnetizing tensor and atom spins. Numerically, this convolution is implemented through the Fast Fourier Transform (FFT) algorithm to gain highest efficiency. For example, in 3D crystal lattice, defined by $\boldsymbol{h}_D\left(\boldsymbol{x}_{i,j,k}\right) \equiv \boldsymbol{h}_{D,i,j,k}$ and $K\left(\frac{\boldsymbol{x}_{l,m,n} - \boldsymbol{x}_{i,j,k}}{\delta}\right) \equiv K_{l-i,m-j,n-k}$, the discretized demagnetizing field is written as:

$$h^{\alpha}_{D,l,m,n} = \sum_{i=-\infty}^{+\infty} \sum_{j=-\infty}^{+\infty} \sum_{k=-\infty}^{+\infty} \mu_{i,j,k} K^{\alpha\beta}_{l-i,m-j,n-k} S^{\beta}_{i,j,k} \tag{4.47}$$

For periodic boundary conditions, atom moment is periodic:

$$\boldsymbol{\mathcal{M}}_{i,j,k} \equiv \mu_{i,j,k}\boldsymbol{S}_{i,j,k} = \boldsymbol{\mathcal{M}}_{i+n_x,j+n_y,k+n_z} \tag{4.48}$$

And the demagnetizing tensor can be redefined as periodic function as well:

$$\widetilde{K}_{i,j,k} \equiv \sum_{\lambda_x=-\infty}^{+\infty} \sum_{\lambda_y=-\infty}^{+\infty} \sum_{\lambda_z=-\infty}^{+\infty} K_{i+\lambda_x n_x, j+\lambda_y n_y, k+\lambda_z n_z} \tag{4.49}$$

Where $i = 0, 1, 2, \cdots, n_x - 1$, $j = 0, 1, 2, \cdots, n_y - 1$, $k = 0, 1, 2, \cdots, n_z - 1$. Using the periodic tensor and moment, the demagnetizing field satisfies the convolution requirement of the discrete Fourier transform (DFT):

$$h^{\alpha}_{D,l,m,n} = \sum_{i=0}^{n_x-1} \sum_{j=0}^{n_y-1} \sum_{k=0}^{n_z-1} \widetilde{K}^{\alpha\beta}_{l-i,m-j,n-k} \mathcal{M}^{\beta}_{i,j,k} \tag{4.50}$$

The convolution can then be calculated through DFT as:

$$h^{*,\alpha}_{D,r,s,t} = \widetilde{K}^{*,\alpha\beta}_{r,s,t} \mathcal{M}^{*,\beta}_{r,s,t} \tag{4.51}$$

Where $\boldsymbol{h}^*_D \equiv DFT\{\boldsymbol{h}_D\}$, $\widetilde{K}^* \equiv DFT\{\widetilde{K}\}$, and $\boldsymbol{\mathcal{M}}^* \equiv DFT\{\mu\boldsymbol{S}\}$. This procedure is accelerated by the famous FFT algorithm.[91]

It should be noted that in a system with free boundary conditions, a padding technique[92] is needed to satisfy Equation 4.50. Details can be found in APPENDIX G. Finally, the FFT calculation is handled by the free FFTW library in the MMP.

4.6.5 Heun Integration Scheme for Stochastic LLG Algorithm

Finalizing the introduction of the MMP, the Heun integration scheme is shown to be a critical component for the stochastic LLG algorithms. As previously discussed, the dimensionless stochastic LLG equation can be rearranged into the form as:

$$\frac{dS_i^{\mu}(\tau)}{d\tau} = a_i^{\mu}\big(\boldsymbol{S}(\tau)\big) + \sqrt{2\kappa_i}\, b_i^{\mu\lambda}\big(\boldsymbol{S}(\tau)\big)\zeta_i^{\lambda}(\tau) \tag{4.52}$$

Where $\mu, \lambda = x, y, z$, a_i^{μ} is the drift parameter, and $b_i^{\mu\lambda}$ is the volatility tensor. In order to be consistent with Equation 4.52, the integration scheme has to be carefully designed. More importantly, integration has to be considered as a Stratonovich type:

$$\begin{aligned} S_i^{\mu}(\tau + \Delta\tau) = S_i^{\mu}(\tau) + a_i^{\mu}\big(\boldsymbol{S}(\tau)\big)\Delta\tau \\ + \sqrt{2\kappa_i}\left(\frac{b_i^{\mu\lambda}\big(\boldsymbol{S}(\tau + \Delta\tau)\big) + b_i^{\mu\lambda}\big(\boldsymbol{S}(\tau)\big)}{2}\right)\Big(W_i^{\lambda}(\tau + \Delta\tau) \\ - W_i^{\lambda}(\tau)\Big) \end{aligned} \tag{4.53}$$

Where W_i^{λ} is a standard Wiener process. The Heun integration scheme can thus be defined as:

$$S_i^{\mu}(\tau + \Delta\tau) \approx S_i^{\mu}(\tau) + \tilde{a}_i^{\mu}\Delta\tau + \sqrt{2\kappa_i}\tilde{b}_i^{\mu\lambda}\left(W_i^{\lambda}(\tau + \Delta\tau) - W_i^{\lambda}(\tau)\right) \tag{4.54}$$

Where:

$$\tilde{a}_i^{\mu} \equiv \frac{1}{2}\Big(a_i^{\mu}\big(\boldsymbol{S}(\tau)\big) + a_i^{\mu}\left(\tilde{\boldsymbol{S}}(\tau + \Delta\tau)\right)\Big) \tag{4.55}$$

$$\tilde{b}_i^{\mu\lambda} \equiv \frac{1}{2}\left(b_i^{\mu\lambda}\big(\boldsymbol{S}(\tau)\big) + b_i^{\mu\lambda}\left(\tilde{\boldsymbol{S}}(\tau+\Delta\tau)\right)\right) \tag{4.56}$$

$$\begin{aligned}\tilde{S}_i^{\mu}(\tau+\Delta\tau) \equiv S_i^{\mu}(\tau) + a_i^{\mu}\big(\boldsymbol{S}(\tau)\big)\Delta\tau \\ + \sqrt{2\kappa_i}\, b_i^{\mu\lambda}\big(\boldsymbol{S}(\tau)\big)\left(W_i^{\lambda}(\tau+\Delta\tau) - W_i^{\lambda}(\tau)\right)\end{aligned} \tag{4.57}$$

Equivalently, the Heun integration can be expressed in two steps of predictor and corrector:

(1) Predictor:

$$\tilde{\boldsymbol{S}}_i \equiv \boldsymbol{S}_i(\tau) + \Delta\boldsymbol{S}_i\Delta\tau \tag{4.58}$$

Where:

$$\begin{aligned}\Delta\boldsymbol{S}_i = -g_{L,i}\boldsymbol{S}_i \times \left(\boldsymbol{h}_{eff}^{i} + \sqrt{2\kappa_i}\dot{\boldsymbol{W}}_i(\tau;\Delta\tau)\right) - \alpha_i g_{L,i}\boldsymbol{S}_i \\ \times \left(\boldsymbol{S}_i \times \left(\boldsymbol{h}_{eff}^{i} + \sqrt{2\kappa_i}\dot{\boldsymbol{W}}_i(\tau;\Delta\tau)\right)\right)\end{aligned} \tag{4.59}$$

(2) Corrector:

$$\boldsymbol{S}_i(\tau+\Delta\tau) = \boldsymbol{S}_i(\tau) + \frac{1}{2}\big(\Delta\boldsymbol{S}_i + \Delta\tilde{\boldsymbol{S}}_i\big)\Delta\tau \tag{4.60}$$

Where:

$$\begin{aligned}\Delta\tilde{\boldsymbol{S}}_i = -g_{L,i}\tilde{\boldsymbol{S}}_i \times \left(\tilde{\boldsymbol{h}}_{eff}^{i} + \sqrt{2\kappa_i}\dot{\boldsymbol{W}}_i(\tau;\Delta\tau)\right) - \alpha_i g_{L,i}\tilde{\boldsymbol{S}}_i \\ \times \left(\tilde{\boldsymbol{S}}_i \times \left(\tilde{\boldsymbol{h}}_{eff}^{i} + \sqrt{2\kappa_i}\dot{\boldsymbol{W}}_i(\tau;\Delta\tau)\right)\right)\end{aligned} \tag{4.61}$$

Note again that $\sqrt{2\kappa_i}\dot{\boldsymbol{W}}_i(\tau;\Delta\tau) \sim N\left(0, \frac{2\alpha_i}{\beta g_i \mu_i \Delta\tau}\right)$ and bears the same value for both Equation 4.59 and Equation 4.61.

4.7 Modeling Tests on Amorphous RE-TM Alloys

In order to test the new MMP, a series of numerical modeling were finished on the amorphous RE-TM alloys. This testing system has been well studied by Ostler et al.[80,93–95] from the University of

York with their atomistic modeling package VAMPIRE. This section compares the results of the MMP to that of the VAMPIRE. As will be presented, the MMP is capable of reproducing the published results and applying new algorithms to obtain better performance.

4.7.1 Atomistic Model of Amorphous RE-TM Alloy

As important ferrimagnetic materials, amorphous RE-TM alloys have been extensively studied, both experimentally and numerically. Theoretically, this two-sublattice ferrimagnetic system can be modeled by an atomistic approach based on a classical Heisenberg Model. GdFeCo was selected as a representative of RE-TM alloys to effectively complete this process. The atomic moment for RE is 7.63 μ_B and 2.217 μ_B for TM. The exchange constants of RE and TM were selected as 1.26×10^{-21} J/link and 4.5×10^{-21} J/link respectively. The antiferromagnetic (AFM) exchange constant between RE and TM sublattice was -1.09×10^{-21} J/link. A uniaxial perpendicular magnetic anisotropy was assumed as 8.07×10^{-24} J/atom in this RE-TM system. Dipolar interaction was dropped due to its insignificant value compared to other interactions. The damping parameter for both RE and TM was set to 0.1, and gyromagnetic ratios were treated the same as the electron gyromagnetic ratio $\gamma_e = 1.76 \times 10^{11}$ rad T^{-1} s^{-1}.

In the following studies, a pseudo amorphous structure was adopted, which populates RE and TM atoms randomly in a face-centered cubic (FCC) crystal lattice according to a designed atomic concentration, as shown in Figure 4.1. This study applied the same lattice dimension (50 × 50 × 50) as that of Ostler et al.[93] A simple periodic boundary condition was used to eliminate the finite size effect for the large size alloy sample. All the related parameters are summarized in Table 4.2.

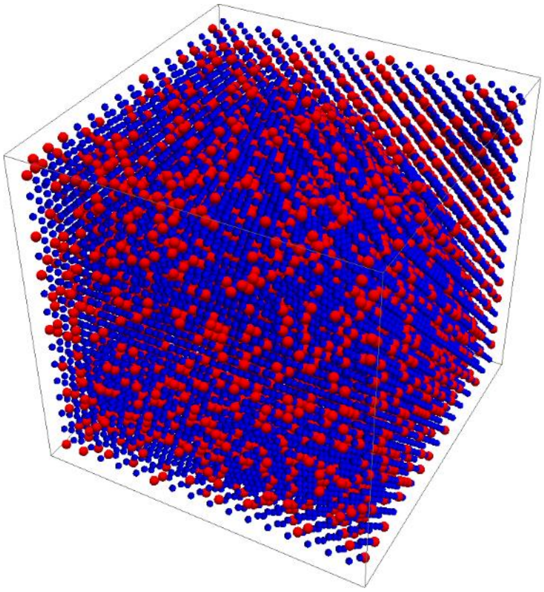

Figure 4.1. Pseudo amorphous atomistic structure of $RE_{26}TM_{74}$ on a 50 × 50 × 50 FCC lattice. RE is represented by red sphere, and TM is represented by blue sphere.

Table 4.2. Atomistic modeling parameters for RE-TM tests.

Parameter	**Value**	**Parameter**	**Value**
μ_{RE}	7.63 μ_B	λ_{RE}	0.1
μ_{TM}	2.217 μ_B	λ_{TM}	0.1
J_{RE-RE}	1.26×10^{-21} J/link	γ_{RE}	1.76×10^{11} radT^{-1}s^{-1}
J_{TM-TM}	4.5×10^{-21} J/link	γ_{TM}	1.76×10^{11} radT^{-1}s^{-1}
J_{RE-TM}	-1.09×10^{-21} J/link	Lattice	50 × 50 × 50
D	8.07×10^{-24} J/atom	Boundary Condition	Periodic

4.7.2 Temperature Dependence of Magnetization

The temperature dependence of magnetization was simulated for different RE concentration. The stochastic LLG algorithm was employed for calculations for the first trial. As shown in Figure 4.2, the Curie temperature of the system increased as the TM concentration ramped up. In addition, the compensation temperature only existed for a certain RE concentration, e.g. from 24 at. % to 40 at. %. Figure 4.2 (a) and (b), and (c) and (d) compare the results of the MMP to that of Ostler et al.[93] These results verify that the MMP can generate almost identical results to the VAMPIRE.

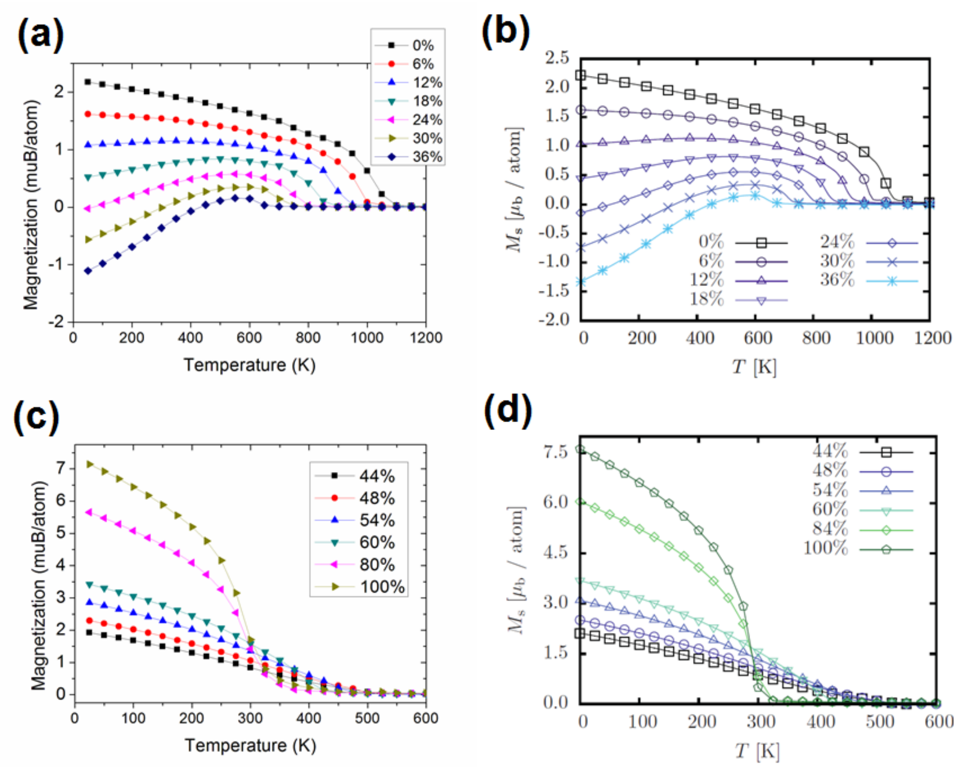

Figure 4.2. Magnetization vs. temperature curves of amorphous RE-TM alloys were simulated by the LLG functionality of the MMP, as shown in (a) and (c), compared to the published results from Ostler et al.[93] in (b) and (d).

Moreover, the temperature dependence can be properly simulated not only by the stochastic LLG algorithm, but also by a straight forward Monte Carlo Metropolis sampling. Figure 4.3 demonstrate the results of the MMP, which are highly consistent with Ostler's data in Figure 4.2 (b) and (d).

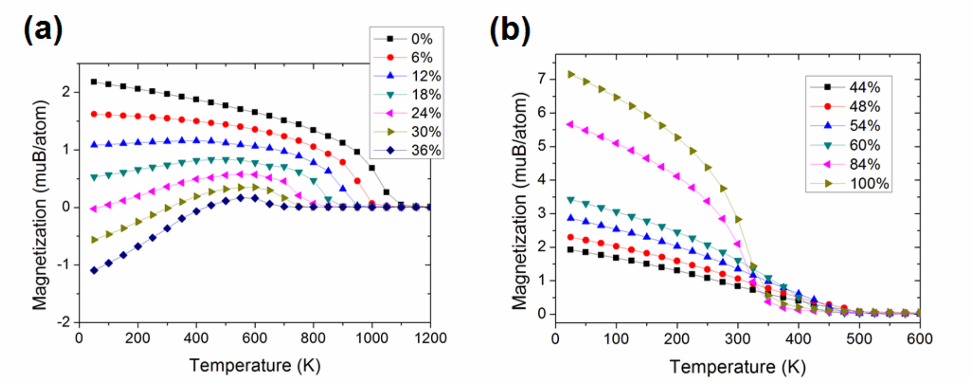

Figure 4.3. Magnetization vs. temperature curves of amorphous RE-TM alloys were calculated by the Monte Carlo Metropolis functionality of the MMP.

This demonstrated success with Metropolis sampling implies a parallel computing scheme based on parallel tempering, which is more efficient for larger-scale problems. Figure 4.4 provides the magnetization vs. temperature curves powered by the parallel tempering functionality of the MMP. Obviously, a larger number of data points smooth out the curve. In addition, at the University of Virginia, those curves were finished in five minutes on the high-performance cluster Rivanna. This demonstrates the excellent efficiency of parallel tempering in simulating static properties such as magnetization.

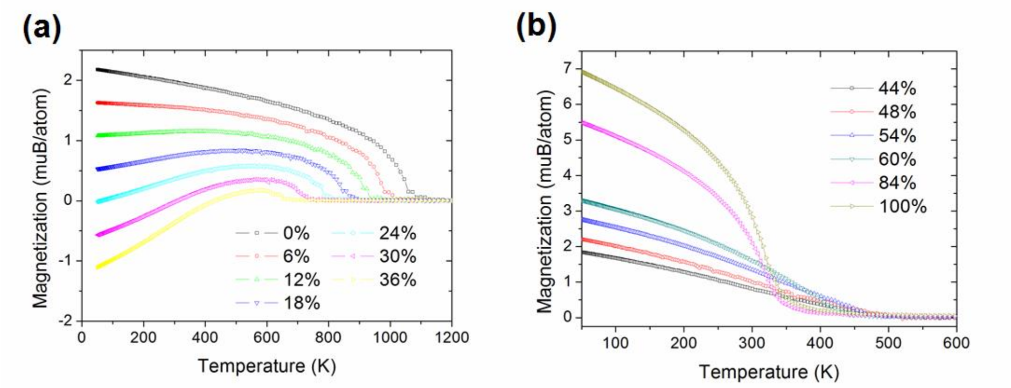

Figure 4.4. Magnetization vs. temperature curves of amorphous RE-TM alloys were simulated by the parallel tempering functionality of the MMP.

4.7.3 Magnetic Hysteresis Loops and Coercivity

Magnetic hysteresis loops are another integral property of the RE-TM system. Figure 4.5 shows 10 independent simulation runs of magnetic hysteresis loops of $RE_{26}TM_{74}$ at 300 K by the stochastic LLG algorithm. Due to the stochastic feature, each of the curves is slightly different from the others.

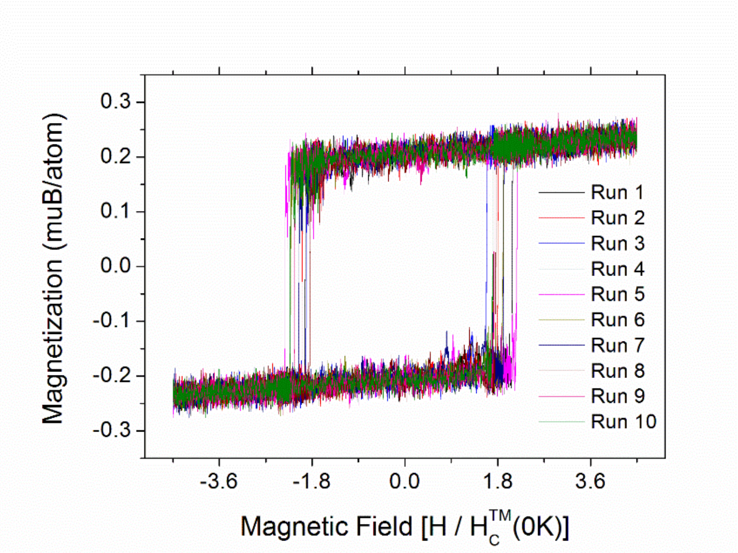

Figure 4.5. Hysteresis loops of amorphous $RE_{26}TM_{74}$ were simulated at 300 K. Ten independent simulation runs are plotted.

An average of the magnetic hysteresis loops offers insight into the average magnetization and coercivity. Figure 4.6 presents a temperature dependence on the coercivity of $RE_{26}TM_{74}$. As demonstrated in Figure 4.6 (a), the coercivity diverged at temperatures around 200 K, which corresponds to its compensation temperature. This trend supports the results from Ostler et al.[93] as expressed in Figure 4.6 (b).

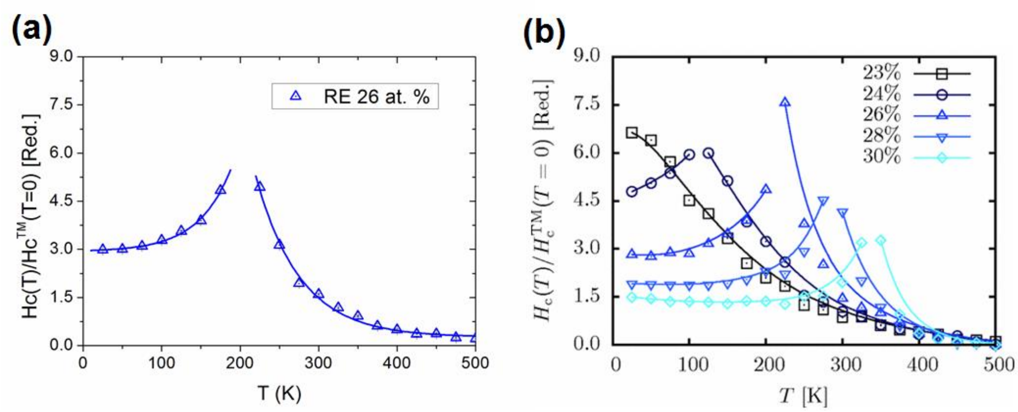

Figure 4.6. Coercivity vs. temperature curve of amorphous $RE_{26}TM_{74}$ was calculated by the MMP, as shown in (a), compared to the published results of Ostler et al.[93] in (b).

4.7.4 Tuning Exchange Constants

In the RE-TM system, the Hamiltonian is dominated by the exchange interaction term between nearest neighboring sites. As shown by Ostler et al.[93], the influence of tuning the antiferromagnetic exchange constant J_{RE-TM} can also be verified by the MMP. In this section, the present study used the efficient parallel tempering technique. Results are provided in Figure 4.7.

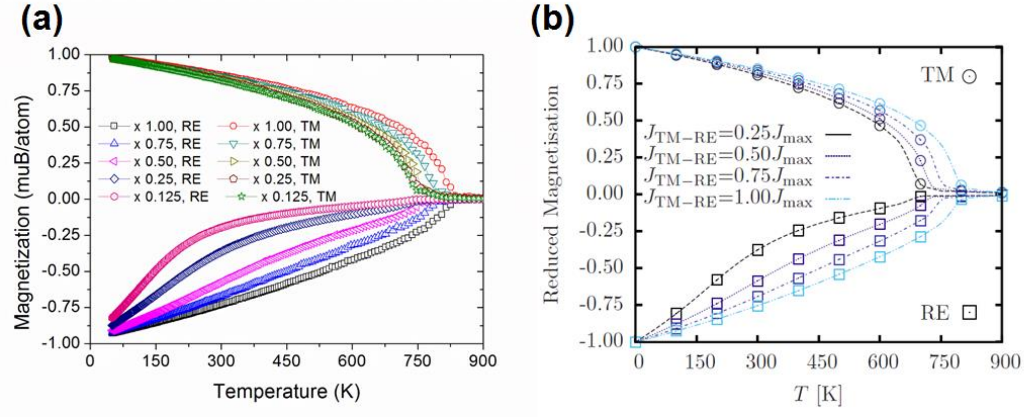

Figure 4.7. Temperature dependence of magnetization was simulated for RE and TM sublattices with different J_{RE-TM}. (a) shows the results using the parallel tempering functionality of the MMP. (b) provides published results from Ostler et al.[93]

In Figure 4.8, a step-like temperature pulse of 300 K was exerted at exactly zero time on a spin system in its ground state. Here, the effective temperature of the spin system quickly ramped up to 300 K within several picoseconds. Moreover, the relaxation time was shorter for the system with higher value of $|J_{RE-TM}|$. The findings from the MMP offered the same results as Ostler et al.'s VAMPIRE.[93]

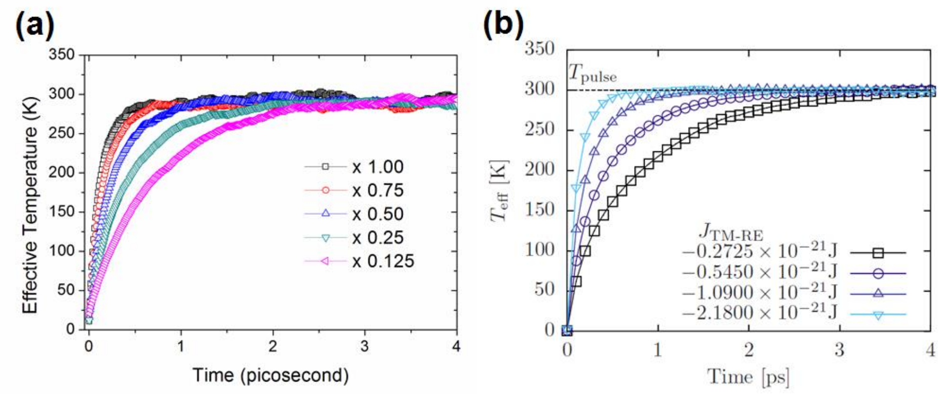

Figure 4.8. Effective temperature vs. time curves of amorphous $RE_{26}TM_{74}$ were simulated by the MMP in (a), compared to the results from Ostler et al.[93] as shown in (b).

4.7.5 Ferromagnetic Resonance

The ferromagnetic resonance of RE-TM alloy can also be simulated using the atomistic model of the MMP. The absorbed power during the ferromagnetic resonance is given using the following equation:

$$P_{FMR}(\omega) = -\frac{\omega}{2\pi}\int_0^{\frac{2\pi}{\omega}} \boldsymbol{M}(t) \cdot \frac{\partial \boldsymbol{B}(t)}{\partial t} dt \tag{4.62}$$

This integral was calculated using a simple first-order trapezium integration scheme. Figure 4.9 provides the results of the frequency dependence of FMR absorbed power at zero temperature. For each concentration, the power absorption has a maximum that corresponds to the FMR resonance. Empirical findings show that both the peak position and the maximum absorbed power strongly depended on the RE concentration. More interestingly, when $x = 0.2$, the curve is significantly depressed to zero, which corresponds to a full compensation at zero Kelvin. These findings confirm, yet again, that the results of the MMP are identical to the VAMPIRE (Ostler et al.[96]) in Figure 4.9.

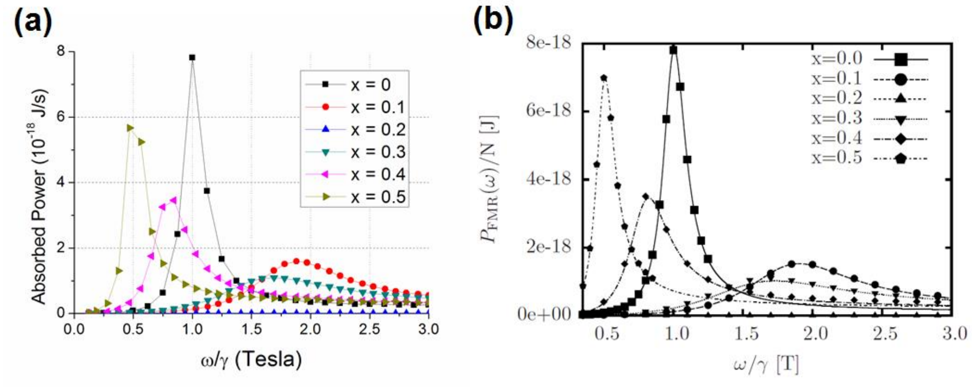

Figure 4.9. FMR absorbed power vs. field frequency curves were simulated for amorphous RE-TM alloys at 0 K. (a) shows the results generated by the MMP. (b) is from Ostler et al.[96]

4.7.6 Transverse and Longitudinal Susceptibility

Finally, the transverse ($\chi_{\perp}$) and longitudinal ($\chi_{\parallel}$) susceptibility can be derived by statistical physics:

$$\chi_{\alpha} = \beta(\langle M_{\alpha}^{2}\rangle - \langle M_{\alpha}\rangle^{2}) \tag{4.63}$$

Where $\alpha = x, y, z$. When the external field is along z axis:

$$\chi_{\parallel} = \chi_{z} \tag{4.64}$$

$$\chi_{\perp} = \chi_{x\,(y)} \tag{4.65}$$

For the RE-TM system, both susceptibilities could be extracted by parallel tempering as demonstrated in Figure 4.10. The peak of the longitudinal susceptibility, due to a divergent behavior at its Curie temperature, could then be identified. On the other hand, the transverse susceptibility showed an obvious minimum near the compensation temperature.

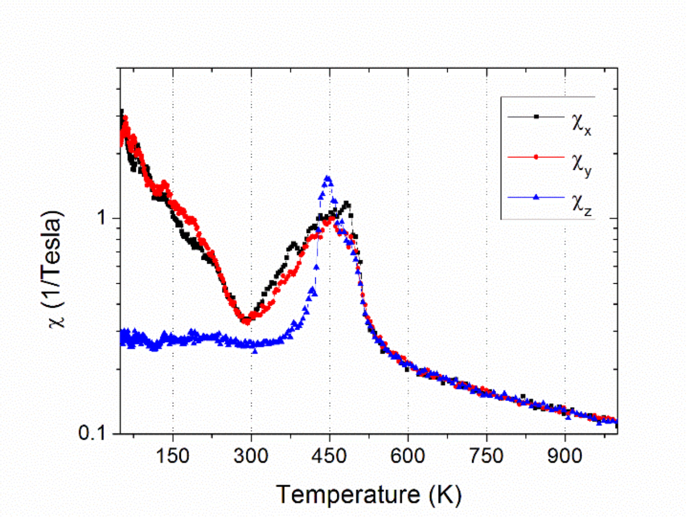

Figure 4.10. Temperature dependence of transverse and longitudinal susceptibility of amorphous $RE_{30}TM_{70}$.

4.8 Concluding Remarks

In this chapter, the fundamentals of the magnetic numerical modeling were introduced, including the atomistic Heisenberg model, the Monte Carlo Metropolis/parallel tempering algorithms, the atomistic LLG method, and the micromagnetic LLB method. These basic methods were programmed from ground up in C++ and combined into a magnetic modeling package (MMP). Employing the MMP, results that were reproduced for the pseudo amorphous GdFe alloys, were consistent with past research, especially that of Ostler et al.[93,96] Therefore, this program package provides powerful tools in which to study the static properties of the RE-TM system, which will be presented in Chapter 5 and Chapter 6. Chapter 7 will focus on numerical research concerning the ultrafast magnetization dynamics of the RE-TM system using the MMP together with a phenomenological two-temperature model.

CHAPTER 5 THICKNESS DEPENDENCE OF MAGNETIZATION IN AMORPHOUS RE-TM THIN FILMS

5.1 Introduction

This chapter will first present empirical experimental results of sputtered amorphous TbFeCo thin films. As previously discussed in Chapter 2, amorphous RE-TM thin films with perpendicular magnetic anisotropy (PMA) have been investigated for their applications in magneto-optical recording[28,97] and high-areal-density low-current spintronic devices, e.g. perpendicular magnetic tunnel junction (p-MTJ) for perpendicular MRAM.[30] In recent years RE-TM alloys have been attracting greater interests due to their potentials in ultrafast magnetic all-optical switching.[12,14,98,99]

Within the family of RE-TM alloys, amorphous TbFeCo, similar to the GdFeCo mentioned in Chapter 4, is ferrimagnetic (FI) and contains antiferromagnetically coupled Tb and FeCo sublattices. These compounds display a compensation temperature (T_{comp}) for a range of Tb concentrations. This phenomenon can be explained by the conventional FI model, where antiparallel sublattice moments compensate each other to produce a zero net magnetic moment. Unlike Gd, that has a zero $4f$ orbital moment at its ground state, Tb has a strong single ion anisotropy due to its $4f$ spin-orbit coupling. Therefore, amorphous TbFeCo possesses strong PMA with K_u about 5×10^6 erg/cm^3 and high coercive fields, which leads to a desirable high thermal stability for spintronic devices. Moreover, a strain-induced enhancement of coercivity has also been reported in the amorphous TbFeCo thin films.[100] This implies a significant magnetostriction effect in the films.

Considering the examined sputtered amorphous TbFeCo thin films, a strong PMA is confirmed by VSM measurements. This chapter will explore the thickness-dependent magnetization phenomenon as it implies a non-uniform depth profile of the amorphous thin film. To further examine the physics, atomistic magnetic modeling was performed based on a depth profile of the short-range order, specifically, the Tb-Fe pair ratio. This model can effectively predict consistent results for both single-sputtered and co-sputtered thin films. The present study yields a deeper understanding of RE-TM amorphous thin films, and provides a new angle for tuning ferrimagnetic magnetization and compensation temperature.

5.2 Experimental Results of Amorphous TbFeCo Thin Films

5.2.1 Sample Preparation and Characterization

For this study amophrous TbFeCo thin films were prepared by the radio frequency (RF) magnetron sputtering system. The depositions were carried out in a high vacuum chamber with a base pressure below 5×10^{-7} Torr. A single-side thermal oxidized Si wafer was used as substrate. During the sputtering, the substrate was cooled to an ambient temperature with chilled water, and kept rotating for a laterally homogeneous deposition. Finally, a 5 nm thick Ta layer was capped on top of the film to protect it from oxidation.

For this study, two sets of samples were prepared at two distinct conditions. The first set of samples were sputtered from a single alloy TbFeCo target under a constant Ar pressure of 1 mTorr; the other set of samples were co-sputtered from a Tb single elementary target and the TbFeCo alloy target under an Ar pressure of 7 mTorr. Both sets consisted of samples of different thicknesses. The thickness of each sample was characterized by XRR on the Rigaku SmartLab®. The composition of the sputtered samples was then tuned by the RF power of each sputtering target. An energy-dispersive X-ray spectroscopy (EDS) was used to analyze the composition of each sample.

The surface profile of the thin film was visualized by an Asylum Cypher scanning probe microscope. A typical profile is shown in Figure 5.1. The root mean squared roughness of the film was about 0.4 nm, which is comparable to most sputtered amorphous films.

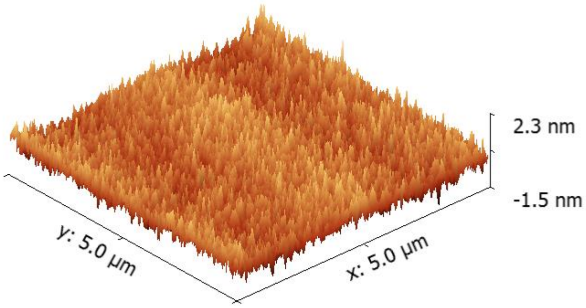

Figure 5.1. Surface profile of a 102 nm co-sputtered TbFeCo film by atom force microscopy.

High-resolution transmission electron microscopy (HRTEM) images were taken on the cross-sectional specimens for both single-sputtered and co-sputtered TbFeCo thin films by FEI Titan® at 300 keV. As shown in Figure 5.2, no obvious nano-crystallinity existed, which was supported by the corresponding diffusive rings of fast Fourier transform (FFT).

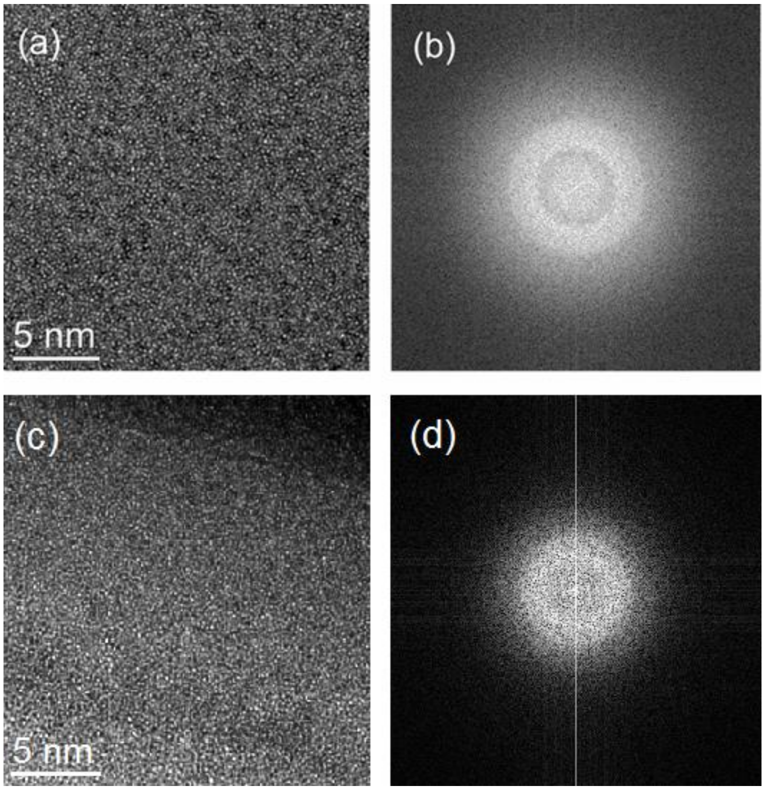

Figure 5.2. HRTEM images of co-sputtered (a) and single-sputtered (c) TbFeCo thin films. The corresponding FFT images are plotted in (b) and (d) for co-sputtered and single-sputtered films respectively.

Additionally, the amorphous TbFeCo was found to be sensitive to a high energy electron beam, e.g. 300 keV. As shown in Figure 5.3, the amorphous structure started to form nano-crystals after irradiated by a 300 keV electron beam for about 5 minutes. The FFT of the irradiated portion gives a spotted pattern, and corresponds to different orientations of nano-crystals within this region.

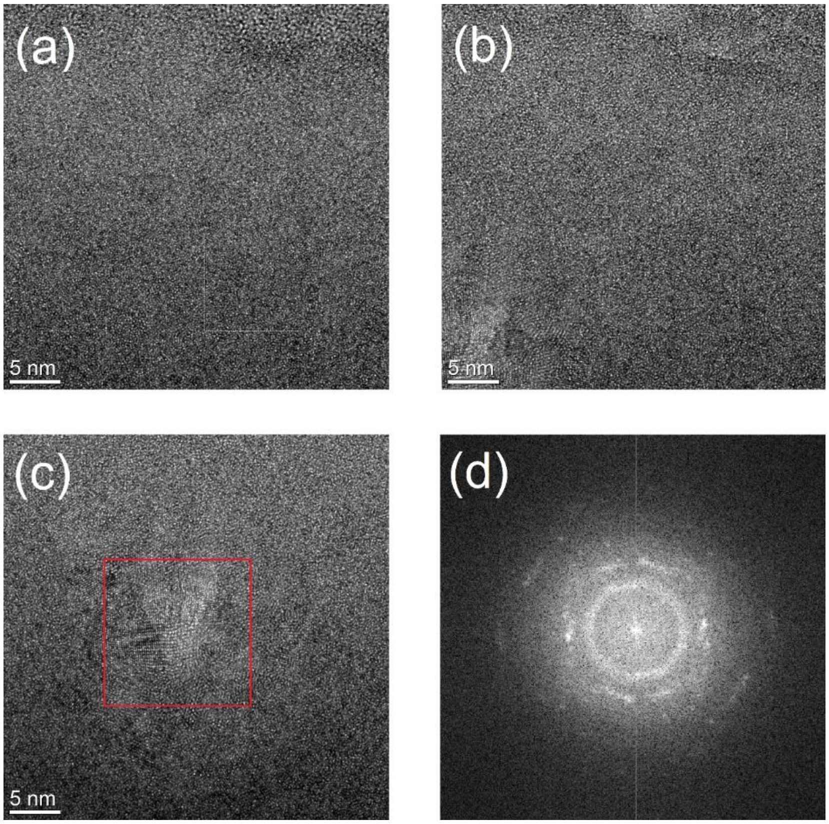

Figure 5.3. HRTEM of the co-sputtered TbFeCo thin films: (a) the original image, (b) image after irradiated for 5 minutes, (c) laser-spot-centered image after irradiated for 5 minutes, (d) FFT image for the reduced-area labeled by the red square in (c).

5.2.2 Perpendicular Magnetic Anisotropy

The amorphous single-sputtered TbFeCo thin films exhibited strong PMA for various compositions. As an example, the single-sputtered $Tb_{29.3}Fe_{59.5}Co_{11.2}$ thin film was measured by VSM at 300 K. Figure 5.4 shows hysteresis loops of both in-plane and out-of-plane orientations. The out-of-plane loop exhibited an obvious square shape, which corresponded to the easy direction of its PMA. Here saturation magnetization could be estimated by the maximum value as 165 emu/cm^3. While, the in-plane curve was tilted and the final saturation had not been reached within 3 Tesla, i.e. the limit of

VersaLab®. Therefore, the strength of PMA could be estimated by $K_u = \frac{1}{2}\mu_0 M_S H_K + \frac{1}{2}\mu_0 M_S^2 \sim 2.6 \times 10^6$ erg/cm^3. The coercivity of both in-plane and out-of-plane was about 4 kOe.

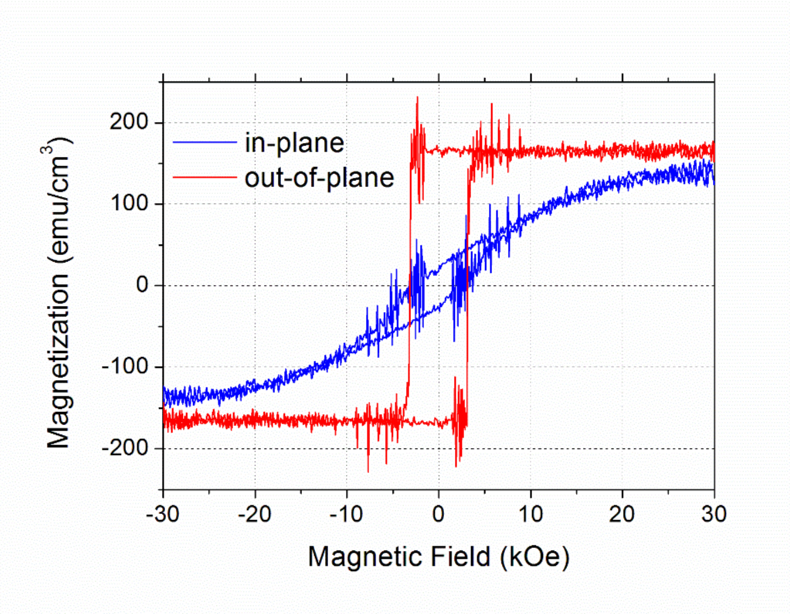

Figure 5.4. In-plane (blue) and out-of-plane (red) hysteresis loops of a 65 nm single-sputtered TbFeCo film at 300 K.

Similarly, the co-sputtered $Tb_{28.8}Fe_{60.8}Co_{10.4}$ thin film also showed a PMA at 300 K. Compared to the single-sputtered TbFeCo, the out-of-plane loop had a smaller saturation magnetization of 45 emu/cm^3 and a larger coercivity of 16 kOe. This large coercivity had been confirmed by MOKE as demonstrated in Figure 5.5 (b). The in-plane loop was a similar tilted "S" shape with a saturation magnetic field of about 25 kOe. The in-plane coercivity was much smaller than the out-of-plane, and the strength of PMA was about 0.6×10^6 erg/cm^3.

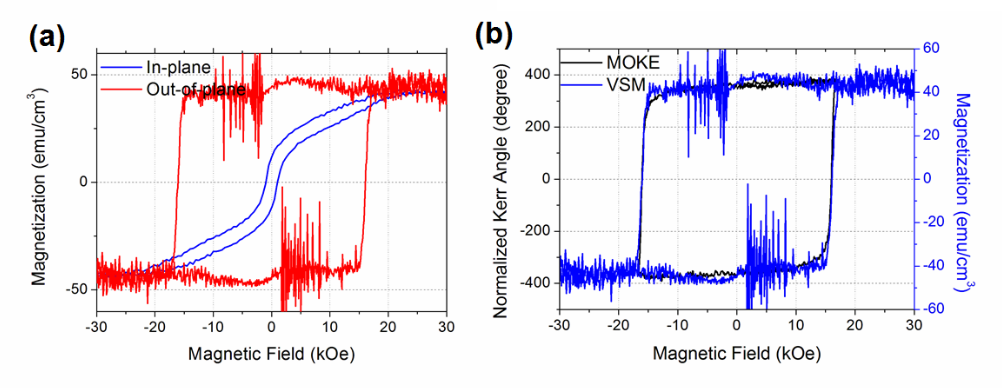

Figure 5.5. Hysteresis loops of a 102 nm co-sputtered TbFeCo film: (a) In-plane (blue) and out-of-plane (red) loops measured by VSM. (b) Out-of-plane loops measured by MOKE (black) and VSM (blue).

Moreover, out-of-plane hysteresis loops of both the single-sputtered and co-sputtered samples were measured at temperatures ranging from 50 K to 350 K. The results are presented in Figure 5.6. It is clear that PMA existed for the whole range of temperatures. The saturation magnetization increased for both samples as the temperature deceased, which indicates their compensation temperature is higher than 350 K. The coercivity of the single-sputtered sample increased monotonically as the system cooled down. But the coercivity of the co-sputtered samples had a minimum coercivity at about 200 K, which indicates its compensation was closer to 350 K than that of the single-sputtered sample. In addition, the square loop shape tended to tilt at a lower temperature for both of the samples.

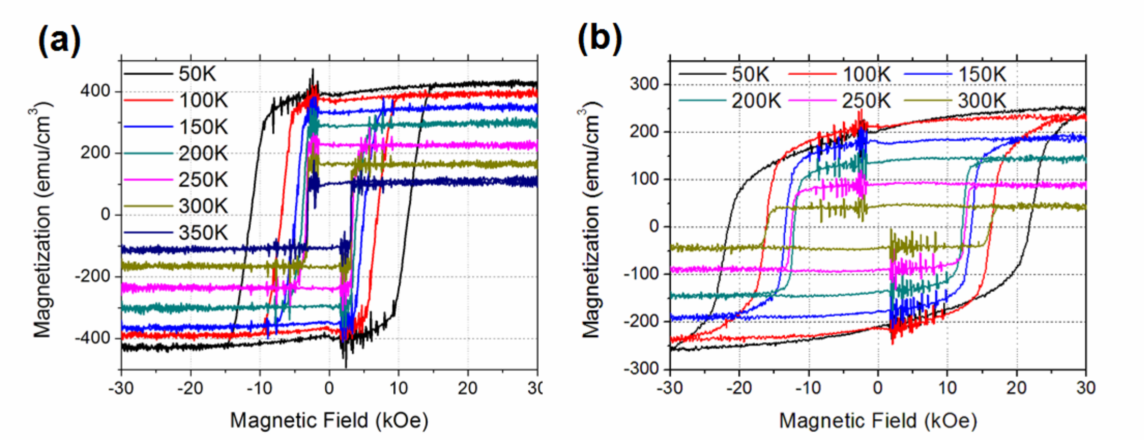

Figure 5.6. Out-of-plane hysteresis loops of single-sputtered (a) and co-sputtered (b) TbFeCo films at different temperatures measured by VSM.

The above results confirm the existence of PMA in both single-sputtered and co-sputtered TbFeCo thin films for temperatures ranging from 50 K to 350 K. However, due to their distinct deposition conditions, the strength of PMA, saturation magnetization and coercivity were obviously different from each other. As is well-known in past research, the single-sputtered sample which was sputtered at a lower Ar pressure, tends to have a denser film morphology. On the other hand, the co-sputtered sample may suffer from both a shadowing effect[31,101,102] and lower ion mobility due to an increasing number of collisions.[101,103] In the following section, thickness-dependent magnetization for both single-sputtered and co-sputtered samples is further examined. A numerical model will be proposed later to fit both of these samples, even though a significant difference exists between the two sets.

5.2.3 Thickness Dependence of Magnetization

The thickness dependence of saturation magnetization was examined through a series of amorphous TbFeCo films that were single-sputtered at an Ar pressure of 1 mTorr with an increasing deposition time. The RF power of the TbFeCo alloy target was kept at 150 W, which corresponded to a composition of $Tb_{26.0}Fe_{62.9}Co_{11.1}$. The saturation magnetization was then plotted as a function of temperature for different thicknesses in Figure 5.7. The sign of the magnetization indicated the orientation of Fe sublattice. For example, at high temperatures, the magnetization was positive, which means that the Fe sublattice would exhibit a positive orientation; at low temperatures, the Tb sublattice was dominated and the Fe sublattice thus pointed to the negative direction. A thickness dependence of saturation magnetization was clearly exhibited in single-sputtered amorphous TbFeCo thin films. The thicker the sample was, the larger the magnetization curve shifted to the right, and the higher the compensation temperature would be, as shown in Table 5.1. Moreover, this thickness dependence tended to saturate for films thicker than 100 nm. Finally, at low temperatures, results showed that all curves converged to the same interception, agreeing with the common composition of all the thicknesses.

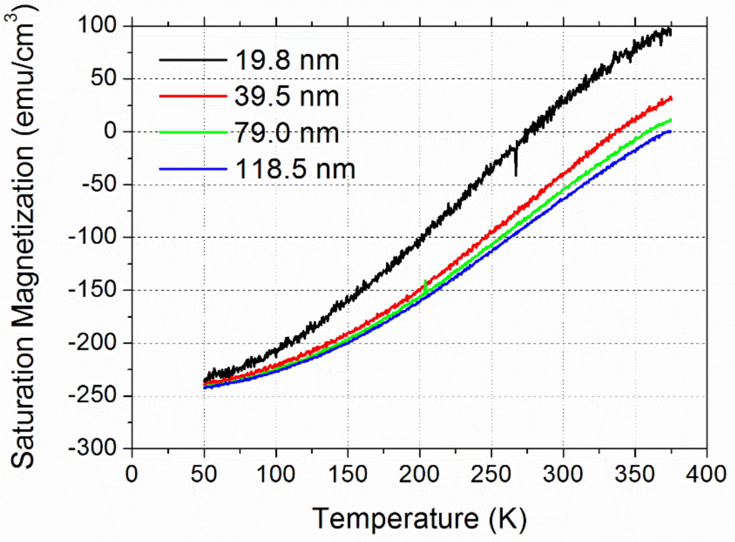

Figure 5.7. Saturation magnetization vs. temperature curves of single-sputtered $Tb_{26.0}Fe_{62.9}Co_{11.1}$ films with different thicknesses measured by VSM.

Similarly, a series of thin films were co-sputtered by Tb and TbFeCo targets at an Ar pressure of 7 mTorr. The RF power of the Tb and TbFeCo targets were 26 W and 100 W, respectively. The composition of these films was characterized as $Tb_{28.1}Fe_{61.0}Co_{10.9}$. As shown in Figure 5.8, a similar thickness dependence of saturation magnetization was observed in the co-sputtered films. The compensation temperature was elevated to a higher value for the thicker sample, which is summarized in Table 5.1.

Table 5.1. Thickness dependence of the compensation temperature for both co-sputtered (left) and single-sputtered (right) TbFeCo films.

Thick (nm)	**T_{comp} (K)**	**Uncertainty**	**Thick (nm)**	**T_{comp} (K)**	**Uncertainty**
14.7	229.7325	1.7645	19.8	277.7203	4.2637
31.2	286.9885	1.4984	39.5	336.3005	1.7472
66.0	321.7299	2.2537	79.0	358.2137	1.7534
101.5	344.4567	1.8389	118.5	371.9871	2.5249

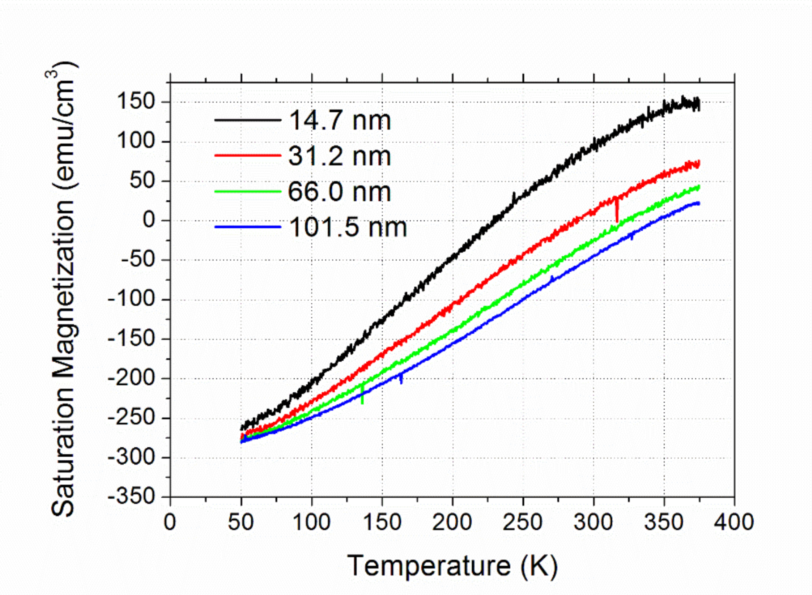

Figure 5.8. Saturation magnetization vs. temperature curves of co-sputtered $Tb_{28.1}Fe_{61.0}Co_{10.9}$ films with different thicknesses measured by VSM.

In Figure 5.9, the compensation temperature of the two sets of samples are plotted as a function of the film thickness. The compensation temperature increased for both sets as the thickness increased. However, the slope of both curves was shown as decreasing and tended to saturate for samples thicker than 100 nm. More interestingly, the compensation temperature of the co-sputtered Tb 28 at. % sample was lower than that of the single-sputtered Tb 26 at. % sample. This finding was inconsistent with the modeling results in Chapter 4, if based on a simple pseudo amorphous structure. This discrepancy implied a morphological difference of the films deposited at distinct conditions. Specifically, the co-sputtered thin films were less dense due to a shadowing effect and lower ion mobility.

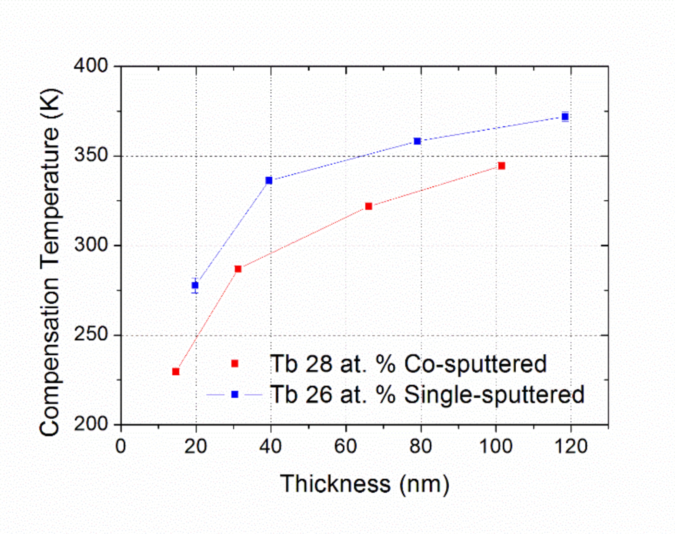

Figure 5.9. Thickness dependence of compensation temperature for both single-sputtered (blue) and co-sputtered (red) TbFeCo films.

5.3 Numerical Study of Thickness Dependence

This section of Chapter 5 will focus on a numerical study of the thickness-dependent magnetization based on an ab initio-generated amorphous structure created by Professor Sheng from George Mason University.[104] Modifications of the original amorphous structure were performed by a random pair swap and a random close pack, in order to obtain an ensemble of random atomistic structures with a different Tb-Fe pair ratio. Finally, this section will end by proposing a depth profile of the Tb-Fe pair ratio to fit the experimental magnetization curves.

5.3.1 Ab Initio Amorphous Structure

A group of researchers, under Professor Sheng from George Mason University, generated an atomistic amorphous structure by an ab initio molecular dynamics calculation, resulting in a structure that has 250 atoms within a box of 1.58 nm × 1.58 nm × 1.58 nm. The insect figure shows a 3D plot of the ab initio amorphous structure of Tb 27.2 at. %. A periodic boundary condition was used for the original structure. As Figure 5.10 shows, the first peak positions of the pair distribution function of Fe-Fe, Fe-Tb and Tb-Tb were 2.51 Å, 2.97 Å and 3.28 Å, respectively. In this study, only the nearest neighbor pairs were considered in the classical Heisenberg model. These pairs were selected based on the longest pair distance, i.e. $d_{max}^{Fe-Fe} < 2.655$ Å, $d_{max}^{Tb-Fe} < 3.045$ Å and $d_{max}^{Tb-Tb} < 3.650$ Å. The coordination number statistics are summarized in Table 5.2, which are comparable to the experimental EXAFS results.[34,35]

Table 5.2. The coordination number statistics of ab initio calculated atomistic amorphous structure from Sheng et al.

	Tb-Tb	**Tb-Fe**	**Fe-Tb**	**Fe-Fe**
Sheng's Structure	3.53 ± 1.07	7.00 ± 2.26	2.62 ± 0.99	5.16 ± 1.58

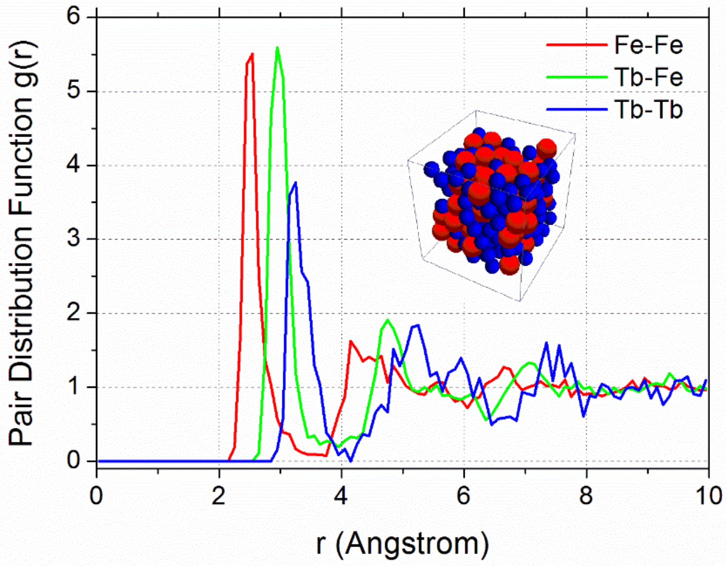

Figure 5.10. Pair distribution function of ab initio calculated atomistic amorphous structure from Sheng et al. The insect figure shows a 3D plot of this structure.

The present study utilizes a particular focus on tuning the amorphous structure while keeping a fixed concentration. To achieve this goal, a pair ratio was defined by the number of the neighbor pairs of interest divided by the total number of neighbor pairs within the system, as presented in the following equation:

$$p_{A-B} \equiv \frac{N_{A-B}}{N_{total}} \tag{5.1}$$

For example, the original ab initio amorphous structure has pair ratios for different neighbor pairs as: $p_{Fe-Fe} = 0.441$, $p_{Tb-Fe} = 0.446$, and $p_{Tb-Tb} = 0.113$.

5.3.2 Random Pair Swap and Random Close Pack

Notoriously noted in past research, the sputtered thin film is not usually found within thermal equilibrium due to fast quenching in the sputter procedure. This fact implies a range of possible structures away from the original ab initio calculation. In this study, an ensemble of different amorphous structures were derived from the ab initio amorphous structure by a minimum amount of random pair swap. Resulting structures were then relaxed by a random close-pack algorithm.

During the random pair swap stage, pseudo energy was defined based on a weighted quadratic sum of the difference between the current and the target pair ratios as shown in the following equation:

$$\begin{aligned} E_{pair} \equiv w_{Fe-Fe}\left(p_{Fe-Fe} - p_{Fe-Fe}^{target}\right)^2 + w_{Tb-Fe}\left(p_{Tb-Fe} - p_{Tb-Fe}^{target}\right)^2 \\ + w_{Tb-Tb}\left(p_{Tb-Tb} - p_{Tb-Tb}^{target}\right)^2 \end{aligned} \quad (5.2)$$

Here, neighbor pairs were randomly swapped by the Metropolis sampling algorithm at a finite pseudo temperature. This procedure was terminated immediately after a threshold energy difference was reached, in order to introduce a minimum modification.

After swapping pairs, it was necessary to relax the system due to the different radius of Tb and Fe atoms. In this stage, a random close-pack algorithm was adopted in order to relax the system. This algorithm was introduced by Desmond et al.[105,106] Figure 5.11 provides a flow chart of this random close-pack algorithm. It should be noted that, this flow chart itself only represents a single iteration of the whole procedure. In order to have a packing ratio close to 0.64, multiple such iterations may be required for relaxing larger scale structures.

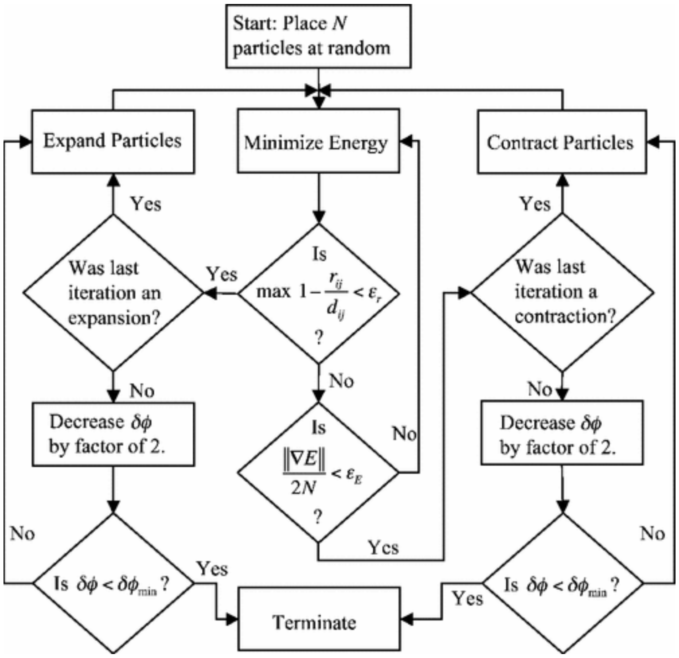

Figure 5.11. Flow chart of the random close-pack algorithm. From Desmond et al.[105]

After the two stages of pair swap and close pack an ensemble of atomistic structures, e.g. 1,080 different structures for each Tb concentration, were prepared with different pair ratios. For simplicity, from now on only Tb-Fe pair ratio is mentioned due to its importance for antiferromagnetic coupling as described in Chapter 4. Figure 5.12 plots a series of example structures with Tb-Fe pair ratios ranging from 0.25 to 0.50 for Tb 26 at. %.

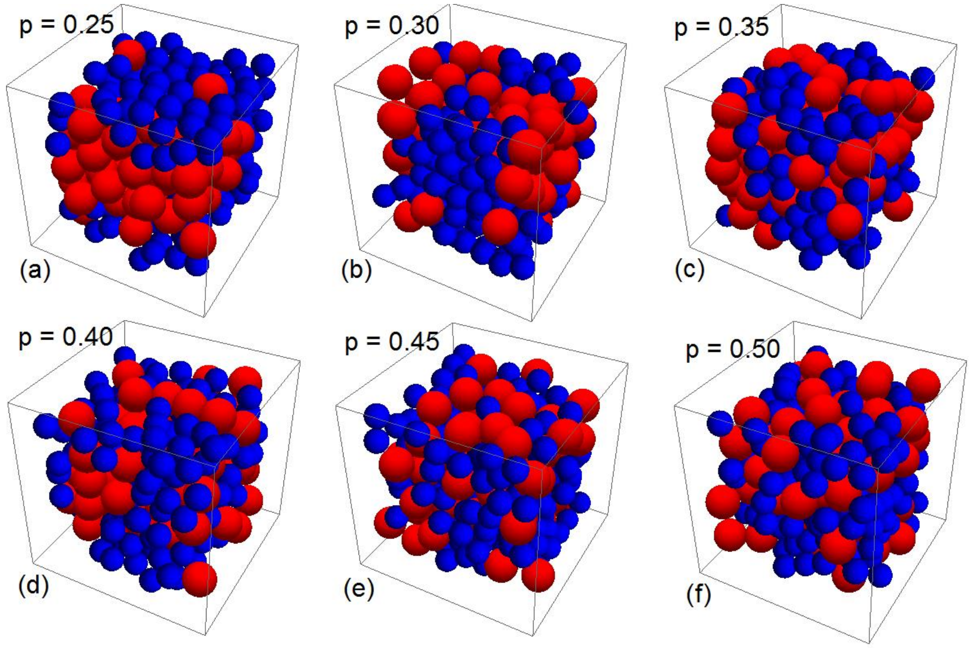

Figure 5.12. Example structures with Tb-Fe pair ratios ranging from 0.25 to 0.50 for Tb 26 at. %. The box size is 1.58 nm × 1.58 nm × 1.58 nm.

5.3.3 Amorphous Structure with Uniform Tb-Fe Pair Ratio

Before handling the heterogeneous structures, amorphous structures were first considered with a uniform Tb-Fe pair ratio. The atomistic simulations were based on the parallel tempering algorithm, and the simulation parameters are listed in Table 5.3. As shown in Figure 5.13 and Figure 5.14, the magnetization of both Tb at. 26% and Tb at. 28% had a significant dependence on the Tb-Fe pair ratio. This can be explained by the tuning of the antiferromagnetic coupling similar to the direct tuning of J_{RE-TM}, which was explored in Chapter 4. In this example, all curves converged at the same point due to the same ground state for each concentration.

Table 5.3. Simulation parameters for the parallel tempering functionality of the MMP.

Parameter	**Value**	**Parameter**	**Value**
μ_{Tb}	9.34 μB	λ_{Tb}	0.1
μ_{Fe}	2.217 μB	λ_{Fe}	0.1
J_{Tb-Tb}	0.993×10^{-21} J/link	γ_{Tb}	1.76×10^{11} radT^{-1}s^{-1}
J_{Fe-Fe}	7.08×10^{-21} J/link	γ_{Fe}	1.85×10^{11} radT^{-1}s^{-1}
J_{Tb-Fe}	-1.41×10^{-21} J/link	Structure Duplication	6 × 6 × 6
D	3.05×10^{-23} J/atom	Boundary Condition	Periodic

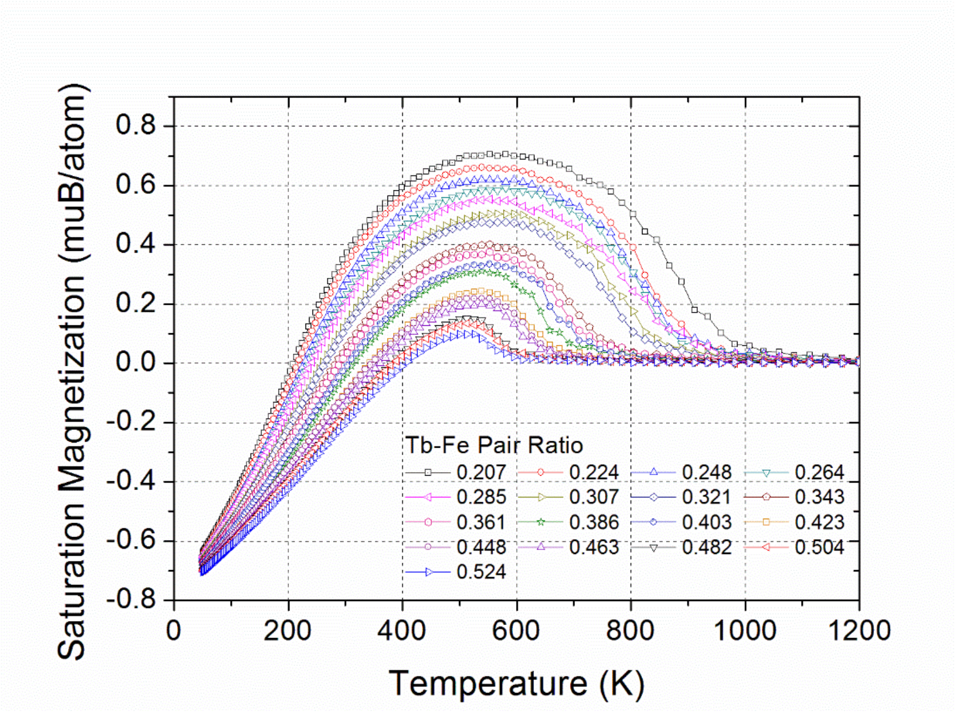

Figure 5.13. Saturation magnetization vs. temperature curves of amorphous $Tb_{26}Fe_{74}$ with uniform Tb-Fe pair ratios ranging from 0.20 to 0.52.

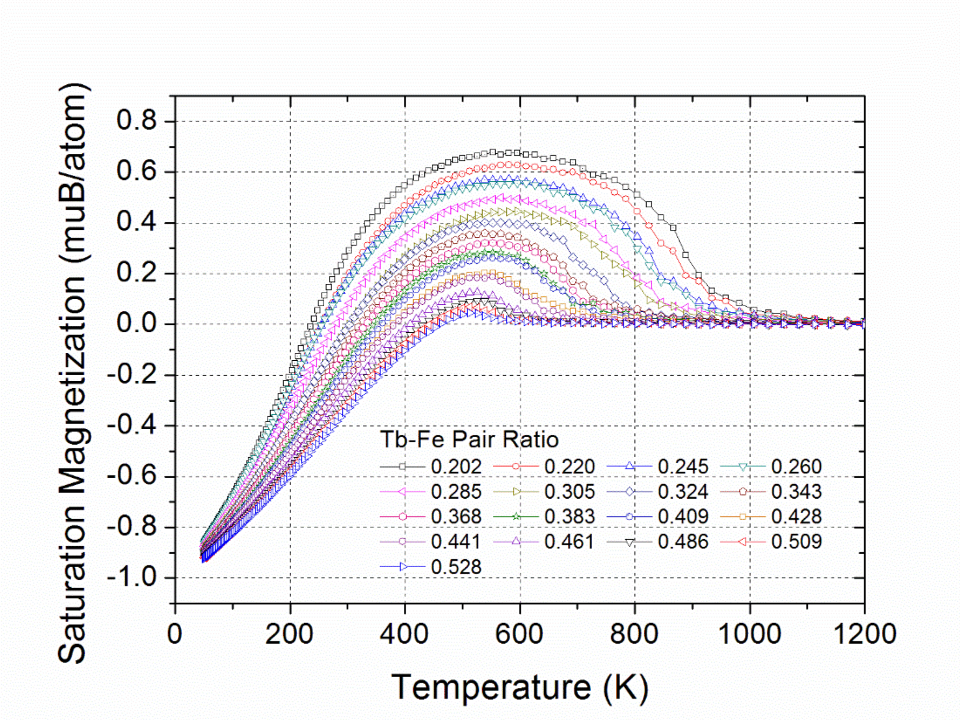

Figure 5.14. Saturation magnetization vs. temperature curves of amorphous $Tb_{28}Fe_{72}$ with uniform Tb-Fe pair ratios ranging from 0.20 to 0.53.

Figure 5.15 presents an analysis of the compensation temperature as a function of the Tb-Fe pair ratio. For both concentrations the relationship could be fitted nicely by a quadratic curve. Moreover, given that real films were sputtered at different conditions, the compensation temperature of Tb 28 at. %, which was co-sputtered at 7 mTorr, could be further reduced due to its lower density and fewer average coordinating neighbors. As reported by Li et al.[103], the density of the film sputtered at 3.4 mTorr was only 90% of the film that was sputtered at 1.1 mTorr. Here, by a similar reduction of 0.9, the compensation curve of Tb 28 at. % was very close to that of Tb 26 at. % which was single-sputtered at 1 mTorr.

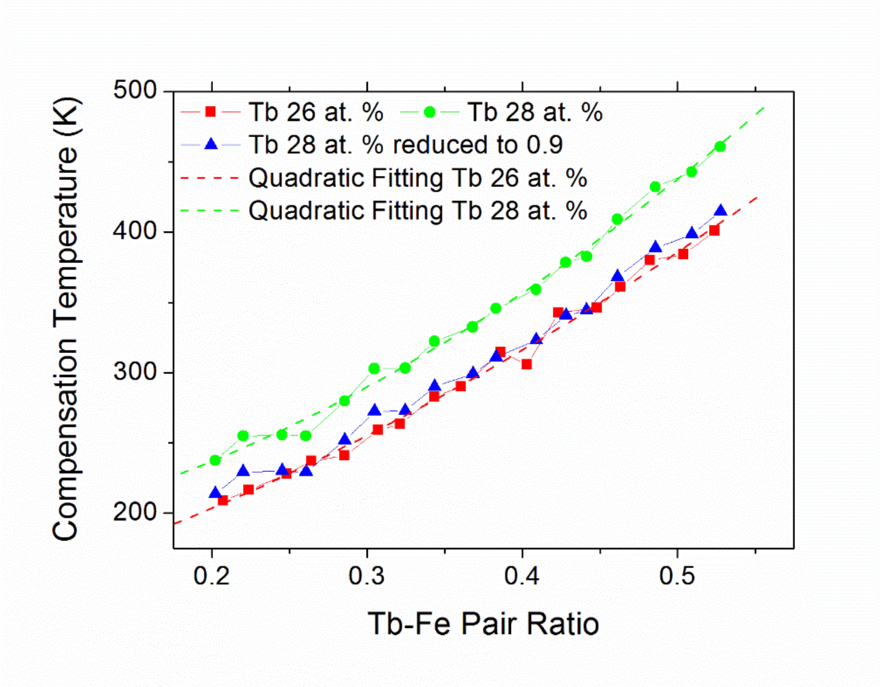

Figure 5.15. Analysis of the compensation temperature as a function of the Tb-Fe pair ratio.

5.3.4 Amorphous Structure with Tb-Fe Pair Depth Profile

Amorphous structures with a depth profile of Tb-Fe pair ratio were designed for both sets of thin films, assuming that the compensation temperature depended on the average Tb-Fe pair ratio of the overall sample. As shown in Figure 5.16, a curve of average Tb-Fe pair ratio in terms of the film thickness could be derived from the experimental compensation temperature curve based on the quadratic fitting previously discussed. Finally, a layered Tb-Fe pair ratio was plotted for the single-sputtered Tb 26 at. % films.

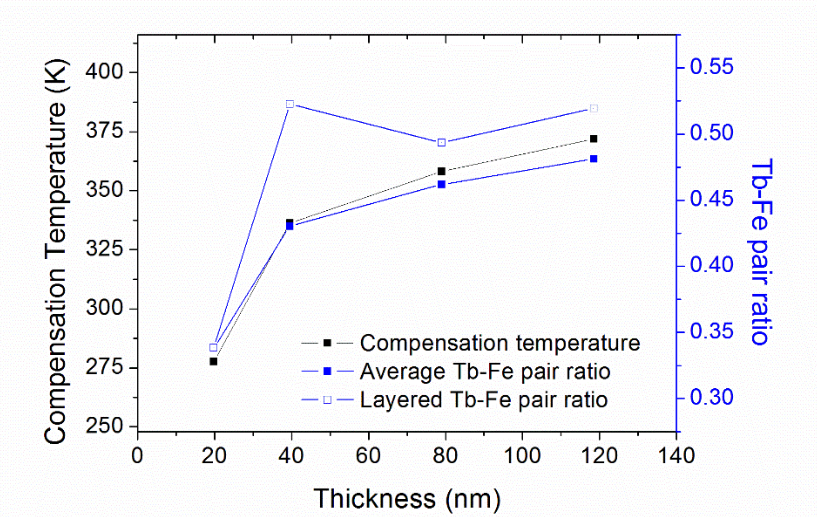

Figure 5.16. Thickness dependence of compensation temperature and Tb-Fe pair ratio of single-sputtered Tb 26 at. % films.

For simplicity, a stepwise Tb-Fe pair depth profile was applied when building the final amorphous atomistic structure, as demonstrated in Figure 5.17. The Tb concentration was designed as a uniform function for the whole thickness, the full structure being 10 nm × 10 nm × 79 nm large and containing 450,000 atoms. Periodic boundary conditions were applied in both the x and y axes, while a free-boundary condition was used for the z axis.

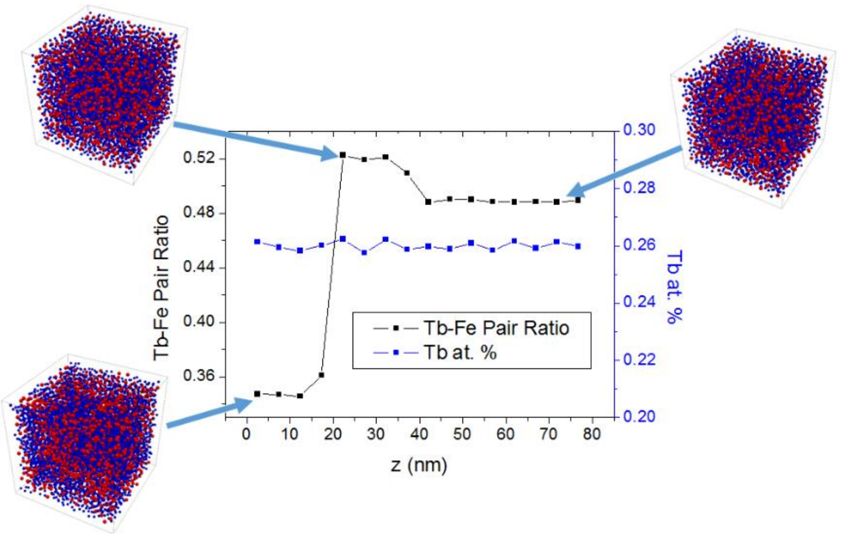

Figure 5.17. Depth profile of Tb-Fe pair ratio and Tb at. % of the atomistic structure for single-sputtered Tb 26 at. % thin films.

A series of numerical simulations were performed using parallel tempering for different thicknesses. Figure 5.18 summarizes the results, comparing them with experimental data. The empirical modeling results clearly agreed with the experiments. Figure 5.18 (a) confirmed the previous assumption that the compensation temperature was directly determined by the overall Tb-Fe pair ratio. In Figure 5.18 (b), modeling curves overlapped experimental curves in the temperatures higher than 200 K. When approaching lower temperatures, due to the large coercivity and tilting hysteresis loop, the saturation magnetization was possibly underestimated. Moreover, the differences exhibited at low temperatures may also be due to the fact that the model was built in nanoscale and no domain dynamics were considered.

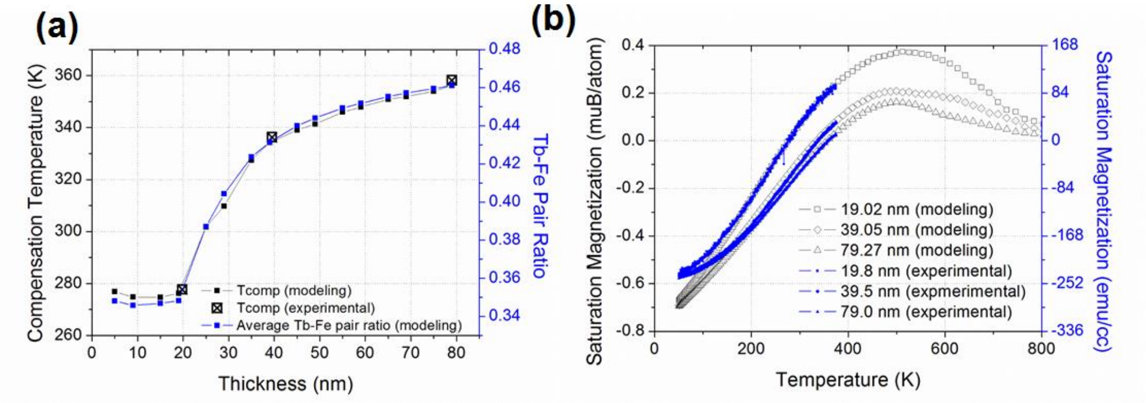

Figure 5.18. Thickness dependence of compensation temperature and saturation magnetization curves of single-sputtered Tb 26 at. % films: (a) compares the modeling and experimental compensation temperature of different thicknesses. (b) compares the modeling and experimental saturation magnetization curves for three different thicknesses.

Using the same method, as shown in Figure 5.19, a depth profile of Tb-Fe pair ratio was designed for the co-sputtered Tb 28 at. %. The largest dimension was 10 nm × 10 nm × 66 nm and contained a total of 378,000 atoms. The depth profile and Tb concentration are plotted in Figure 5.20.

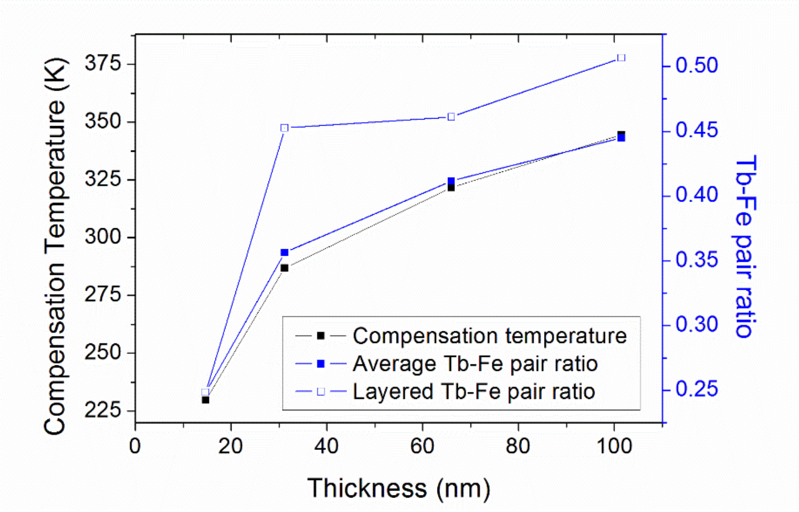

Figure 5.19. Thickness dependence of compensation temperature and Tb-Fe pair ratio of co-sputtered Tb 28 at. % films.

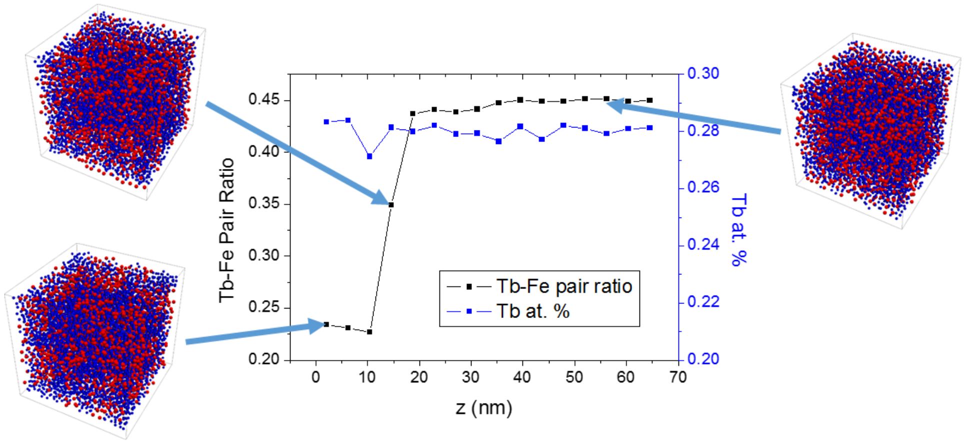

Figure 5.20. Depth profile of Tb-Fe pair ratio and Tb at. % of the atomistic structure for co-sputtered Tb 28 at. % thin films.

As shown in Figure 5.21 (a) and (b), the numerical results were very consistent with the corresponding experimental observations.

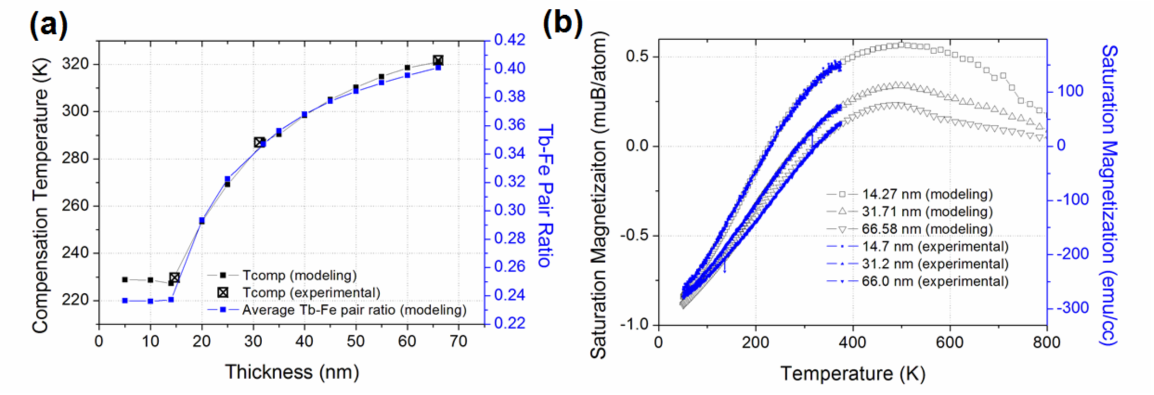

Figure 5.21. Thickness dependence of compensation temperature and saturation magnetization curves of co-sputtered Tb 28 at. % films: (a) compares the modeling and experimental compensation temperature of different thicknesses. (b) compares the modeling and experimental saturation magnetization curves for three different thicknesses.

5.4 Concluding Remarks

In this chapter, a large PMA has been verified for a wide range of temperatures in both the single-sputtered and the co-sputtered amorphous TbFeCo thin films. The temperature dependence of the saturation magnetization has been measured by VSM experimentally, showing a tunable compensation temperature near the room temperature. Specifically, an obvious thickness dependence has been confirmed in both the single-sputtered and the co-sputtered sample sets of increasing thicknesses, where higher compensation temperatures have been consistently observed for thicker films.

An atomistic model, based on an ab-initio amorphous structure, has been proposed to better understand the experimental thickness dependence. A depth profile of the Tb-Fe pair ratio has been introduced by a minimum modification through a random pair swap and a random close pack. This model effectively explains the thickness dependence of both sample sets on equal footing. Consistent temperature dependent magnetization curves have been predicted and compared to the experimental observations. This study numerically confirmed the possibility of depth profiles of heterogeneous structures in the sputtered amorphous thin films.

CHAPTER 6 EXCHANGE BIAS IN CO-SPUTTERED AMORPHOUS RE-TM THIN FILMS

6.1 Introduction

The exchange bias (EB) effect, as introduced in the second chapter, describes a unidirectional shift of a magnetic hysteresis loop along the magnetic field axis. Recently the EB effect has received intensive interest because of its importance in a variety of technological applications, especially in spin-valve devices and magnetic tunnel junctions.[13,38,48,50,107–109] The exchange anisotropy has been interpreted in terms of the exchange interaction across the ferromagnetic (FM)-antiferromagnetic (AFM) interface, e.g. in Co/IrMn.[39,40,110] EB also exists in soft/hard FM/FM systems, where two types of EB have been reported, i.e. the minor loop effect and the standard EB effect.[111,112] Moreover, enhanced EB has been observed using compensated ferrimagnetic (FiM) materials, e.g. $GdCo_2$-Co and TbFe-[Co/Pt].[44,45] Recently, polycrystalline Heusler compounds Ni-Mn-*X* (*X* = Sn, In, Sb) and Mn-Pt-Ga have been reported to show an intrinsic EB at low temperatures due to the coexistence of FM and AFM regions.[48–50,113] However, ongoing efforts are still in progress of attempting to engineer more desirable properties, such as high Néel temperature, large magnetic anisotropy and suitable chemical and structural tunability. In this study, the amorphous rare-earth-transition-metal (RE-TM) thin film is presented as one promising material-base that provides wide compositional tunability and requires no epitaxial growth.

Amorphous TbFeCo thin films were characterized in Chapter 5 with strong perpendicular magnetic anisotropy (PMA). Moreover, the thickness-dependent magnetization implies anisotropic microstructures, which have also been reported in other room-temperature sputter-deposited thin films.[31,101,102] Compositional inhomogeneities that are formed by a shadowing effect, when separate sources are used for multi-target co-sputtering deposition, are worthy of special attention. These growth-induced inhomogeneities provide an opportunity to manipulate the magnetic properties of the amorphous thin film.

This chapter explores EB and an accompanied bistable magneto-resistance (MR) states that were uncovered at room temperature in the amorphous TbFeCo thin films. Two growth-induced nanoscale phases have been observed by atom probe tomography (APT) and aberration-corrected scanning transmission electron microscopy (STEM). The EB originates from the exchange interaction between the FI and FM components that correspond to the two nanoscale phases respectively. The bistable MR states can also be understood in light of the same exchange interaction. Finally, a modeling study on EB in the ferrimagnetic system predicts consistent temperature dependence in the exchange-biased hysteresis loop, which provides numerical supports to the experimental two-phase model.

6.2 Experimental Results of Co-sputtered Tb(Sm)FeCo Thin Films

6.2.1 Sample Preparation

Amorphous $Tb_{26}Fe_{64}Co_{10}$ and $Tb_{20}Sm_{15}Fe_{55}Co_{10}$ thin films were prepared on thermally oxidized Si substrates by RF magnetron sputtering. The TbFeCo films were deposited at room temperature by co-sputtering from TbFeCo alloy and Tb elementary targets under a constant Ar pressure of 7 mTorr. The TbSmFeCo films were also deposited at room temperature from TbFeCo alloy, Tb elementary and Sm elementary targets under the same Ar pressure. The total deposition rate was adjusted to about 1.2 Å/s. Compositions were then determined by energy-dispersive X-ray spectroscopy (EDS) in an FEI Quanta 650 scanning electron microscope (SEM) and confirmed by atom probe tomography (APT). A series of films were made with thicknesses of 50, 100, 150 and 200 nm. These samples were capped by a 5 nm thick Ta layer to prevent oxidation.

6.2.2 Structural Characterization

High-resolution transmission electron microscopy (HRTEM) has been used to characterize the amorphous structure of the co-sputtered TbFeCo and TbSmFeCo thin film. As shown in Figure 5.2 and Figure 6.1, a typical pattern of amorphous structure was provided by the cross sectional HRTEM image, and the fast Fourier transform (FFT) image indicated no apparent presence of crystallinity, similar to that reported previously.[100,114]

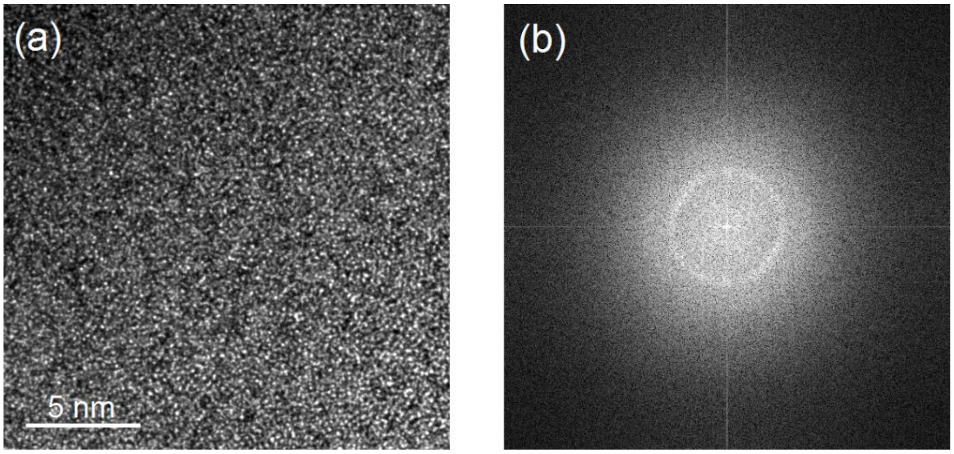

Figure 6.1. HRTEM image (a) and its FFT image (b) of co-sputtered TbSmFeCo thin film.

To characterize the compositional uniformity, high-angle annular dark field imaging (STEM-HAADF) have been conducted on the TbFeCo film. Figure 6.2 (a) shows a representative STEM-HAADF micrograph. The non-uniform contrast of the image indicates local compositional fluctuations. STEM-EDS was utilized to further validate the STEM-HAADF observations. Figure 6.2 (b-e) shows the HAADF signal and maps of the Co *K*, Tb *L*, and Fe *K* edges that were taken around one such cluster. These maps have had their background removed and overlapping edges deconvoluted. Qualitatively, the distribution of all three signals is clearly non-uniform. Focusing specifically on the Tb *L* and Fe *K* edges, we see that in the regions marked with arrows there is a local depletion in Tb that directly coincides with enrichment in Fe. This suggests that the distribution of these two elements is inversely related. A composite map of the Tb *L* and Fe *K* edges (Figure 6.2 (f)) shows this with more clarity thus supporting the conclusion that local Fe enrichment is associated with local Tb depletion on the length scale of 2 - 5 nm.

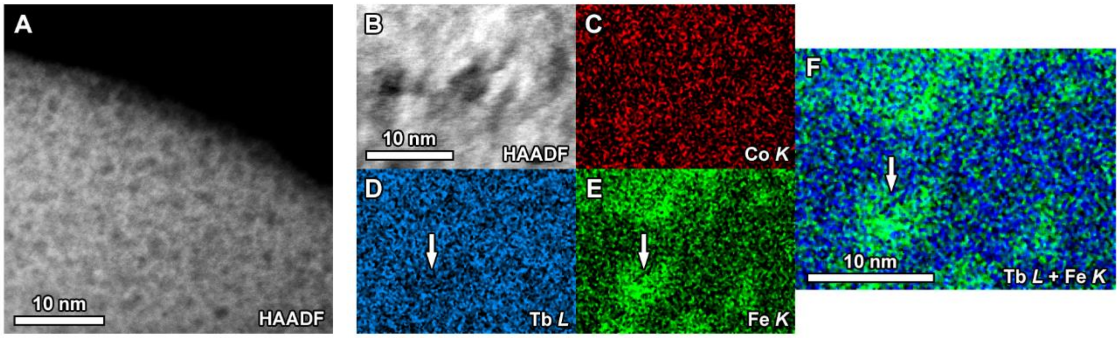

Figure 6.2. Correlative STEM analysis. (a) Representative STEM-HAADF micrograph exhibiting non-uniform contrast due to clustering. (b)–(e) STEM-EDS maps of the HAADF, Co *K*,Tb *L*, and Fe *K* signals, respectively, around one such cluster. (f) Composite of the Tb *L* and Fe *K* edges. Published by Li et al.[115]

Additionally, atom probe tomography (APT) was also performed by research collaborators in PNNL. APT is capable of providing information on the 3D nanoscale distribution of elements in amorphous thin films, permitting quantitative measurements that express uniformity of elemental distribution, which can complement the qualitative observations by 2D STEM-EDS mapping.[73–75] APT was used to analyze a 3D volume of 67.66 × 66.13 × 99.89 nm, as shown in Figure 6.3 (a) while Figure 6.3 (b-d) plot 3D elemental distributions. Tb (blue), Fe (green) and Co (red) distribution along a 5 nm slice parallel to the film plane is shown in Figure 6.3 (e-g). These maps clearly show a continuous network-like segregation of all three elements.

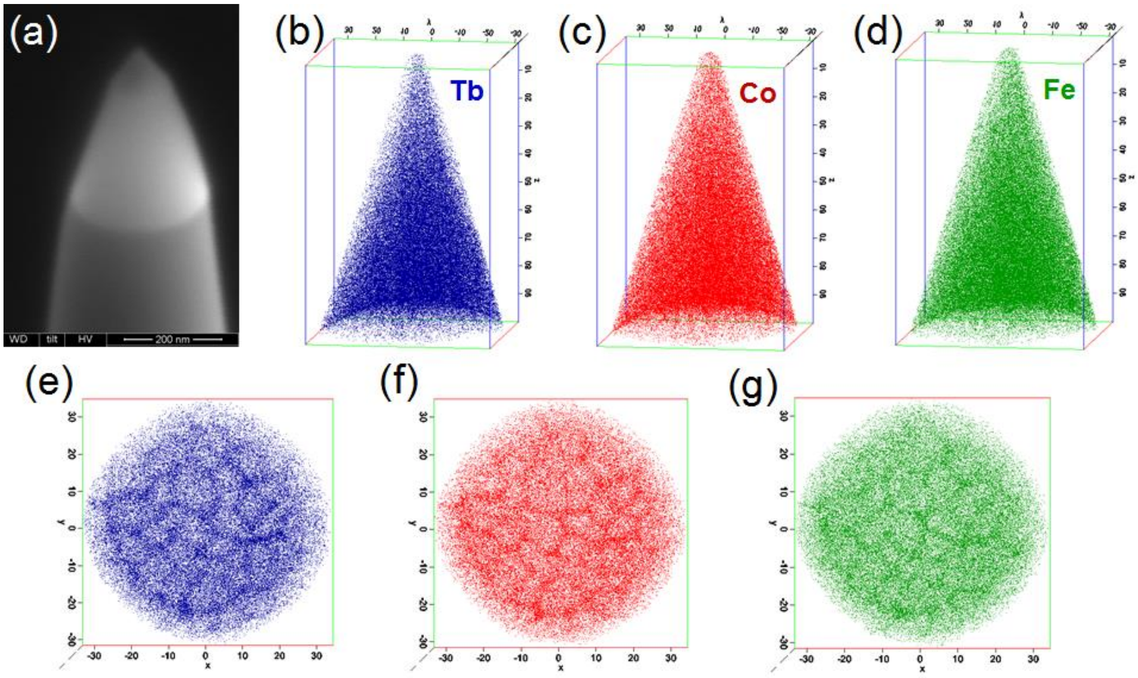

Figure 6.3. APT analysis. (a) SEM image of the sharp tip of the specimen. (b)-(d) Tb (blue), Co (red) and Fe (green) distribution in the 67.66 × 66.13 × 99.89 nm volume analyzed by APT. (e)-(g) 5 nm slice of APT data perpendicular to z axis showing Tb (e), Fe (f), and Co (g) distribution parallel to the film plane. Published by Li et al.[115]

A 1 × 30 × 30 nm volume region highlighted by the gray rectangle in Figure 6.4 (j) was selected to plot 2D concentration elemental maps to obtain a quantitative distribution. In all three 2D maps provided in Figure 6.4 (k-m) red indicates the highest concentration regions and blue indicates the lowest. These results clearly show that Tb segregates to distinct regions, which are depleted in Fe and Co. Figure 6.4 (h) plots a highly disordered iso-composition surface of Tb 27 at. %. Typical concentration line profiles are presented in Figure 6.4 (i) from a Fe rich region to a Tb rich region. These observations directly correlate with the STEM-EDS measurements, which supports the existence of a two-phase compositional partitioning in the TbFeCo thin film.

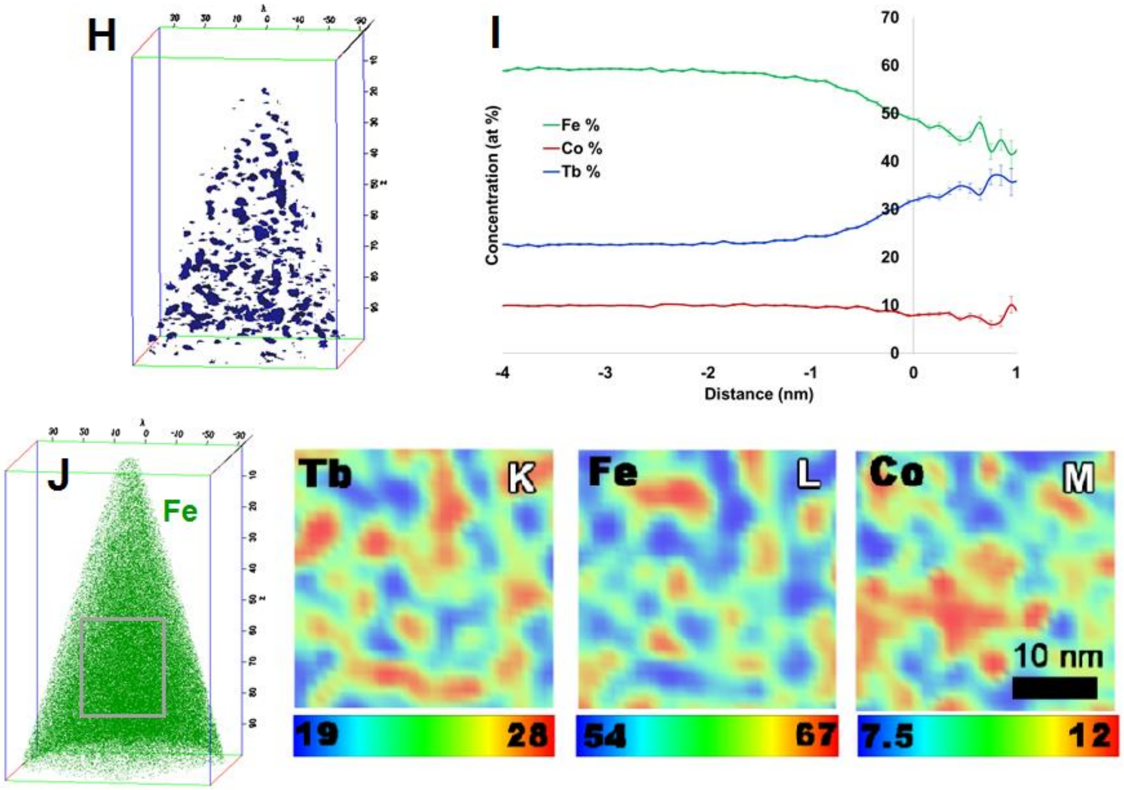

Figure 6.4. APT analysis continued. (h) Tb 27 at. % iso-composition surface. (i) Compositional line-profiles between a Fe rich region and a Tb rich region. (j) Fe (green) distribution analyzed by APT. (k)–(m) 2D concentration maps of Tb (k), Fe (l), and Co (m) plotted on a 1 × 30 × 30 nm volume shown by the dashed rectangle in (j). The dark red and dark blue colors show the highest and lowest concentration regions, respectively. The scale bar indicates the corresponding high and low concentrations for each map. Published by Li et al.[115]

6.2.3 Exchange Bias in Co-Sputtered Tb(Sm)FeCo Thin Films

6.2.3.1 Co-Sputtered TbFeCo Thin Films

TbFeCo films, as previously discussed in Chapter 5, exhibited strong PMA for a wide range of temperatures. Magnetic hysteresis loops of the 100 nm TbFeCo film were characterized by VSM as a function of temperature from 100 to 375 K, from which the temperature dependence of saturation magnetization (M_S) and coercivity (H_C) were extracted. As shown in Figure 6.5, the

Curie temperature (T_C) of the system is greater than 375 K. M_S is expected to reach a minimum at T_{comp}, which is near 250 K.

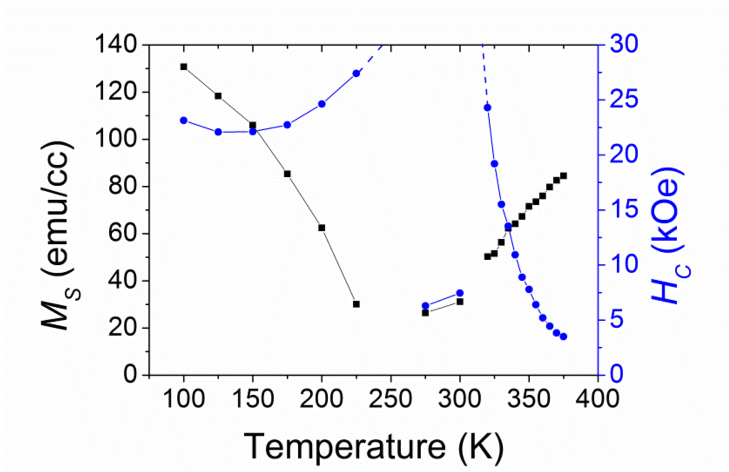

Figure 6.5. Temperature dependence of M_S (black) and H_C (blue) of the amorphous $Tb_{26}Fe_{64}Co_{10}$ thin film. The reduced H_C at 275 and 300 K is related to the exchange bias. Hysteresis loops at 300 K are provided in Figure 6.6 (a). Published by Li et al.[115]

Figure 6.6 (a) shows hysteresis loops in the out-of-plane direction for three distinct temperature regions: well-below, near, and well-above T_{comp}. Two exchange-biased hysteresis loops have been observed at 300 K in the region near T_{comp}. Both of the biased loops have the absolute EB field ($|H_E|$) of 1.9 kOe. The observed EB can be either positive or negative depending on the sample initialization condition. The biased loop with negative H_E was initialized by heating the sample to 355 K in zero field, followed by magnetizing it in +30 kOe and finally cooling it down to the original temperature of 300 K in zero field. On the other hand, the biased loop with positive H_E was initialized by first cooling the sample down to 175 K in zero field, and then magnetizing it in +30 kOe and finally heating it up to 300 K in zero field. Here the EB vanished at temperatures well-below and well-above T_{comp}, namely 175 and 355 K.

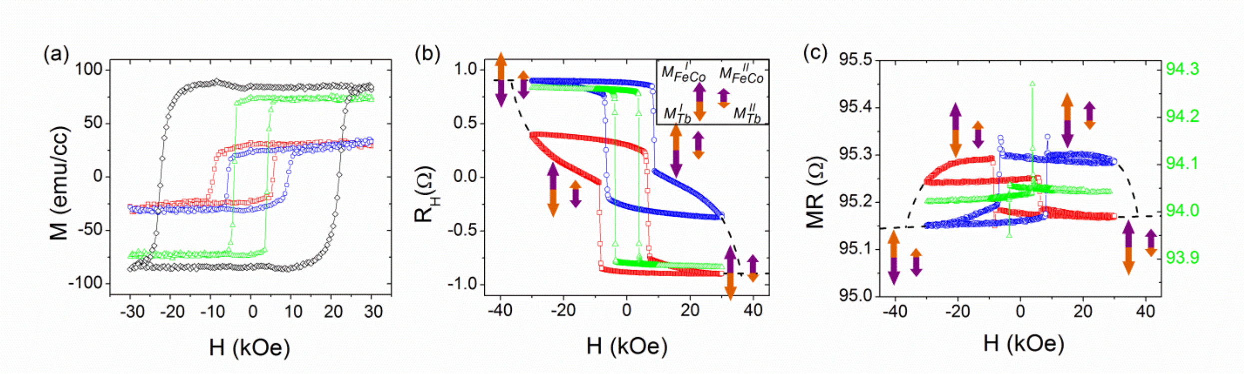

Figure 6.6. Magnetic and magneto-transport measurements of the amorphous $Tb_{26}Fe_{64}Co_{10}$ thin film. a) Out-of-plane magnetic hysteresis loops at 175 K (black), at 355 K (green), and at 300 K (red and blue). The red loop corresponds to samples initialized under 355 K and +30 kOe, while the blue loop for 175 K and +30 kOe. b-c) AHE and MR measurements of the 50 μm Hall bar at 355 K (green) and 300 K (red and blue). The red and blue color indicate the same initialization conditions as (a). Arrow pairs are sketched side by side in (b-c) depicting magnetic moment orientations. The inset of (b) shows an example of the magnetic configuration. The left pair indicates the near-compensated Phase I ($\boldsymbol{M}_{Tb}$(I) and $\boldsymbol{M}_{FeCo}$(I)), and the right for the uncompensated Phase II ($\boldsymbol{M}_{Tb}$(II) and $\boldsymbol{M}_{FeCo}$(II)). In each pair the purple arrow represents $\boldsymbol{M}_{FeCo}$, and the orange for $\boldsymbol{M}_{Tb}$. Dash lines are sketched in (b-c) to indicate the major loop enveloping the two biased loops. Published by Li et al.[115]

To further exploit the EB effect, the magneto-transport behaviors were characterized on TbFeCo Hall bar devices.[100] Theoretically, the anomalous Hall effect (AHE) can be expressed as $R_H \propto R_{Tb}M_{Tb} + R_{FeCo}M_{FeCo}$, where R_{Tb} and R_{FeCo} are AHE coefficients, and M_{Tb} and M_{FeCo} are magnetizations.[116] Past research proves that in amorphous FM materials, R_{Tb} is positive, while R_{FeCo} is negative.[23] Since M_{Tb} and M_{FeCo} also have opposite signs, the AHE terms of Tb and FeCo actually contribute with the same sign, unlike their compensated contributions to magnetic hysteresis loops. Figure 6.6 (b) shows the AHE loops at 300 and 355 K. The loop at 355 K orients opposite to the magnetic hysteresis loop, because the dominant M_{FeCo} has a negative R_{FeCo}. Similarly, two exchange-biased AHE loops were detected at 300 K, which correlated to the two above-mentioned initialization conditions. Moreover, the two biased AHE loops shifted away from each other along the R_H axis.

Finally, the transverse magneto-resistance (MR) was measured using a four-point probe method. The magnetic field was applied perpendicularly to the film plane. Current was applied to the film plane and perpendicular to the magnetic field. As shown in Figure 6.6 (c), at 355 K, two sharp anti-symmetric peaks were observed in the coercive fields of the corresponding AHE loop. Similar results have been reported in other PMA systems, e.g. Pt/Co multilayers.[117] This type of MR peak relates to the multi-domain configuration during the magnetization reversal process. In addition to the sharp anti-symmetric peaks, unusual biased MR loops were revealed at 300 K. The MR difference for the Hall bar of 50 μm width is about 0.1 Ω with a relative change of 0.1 %. These biased MR loops have the same H_E and sample initialization dependence as the AHE and the magnetic hysteresis loops. This implies that the biased MR loops are also associated with the EB effect.

6.2.3.2 Co-Sputtered TbSmFeCo Thin Films

The EB effect of the amorphous $Tb_{26}Fe_{64}Co_{10}$ thin film was also tuned by adding Sm. The co-sputtered amorphous $Tb_{20}Sm_{15}Fe_{55}Co_{10}$ thin film has exhibited strong PMA, and a more significant EB effect compared to the TbFeCo. Figure 6.7 (a) shows hysteresis loops of the TbSmFeCo in the out-of-plane direction at 275 K. Similar to the TbFeCo, there are two exchange-biased magnetic hysteresis loops. The biased loop exhibiting a negative H_E was initialized by magnetizing the sample at 300 K in +30 kOe, followed by cooling the sample down to 275 K in zero field. On the other hand, the biased loop with positive H_E was initialized by magnetizing the sample at 300 K in -30 kOe, followed by cooling it down to 275 K in zero field. Both of the biased loops have $|H_E|$ of 6.4 kOe, which is over three times larger than $|H_E|$ of the TbFeCo (1.9 kOe).

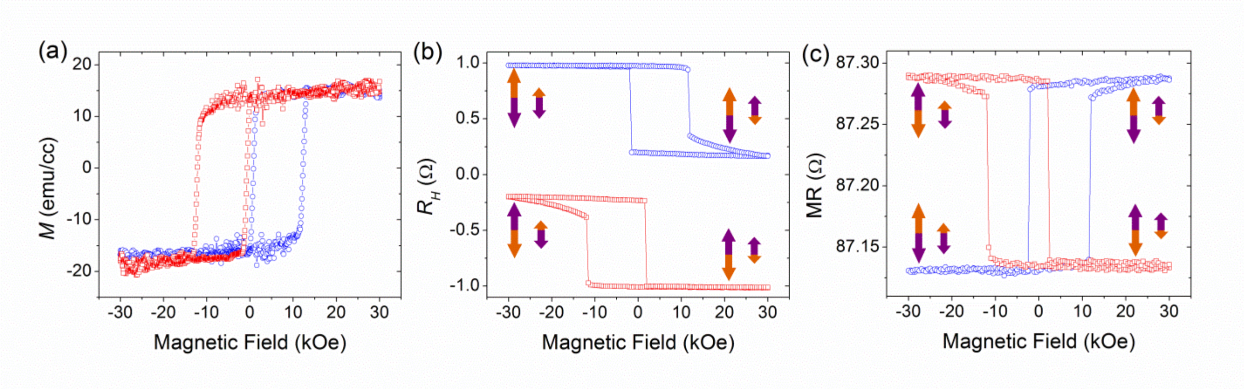

Figure 6.7. Magnetic and magneto-transport measurements of the amorphous $Tb_{20}Sm_{15}Fe_{55}Co_{10}$ thin film. a) Out-of-plane magnetic hysteresis loops at 275 K. b) AHE measurements of 50 μm Hall bar at 275 K. c) The transverse MR measurements of 50 μm Hall bar in the perpendicular external field at 275 K. In (a-c), the red loop corresponds to samples initialized under 300 K and +30 kOe, while the blue loop corresponds initialized under 300 K and -30 kOe. Arrow pairs are sketched side by side in (b-c) depicting magnetic moment orientations. The left pair indicates the near-compensated Phase I ($\boldsymbol{M}_{\mathrm{RE}}$(I) and $\boldsymbol{M}_{\mathrm{TM}}$(I)), and the right for the uncompensated Phase II ($\boldsymbol{M}_{\mathrm{RE}}$(II) and $\boldsymbol{M}_{\mathrm{TM}}$(II)). In each pair the purple arrow represents $\boldsymbol{M}_{\mathrm{TM}}$ and the orange for $\boldsymbol{M}_{\mathrm{RE}}$. Published by Li et al.[115]

Figure 6.7 (b) presents the AHE at 275 K of the TbSmFeCo Hall bar device. Similar to the magnetic loops, two exchange-biased AHE loops with negative and positive H_E were observed at 275 K, and corresponded to the two initialization conditions, i.e. 300 K in +30 kOe and 300 K in -30 kOe respectively. Same as the AHE of the TbFeCo Hall bar device, the two biased AHE loops shifted away from each other along the R_H axis. Biased MR loops were also observed in the TbSmFeCo. As demonstrated in Figure 6.7 (c), at 275 K, the MR difference for the Hall bar of 50 μm width was about 0.15 Ω with a relative change of approximately 0.2%, twice as much as the relative change observed in the TbFeCo (0.1%). Furthermore, the reduction of the high MR in the TbSmFeCo in a large field was less obvious than in the TbFeCo.

6.2.3.3 *Initializing Field of Exchange Bias*

This research has proven the initializing procedure to be critical for the EB. Figure 6.8 (a) presents the results of the hysteresis loops at 315 K of the 200 nm TbFeCo film, which were initialized by a set of gradually increasing fields at 365 K. When initialized by a field smaller than 6 kOe, no EB came to surface and the hysteresis loop was symmetric. In this example the EB started forming and finally saturated for the initializing field from 6 kOe to 10 kOe. The EB continued to keep the same value for an initializing field larger than 10 kOe. This observation is consistent with the film's coercivity of 6 kOe at 365 K, and it was fully saturated in 10 kOe at 365 K, as shown in Figure 6.8 (b).

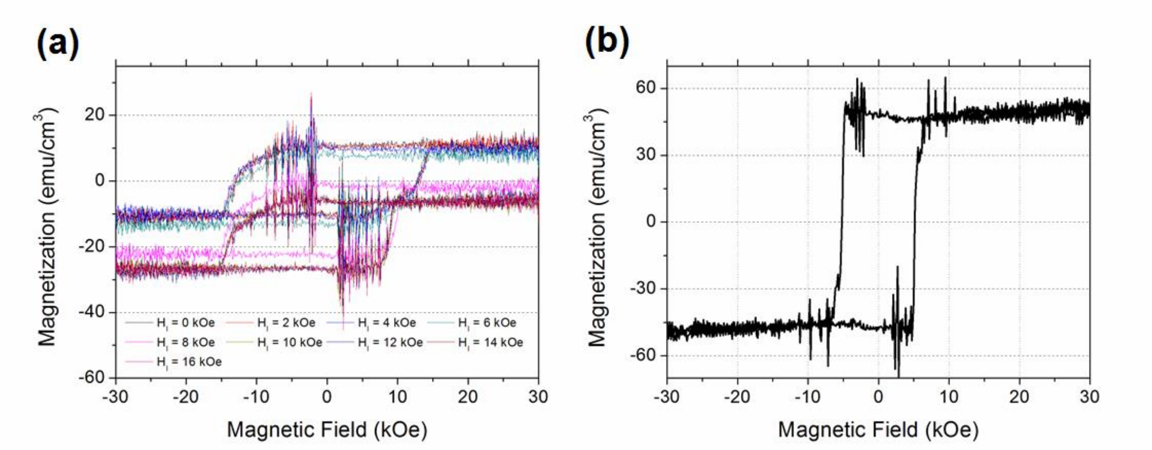

Figure 6.8. Initializing field dependence of EB: (a) Out-of-plane hysteresis loops at 315 K of a 200 nm co-sputtered TbFeCo thin film that were initialized by different magnetic field at 365 K. (b) Out-of-plane hysteresis loop of the same sample at 365 K.

6.2.3.4 *Temperature Dependence of Exchange Bias*

As previously discussed, the EB only existed in the temperature range near the compensation temperature. Moreover, in the present research an obvious temperature dependence of the EB was found within this temperature range as well. Examining the TbSmFeCo film, for example, Figure

6.9 with hysteresis loops measured by VSM, shows that no EB could be observed at 300 K. As the temperature decreased, both positive and negative EB were detected at 275 K. A continuing cooling resulted in a two-step hysteresis loop at 225 K, which implied a possible EB if scanned by a smaller field range, e.g. 20 kOe. For further discussion, the positive minor loop at 225 K had a positive EB, different from that at 275 K. This indicated the compensation temperature of the system was between 225 K and 275 K, where the orientation of the system reversed. In addition, the step position at 225 K actually corresponded to the possible exchange-biased minor loop position. Here the possible EB at 225 K was clearly larger than that at 275 K.

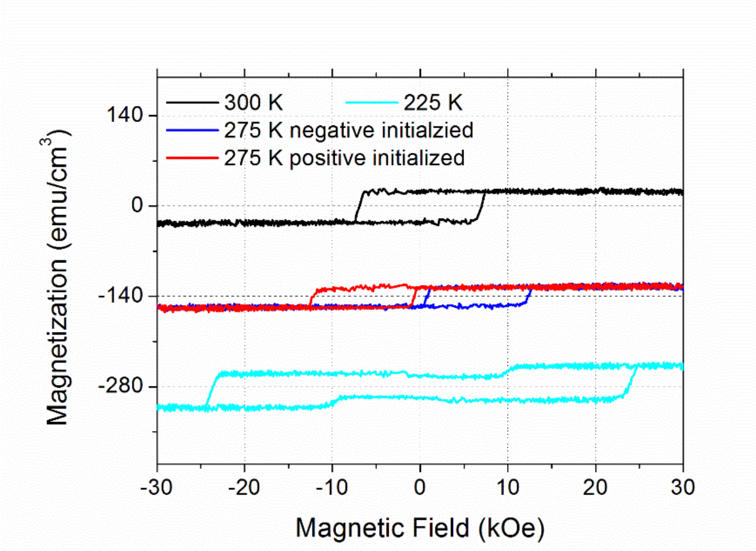

Figure 6.9. Temperature dependence of exchange-biased hysteresis loops of co-sputtered TbSmFeCo thin film measured by VSM.

This temperature dependence was proven by the AHE measurement of the TbSmFeCo Hall bar. As shown in Figure 6.10, the EB started at 275 K, increased gradually as the temperature decreased, and finally disappeared at 100 K. This confirms the above findings from the VSM results that the EB increased as temperatures cooled down. The difference of the AHE and VSM measurements was due to a larger coercivity induced by the Hall bar fabrication.[100]

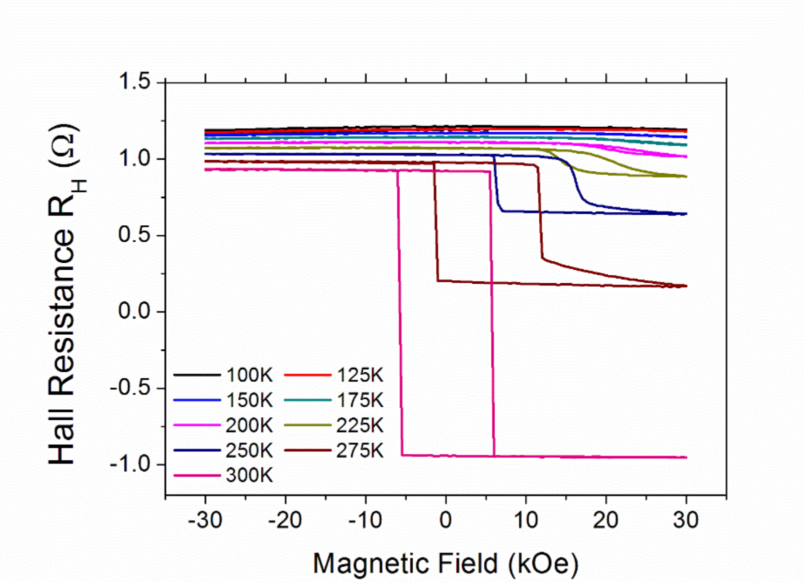

Figure 6.10. Temperature dependence of exchange-biased hysteresis loops of co-sputtered TbSmFeCo thin film measured by AHE.

6.2.4 Two-Phase Model

The EB effect can be interpreted by the presence of two nanoscale magnetic phases. The following will examine the TbFeCo film as an example. Based on the STEM-EDS and APT results, there are two coexisting nanoscale amorphous phases. In the Fe-enriched phase (Phase II) the FeCo moment prevails at room temperature making Phase II behave in a FM manner. Meanwhile, the other phase (Phase I) with higher Tb content provides a near-compensated FI component. The magnetization and anomalous Hall resistance can be expressed in terms of the contributions from the two phases respectively.

$$M = \phi\left(M_{Tb}^{I} + M_{FeCo}^{I}\right) + (1-\phi)\left(M_{Tb}^{II} + M_{FeCo}^{II}\right) \tag{6.1}$$

$$R_H \propto C^{I}\left(R_{Tb}^{I}M_{Tb}^{I} + R_{FeCo}^{I}M_{FeCo}^{I}\right) + C^{II}\left(R_{Tb}^{II}M_{Tb}^{II} + R_{FeCo}^{II}M_{FeCo}^{II}\right) \tag{6.2}$$

Where the superscript I and II denote two nanoscale phases, and ϕ is the volume concentration of Phase I. C^I and C^{II} are positive constants related to ϕ and conductivity tensor of each phase.[118] Additionally, M_{Tb} is opposite to M_{FeCo} due to AFM coupling.

The positive and negative H_E of the EB effect depends on the magnetic orientation of Phase I. Specifically, initialization dependence can be understood by the following discussion. In +30 kOe at 175 K (or 355 K), both M_{FeCo}^{I} and $M_{FeCo}^{II}$are aligned to a negative (or positive) orientation. As the temperature returns to 300 K, the orientation of Phase I persists and becomes fixed because of its large H_C near compensation. In this way, two distinct orientations of Phase I can be initialized, corresponding to the two opposite biased hysteresis loops. Since all temperatures in this study are essentially lower than the Curie temperature, both nanoscale phases are magnetically ordered, making the initializing process different from the zero-field cooling and field cooling in FM/AFM systems.[119] The cooling or heating process shifts the near-compensated Phase I away from compensation and reduces its coercivity. The critical step here is to align the FI phase by directly applying a field larger than the reduced coercivity. Cooling or heating with zero or non-zero field has been verified to offer an identical effect.

In Figure 6.6 (b-c), the magnetic states of Phase I and II are depicted by colored arrows. The left pair indicates the near-compensated Phase I (M_{Tb}^{I} and M_{FeCo}^{I}), and the right indicates the uncompensated Phase II (M_{Tb}^{II} and M_{FeCo}^{II}). In each pair a purple arrow represents M_{FeCo} and an orange arrow represents M_{Tb}. Each biased hysteresis loop contains two magnetic states, i.e. parallel and antiparallel states in terms of the relative orientations of M_{FeCo}^{I} and M_{FeCo}^{II}. The antiparallel state is metastable due to its higher exchange energy than the parallel state. Thus, it requires a larger field to switch from the parallel state to the antiparallel state and a smaller field when switching in the opposite direction, making the hysteresis loop exchange biased. Based on Equation 6.1 and 6.2, the biased loops also shift along the M and R_H axes because of the fixed contribution from Phase

I. Since Phase I is near-compensated, $M_{Tb}^{I} + M_{FeCo}^{I}$ is close to zero. So the M-shift of the magnetic hysteresis loop is very small along M_{FeCo}^{I} above T_{comp}. On the other hand, as discussed above, $C^{I}\left(R_{Tb}^{I}M_{Tb}^{I} + R_{FeCo}^{I}M_{FeCo}^{I}\right)$ always provides a finite contribution, resulting in a determinate R_H-shift opposite to M_{FeCo}^{I}. Interestingly, a positive EB together with an upward M-shift has been reported in the Fe/FeF$_2$ system with an AFM interfacial coupling.[120] However, the current study presented a positive EB corresponded to a tiny downward M-shift as well as an upward R_H-shift. This fact suggests that the overall interfacial coupling at 300 K is FM, which is consistent with the larger FeCo contribution in both phases.

In addition, the shape of the biased loops, especially of the biased AHE loops, is asymmetric. The metastable antiparallel state gradually evolves (or "rotates") to a stable parallel state on the other loop. This transition indicates a big major loop with a greater coercive field enveloping both biased loops and connecting the two isolated branches. It should be noted that the observed exchange bias is a minor loop effect. The major loop would be symmetric if sufficiently large fields were applied to switch Phase I. Moreover, the temperature has a significant effect on the EB. At a high temperature, magnetic ordering mainly comes from the FeCo spins making both of the phases FM dominated. On the other hand, at a low temperature, the two phases magnetically merge into a rigid FI phase because of the large Tb atomic moment and single-ion anisotropy. Thus, the EB vanishes at both low and high temperatures.

The model of two nanoscale phases implies the existence of the bistable MR states. The magnetic states are depicted along with the biased MR loops in Figure 6.6 (c) and Figure 6.7 (c). Obviously, the MR value mainly depends on the relative orientation of the two nanoscale phases. The parallel states have lower MR than the antiparallel states similar to the tunnel MR in magnetic tunnel junctions.[30] A more complete schematic discussion can be found in Figure 6.11.

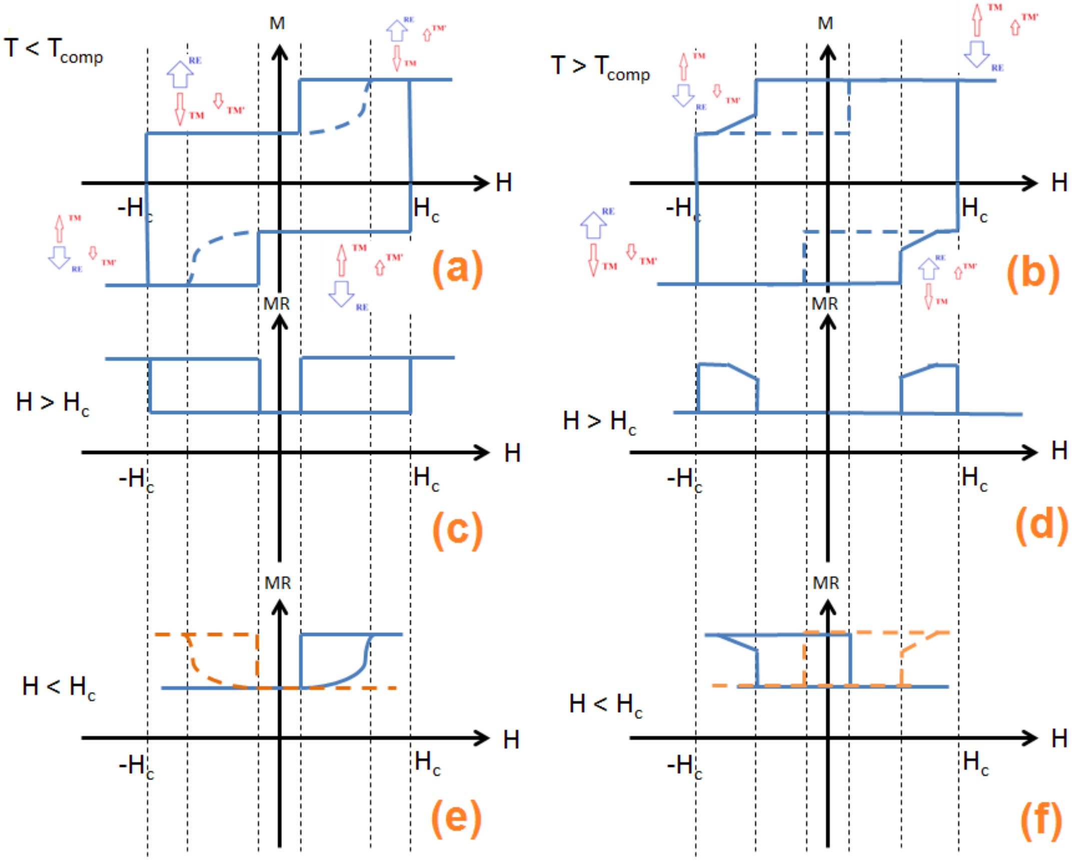

Figure 6.11. Schematic discussion of ferrimagnetic exchange bias based on the two-phase model.

Finally, according to the two-phase model, a pair of MR states on each exchange-biased MR loop can be obtained as shown in Figure 6.11 (f). Moreover, bistable MR states could be switched by external magnetic field impulses, as shown in Figure 6.12 (a-b). The stability of the high MR state, i.e. the antiparallel state, has been verified by a measurement over a specific time period, as is shown in Figure 6.12 (c).

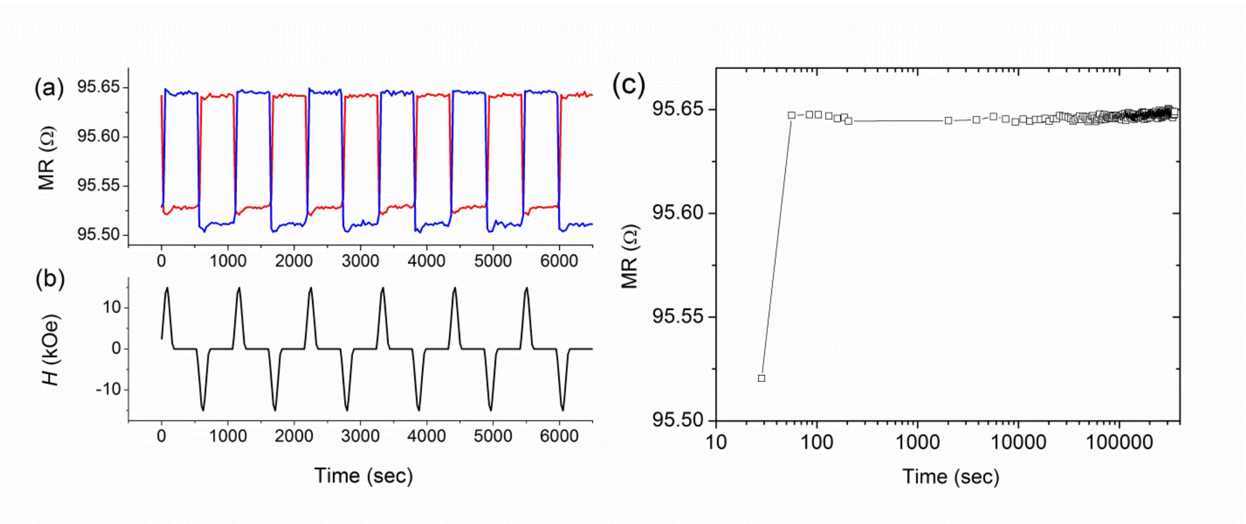

Figure 6.12. The MR switching and stability of the amorphous $Tb_{26}Fe_{64}Co_{10}$ 50 µm Hall bar. a) The MR switching driven by magnetic field impulses at 300 K. b) The stability of the high MR state under 300 K and zero field. The MR was switching from low to high at the beginning. Published by Li et al.[115]

6.3 Numerical Modeling of Exchange Bias in Ferrimagnetic System

In order to have a deeper understanding of the EB in the amorphous Tb(Sm)FeCo thin films, a numerical modeling study was performed using the magnetic modeling package (MMP). A ferrimagnetic core-and-matrix geometry was investigated atomistically and provided reasonable exchange-biased hysteresis loops. Temperature dependence of the EB was predicted by this simple model, which agreed with the experimental results. Finally, a micromagnetic model was proposed for a phase-separated system.

6.3.1 Exchange Bias in Ferrimagnetic Core-and-Matrix

A ferrimagnetic core-and-matrix geometry was generated atomistically as presented in Figure 6.13. The pseudo amorphous structure was built on a 36 × 36 × 36 FCC lattice with a 5.2 nm diameter core of $Tb_{18}Fe_{82}$ in a matrix of $Tb_{26}Fe_{74}$, and the interfacial Fe atoms were colored differently.

Periodic boundary conditions were applied in this model, and the same simulation parameters were adopted as listed in Table 5.3.

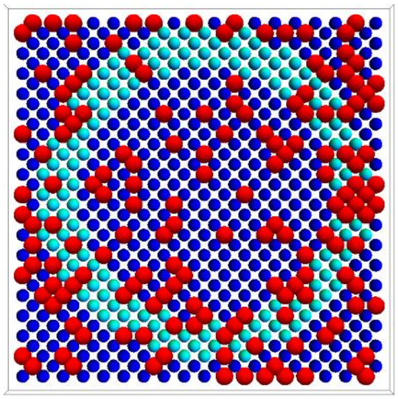

Figure 6.13. Center-cross-sectional plane of an atomistic amorphous core-and-matrix geometry. Tb atoms are depicted by red spheres, and Fe atoms are represented by blue (non-interfacial) and cyan (interfacial) spheres.

The magnetization vs. temperature relation was studied first by the parallel tempering algorithm. As shown in Figure 6.14, the overall compensation temperature was about 246.4 K. No compensation was found for the core of $Tb_{18}Fe_{82}$, while the matrix of $Tb_{26}Fe_{74}$ was compensated at 310.7 K.

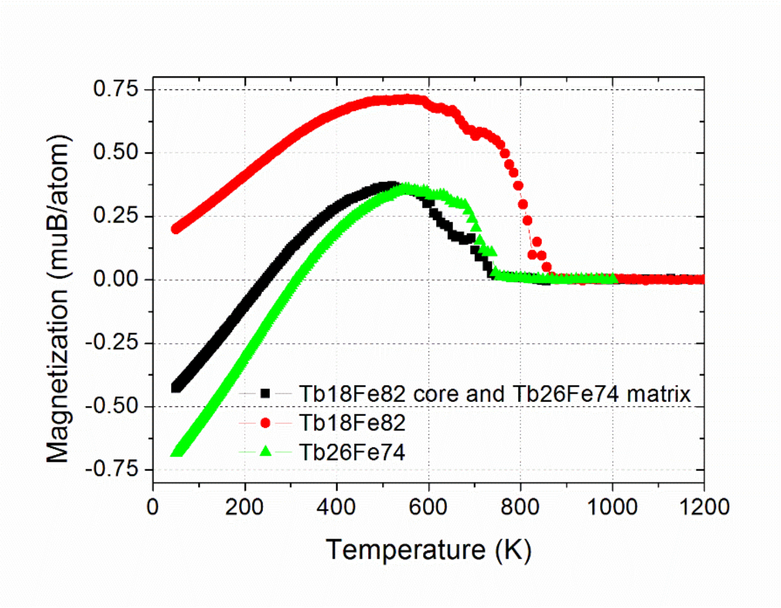

Figure 6.14. Magnetization vs. temperature curves were simulated for uniform alloys and core-and-matrix structure.

Hysteresis loops could be simulated by the stochastic LLG algorithm at 310.7 K. As shown in Figure 6.15, the hysteresis loop was symmetric with no EB. This symmetric loop indicated that both the core and matrix reversed together due to the strong coupling through their interface.

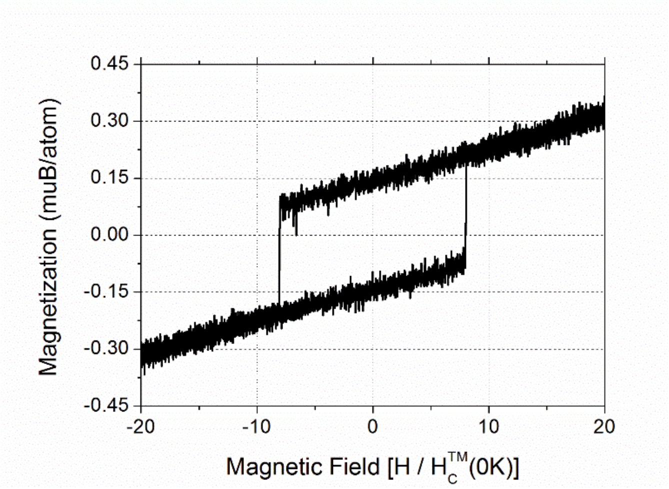

Figure 6.15. Hysteresis loop of plain core-and-matrix structure was simulated at 310 K by the stochastic LLG.

In order to obtain an exchange-biased loop as observed in the experiments, the interfacial coupling had to be weakened. For this study, the interfacial Fe-Fe coupling was reduced to 2.25×10^{-21} J/link. Additionally, 35% of Fe-Fe coupling were treated as antiferromagnetic with a coupling strength of -2.20×10^{-21} J/link. The applied exchange reduction and antiferromagnetic coupling was based on the atomic distance variation of the RKKY interaction between Fe-Fe nearest neighbors.[121] The revealed amorphous phase-separation, by HRTEM and APT experimentally, implied a significant heterogeneity due to the co-sputtering deposition at an Ar pressure of 7 mTorr.

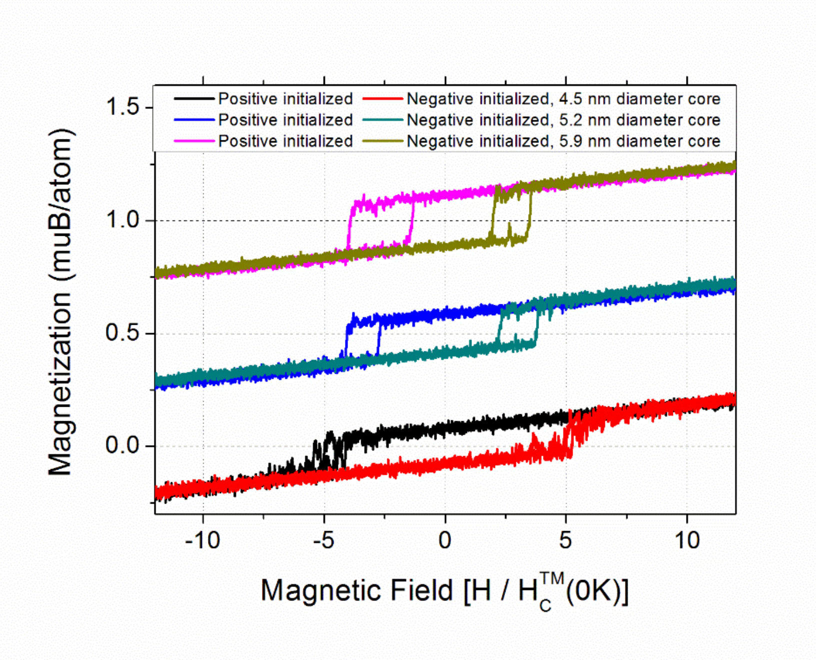

Figure 6.16. Exchange-biased hysteresis loops were simulated with an interfacial exchange reduction in different sizes of core-and-matrix structures at 310.7 K.

With the treatment of the interfacial Fe-Fe coupling, this simple atomistic model was able to generate exchange-biased hysteresis at 310.7 K, as demonstrated in Figure 6.16. Three different size cores were investigated in this study. The EB tended to be smaller for larger cores because of a reduced surface-to-volume ratio. This fact confirmed the interfacial feature of the exchange anisotropy.[37] Additionally, the hysteresis loop had a smoother shape with more atoms inside the core.

For the temperature dependence study, the 5.2 nm diameter core was used as an example. The same model was simulated at different temperatures ranging from 200 K to 450 K. As shown in Figure 6.17, the EB only existed at temperature higher than 275 K, and increased as the temperature cooled down. However, if a smaller field scanning range was considered, e.g. 10, the step shape loop at 262.5 K could also provide exchange-biased minor loops. This confirmed the fact that the EB actually exhibited a minor loop effect, which was consistent with the experimental observation. This loop had a similar shape as the schematic curve of the two-phase model in Figure 6.11 (a). From 262.5 K to 225 K, the hysteresis loop evolved from an obvious step shape to a standard square shape. During this process, the coercivity of the matrix decreased as it moves away from its compensation, however, the EB continued increasing as is indicated by a green dashed line. The EB finally disappeared when it was larger than the matrix coercivity, and both the core and matrix reversed together.

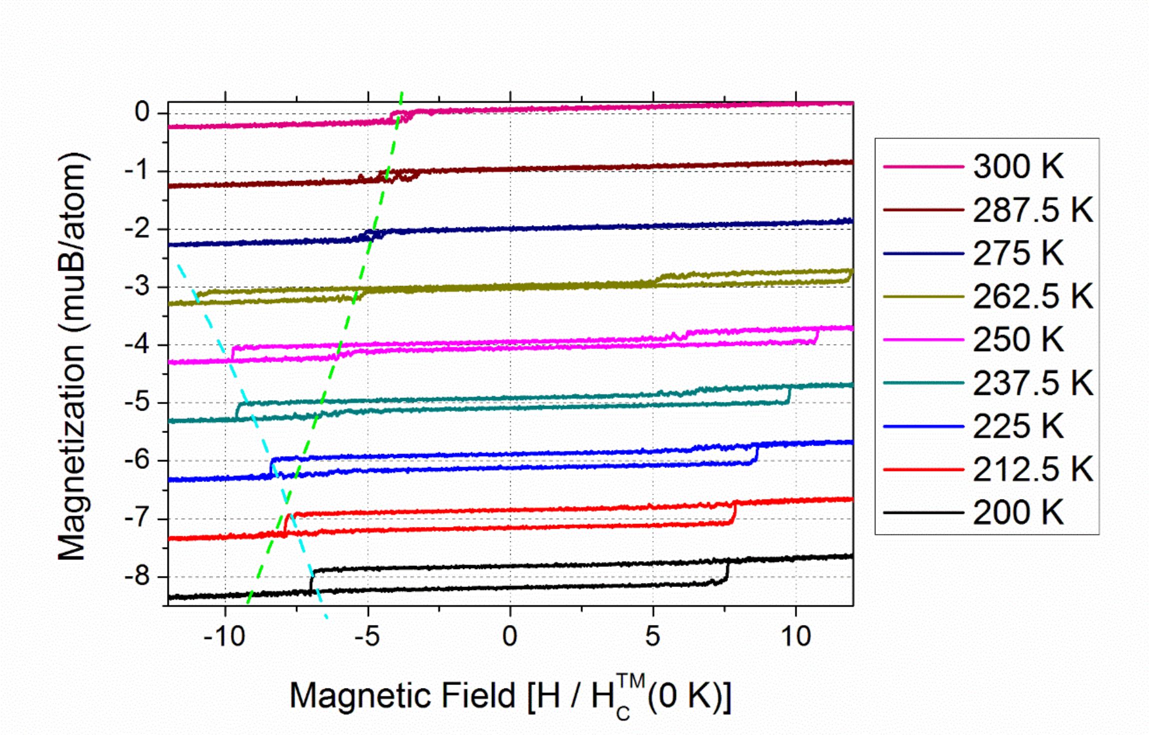

Figure 6.17. Temperature dependence of EB in ferrimagnetic core-and-matrix structure. The green dash line indicates the trend of EB. The cyan dash line indicates the coercivity variation of the matrix.

Figure 6.18 presents a series of hysteresis loops at temperatures higher than 300 K. Similar to Figure 6.17, the EB was seen at for temperatures below 350 K, and the its value decreased as the temperature ramped up. Moreover, two-step curves appeared in a way similar to the typical shape of the two-phase model above compensation temperature, as depicted in Figure 6.11 (b). The coercivity reduced as the temperature increased above the matrix compensation temperature, e.g. 310.7 K. As shown by the green and cyan dashed curves, the two steps would finally merge into a regular square shape. It should be noted that because of the randomness at higher temperatures, both the coercivity and the EB were not always symmetrical. This also implies a possible underestimation of the temperature response: the hysteresis loop of a real system will offer an average over the ensemble of all possible curves, which tends to consequently smear out the exchange-biased two steps.

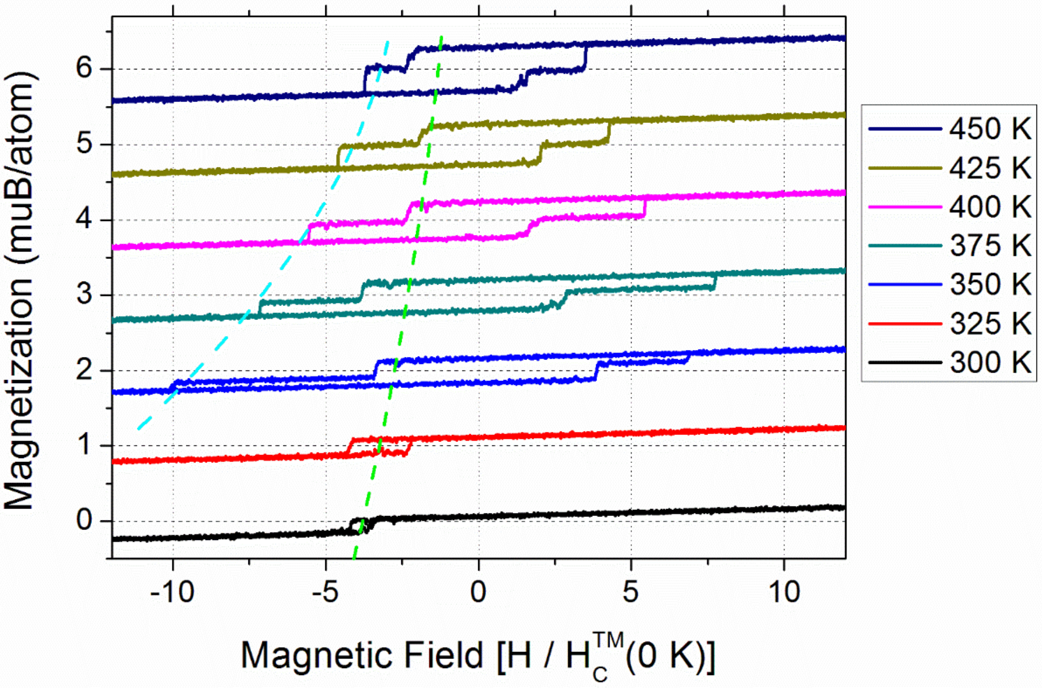

Figure 6.18. Temperature dependence [continued] of EB in ferrimagnetic core-and-matrix structure. The green dash line indicates the trend of EB. The cyan dash line indicates the coercivity variation of the matrix.

6.3.2 Exchange Bias in Phase-Separated Ferrimagnetic System

As shown in the previous section, the EB could be obtained in the core-and-matrix geometry by atomistic modeling. However, in order to compare to the experimental nanoscale phase-separated Tb(Sm)FeCo films directly, a larger scale simulation, e.g. in tens of nanometers, is still in need. Micromagnetism, as introduced in Chapter 4, is a feasible approach for this purpose. In this section, a micromagnetic model for ferrimagnetic materials will be formulated starting from the atomistic Heisenberg model.

A typical Hamiltonian of exchange interaction is given by:

$$\begin{aligned}\mathcal{H}_{ex} = -\frac{1}{2}\sum_{\langle Tb_i,Tb_j\rangle} J_{Tb-Tb}\boldsymbol{S}_{Tb_i}\cdot\boldsymbol{S}_{Tb_j} - \frac{1}{2}\sum_{\langle Fe_i,Fe_j\rangle} J_{Fe-Fe}\boldsymbol{S}_{Fe_i}\cdot\boldsymbol{S}_{Fe_j} \\ - \sum_{\langle Tb_i,Fe_j\rangle} J_{Tb-Fe}\boldsymbol{S}_{Tb_i}\cdot\boldsymbol{S}_{Fe_j}\end{aligned} \tag{6.3}$$

Assuming the exchange constants are uniform, the first term can thus be rearranged as:

$$\begin{aligned}\mathcal{H}_{Tb-Tb} &= -\frac{1}{2}J_{Tb-Tb}\sum_{\langle Tb_i,Tb_j\rangle}\left(1-\frac{1}{2}\left(\boldsymbol{S}_{Tb_i}-\boldsymbol{S}_{Tb_j}\right)^2\right) \\ &= const. + \frac{1}{4}J_{Tb-Tb}\sum_{\langle Tb_i,Tb_j\rangle}\left(\boldsymbol{S}_{Tb_i}-\boldsymbol{S}_{Tb_j}\right)^2\end{aligned} \tag{6.4}$$

It can be further simplified, given that the system is continuous and the atoms are located in a symmetric way:

$$\begin{aligned}\mathcal{H}_{Tb-Tb} &\approx \frac{1}{4}J_{Tb-Tb}\sum_{\langle Tb_i,Tb_j\rangle}\left(\boldsymbol{r}_{ij}\cdot\nabla\boldsymbol{S}_{Tb}(\boldsymbol{x}_i)\right)^2 \\ &= \frac{1}{2}Ca^2 J_{Tb-Tb} z_{Tb-Tb}\sum_{Tb_i}\left(\nabla\boldsymbol{S}_{Tb_i}\right)^2\end{aligned} \tag{6.5}$$

Table 6.1. Lattice-dependent constant *C*.

	Neighbor rank	Coordination z	Constant C
Simple cubic	1st	6	1/6
	1st, 2nd	18	5/18
Face-centered cubic	1st	12	1/12
	1st, 2nd	18	1/9
	1st, 2nd, 3rd	32	4/21

Where C is a lattice-dependent constant as shown in Table 6.1, a is lattice constant, and z_{Tb-Tb} is Tb-Tb coordination number. A ferromagnetic exchange stiffness constant can then be defined as:

$$A_{Tb-Tb} \equiv \frac{1}{2} C a^2 J_{Tb-Tb} z_{Tb-Tb} c_{Tb} / V_{atom} \tag{6.6}$$

Where c_{Tb} is Tb atomic concentration, and V_{atom} is the average atomic volume. Thus, the ferromagnetic term can be rearranged into the following continuous form:

$$\mathcal{H}_{Tb-Tb} = A_{Tb-Tb} \sum_{Tb_i} \frac{\left(\nabla \boldsymbol{m}_{Tb_i}\right)^2 V_{atom}}{c_{Tb}} = A_{Tb-Tb} \int (\nabla \boldsymbol{m}_{Tb})^2 d^3x \tag{6.7}$$

Similarly, the Fe-Fe ferromagnetic exchange term is given by:

$$A_{Fe-Fe} \equiv \frac{1}{2} C a^2 J_{Fe-Fe} z_{Fe-Fe} c_{Fe} / V_{atom} \tag{6.8}$$

$$\mathcal{H}_{Fe-Fe} = A_{Fe-Fe} \sum_{Fe_i} \frac{\left(\nabla \boldsymbol{m}_{Fe_i}\right)^2 V_{atom}}{c_{Fe}} = A_{Fe-Fe} \int (\nabla \boldsymbol{m}_{Fe})^2 d^3x \tag{6.9}$$

For the antiferromagnetic exchange term, the following constants are defined:

$$A_{Tb-Fe} \equiv C a^2 J_{Tb-Fe} z_{Tb-Fe} c_{Tb} / V_{atom} \equiv A_{Fe-Tb} \tag{6.10}$$

$$B_{Tb-Fe} \equiv J_{Tb-Fe} z_{Tb-Fe} c_{Tb} / V_{atom} \equiv B_{Fe-Tb} \tag{6.11}$$

Therefore,

$$\begin{aligned}\mathcal{H}_{Tb-Fe} &= -B_{Tb-Fe}\sum_{Tb_i}\frac{\boldsymbol{S}_{Tb_i}\cdot\boldsymbol{S}_{Fe_i}V_{atom}}{c_{Tb}} - A_{Tb-Fe}\sum_{Tb_i}\frac{\boldsymbol{S}_{Tb_i}\cdot\nabla^2\boldsymbol{S}_{Fe_i}V_{atom}}{c_{Tb}}\\ &\quad + A_{Tb-Fe}\sum_{Tb_i}\frac{\nabla\cdot\left(\boldsymbol{S}_{Fe}\cdot\nabla\boldsymbol{S}_{Fe_i}\right)V_{atom}}{c_{Tb}}\\ &= -B_{Tb-Fe}\int\boldsymbol{S}_{Tb}\cdot\boldsymbol{S}_{Fe}d^3x - A_{Tb-Fe}\int\boldsymbol{S}_{Tb}\cdot\nabla^2\boldsymbol{S}_{Fe}d^3x\\ &\quad + A_{Tb-Fe}\oint\boldsymbol{S}_{Fe}\cdot\nabla\boldsymbol{S}_{Fe}\cdot\boldsymbol{n}dS\end{aligned}\tag{6.12}$$

Since the last term is integrated only on the boundary, it can be dropped when expressing energy density:

$$\begin{aligned}\mathcal{E}_{ex} &= A_{Fe-Fe}(\nabla\boldsymbol{S}_{Fe})^2 + A_{Tb-Tb}(\nabla\boldsymbol{S}_{Tb})^2\\ &\quad - A_{Tb-Fe}\boldsymbol{S}_{Tb}\nabla^2\boldsymbol{S}_{Fe} - B_{Tb-Fe}(\boldsymbol{S}_{Tb}\cdot\boldsymbol{S}_{Fe})\end{aligned}\tag{6.13}$$

Finally, the effective field due to the exchange interaction is given by:

$$\begin{aligned}\boldsymbol{H}_{ex,Tb} &= \frac{2}{\mu_0 M_{s,Tb}}A_{Tb-Tb}\nabla^2\boldsymbol{S}_{Tb} + \frac{1}{\mu_0 M_{s,Tb}}A_{Tb-Fe}\nabla^2\boldsymbol{S}_{Fe}\\ &\quad + \frac{1}{\mu_0 M_{s,Tb}}B_{Fe-Tb}\boldsymbol{S}_{Fe}\end{aligned}\tag{6.14}$$

$$\begin{aligned}\boldsymbol{H}_{ex,Fe} &= \frac{2}{\mu_0 M_{s,Fe}}A_{Fe-Fe}\nabla^2\boldsymbol{S}_{Fe} + \frac{1}{\mu_0 M_{s,Fe}}A_{Fe-Tb}\nabla^2\boldsymbol{S}_{Tb}\\ &\quad + \frac{1}{\mu_0 M_{s,Fe}}B_{Tb-Fe}\boldsymbol{S}_{Tb}\end{aligned}\tag{6.15}$$

Where $M_{s,Tb} \equiv \frac{\mu_{Tb}\mu_B c_{Tb}}{V_{atom}}$ and $M_{s,Fe} \equiv \frac{\mu_{Fe}\mu_B c_{Fe}}{V_{atom}}$. Moreover, the effective field due to uniaxial magnetic anisotropy can be formulated as:

$$\boldsymbol{H}_{an,Tb} = 2\,\frac{K_{Tb}(\boldsymbol{S}_{Tb}\cdot\boldsymbol{n})\boldsymbol{n}}{\mu_0 M_{s,Tb}}\tag{6.16}$$

$$\boldsymbol{H}_{an,Fe} = 2\,\frac{K_{Fe}(\boldsymbol{S}_{Fe}\cdot\boldsymbol{n})\boldsymbol{n}}{\mu_0 M_{s,Fe}} \tag{6.17}$$

Where:

$$K_{Tb} \equiv \frac{D_{Tb}c_{Tb}}{V_{atom}} \tag{6.18}$$

$$K_{Fe} \equiv \frac{D_{Fe}c_{Fe}}{V_{atom}} \tag{6.19}$$

Joining Equation 6.14, 6.15, 6.16 and 6.17, together with the demagnetizing and external field, provides the necessary micromagnetic effective field. Integrated by the stochastic LLG Equation 4.52, the phase-separated structure of tens of nanometers can be numerically solved in the frame of the micromagnetism. A series of simulations have been completed by Chung T. Ma, a researcher in our group. These simulations were performed on the platform of OOMMF from NIST, and produced qualitatively consistent results, as shown in Figure 6.19.[122]

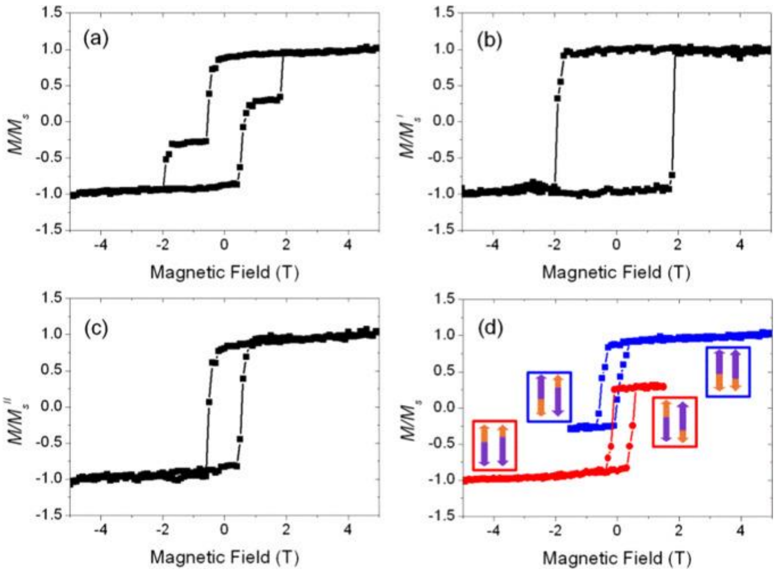

Figure 6.19. Simulated hysteresis loops of two-phase model. (a) Major loop of TbFeCo above T_{comp}, external field scans from 5 T to -5T to 5T. (b–c) Contribution to the major loop from Phase I (b) and Phase II (c) above T_{comp}. (d)

Exchange-biased minor loops of TbFeCo above T_{comp}. External field scans from 5 T to -1.1 T to 5 T (blue square), and from -5T to 1.1 T to 5 T (red circle). The insert shows an example of magnetic configuration. The left pair corresponds to the near-compensated Phase I, and the right for the uncompensated Phase II. Purple arrow represents the moments of FeCo, and orange arrow represents the moments of Tb. The blue box indicates the magnetic configuration of the sample initialized under 355 K and 3 T (blue square), and the red box indicates the magnetic configuration of the sample initialized under 175 K and 3 T (red circle). From Ma et al.[122]

6.4 Concluding Remarks

In summary, this work provides experimental evidence of the EB in the co-sputtered amorphous Tb(Sm)FeCo thin films. The EB is closely related to the two growth-induced nanoscale phases distributed throughout the film, which were observed using STEM-EDS and APT. This exchange-biased thin film has many appealing properties such as the large PMA and room-temperature capability. Moreover, the amorphous thin film requires no epitaxial growth and specific substrates. The bistable MR states associated with the EB were proven to be stable at room temperature and switchable by sweeping the magnetic field.

A numerical study of the EB in the ferrimagnetic core-and-matrix geometry has been performed atomistically by the MMP. This simple model predicted the temperature response of the ferrimagnetic EB, which agreed with the empirical experimental results. Larger scale numerical models for the experimental nanoscale phase-separated system have been proposed in the micromagnetic frame. The micromagnetic formulation has led to preliminary results that were qualitatively consistent to the experimental observations, thus providing numerical supports for the EB when induced by nanoscale two-phase separation.

CHAPTER 7 MODELING OF ULTRAFAST MAGNETIZATION DYNAMICS OF RE-TM SYSTEM

7.1 Introduction

Ultrafast magnetization dynamics have been a topic of examination over the past decades. The RE-TM system is particularly interesting due to the discovery of all-optical switching (AOS).[12,14] Moreover, Skyrmion state has recently been reported in GdFe.[18] These findings make RE-TM thin films promising for future high-speed, low-current spintronic devices. This chapter will present a modeling study of ultrafast dynamics of the RE-TM thin film. Section 7.2 will introduce a phenomenological model for the ultrashort laser heating of metal by a femtosecond laser. Section 7.3 will uncover the discovery of the ultrafast dynamics of amorphous GdFe alloys, especially the reversal probability in terms of laser fluence, atomic concentration, and Gd-Fe pair ratio. Finally, a series of simulations will be presented for Gd/Fe multilayers in Section 7.4.

7.2 Two-Temperature Model

7.2.1 Phenomenological Two-Temperature Model

Rapid advancement of femtosecond lasers has been driving new research in many areas of science and technology ranging from femtosecond laser micromachining[123] to ultrafast magnetization reversal.[56,67] Theoretically, the interaction of ultrashort-pulsed lasers with matter can be described by a phenomenological two-temperature (2T) model, which has been employed for examining ultrafast thermal responses of electrons and phonons with different laser pulse lengths and the types of materials. The phenomenological 2T model has especially been adopted as an approximated treatment of spin-orbit, spin-lattice and electron-lattice interactions in the ultrafast optical control of magnetism.[66,94] The dual-hyperbolic phenomenological 2T model, proposed by Chen et al.[124] for ultrafast laser-material interactions, is given by:

$$C_e \frac{\partial T_e}{\partial t} = -\nabla \cdot \boldsymbol{Q}_e - G(T_e - T_l) + S(\boldsymbol{x}, t) \tag{7.1}$$

$$\tau_e \frac{\partial \boldsymbol{Q}_e}{\partial t} + \boldsymbol{Q}_e = -K_e \nabla T_e \tag{7.2}$$

$$C_l \frac{\partial T_l}{\partial t} = -\nabla \cdot \boldsymbol{Q}_l + G(T_e - T_l) \tag{7.3}$$

$$\tau_l \frac{\partial \boldsymbol{Q}_l}{\partial t} + \boldsymbol{Q}_l = -K_l \nabla T_l \tag{7.4}$$

The non-equilibrium system is depicted by two temperatures: electron temperature T_e, and lattice (or phonon) temperature T_l. Equation 7.1 and 7.3 stand for the energy conservation of electrons and phonons respectively, where C is the heat capacity and $\boldsymbol{Q}$ is the heat flux. A constant G represents the electron-phonon coupling factor, and S is the volumetric laser heat source. Additionally, a time-dependent heat flux of both electron and lattice is related to temperature in Equation 7.2 and 7.4, where K is the thermal conductivity and τ is the relaxation time. For most metals, heat conduction of the lattice is much smaller than that of electrons. Therefore, Equation 7.3 and 7.4 can be combined by dropping the lattice flux term $\boldsymbol{Q}_l$. Moreover, when laser pulse length is much longer than τ_e, which is usually tens of femtoseconds, Equation 7.1 and 7.2 can be further simplified to a parabolic partial differential equation.

7.2.2 Semi-classical Two-Temperature Model

Even though the phenomenological 2T model has been widely employed in past studies, a semi-classical 2T model was proposed by Chen et al.[125] for situations when heat-induced electric field and carrier gradient is extensive and non-equilibrium transport conditions have to be considered. This is particularly true for localized ultrashort-pulse laser heating due to the well-known fact that a tremendously sharp gradient of the electron temperature is present in a small geometry volume. The semi-classical 2T model can be established with the help of transport equations with the Boltzmann approximation. Detailed derivation can be found in APPENDIX H. The semi-classical 2T model contains the same lattice energy conservation equation, i.e. Equation 7.3 and two constitutive equations for heat fluxes in the electrons and phonons, i.e. Equation 7.2 and 7.4. This model also contains two additional equations for electron momentum and energy conservation:

$$C_e\left(\frac{\partial T_e}{\partial t}+\boldsymbol{v}\cdot\nabla_r T_e+\frac{2}{3}T_e\nabla_r\cdot\boldsymbol{v}\right)+\nabla_r\cdot\boldsymbol{Q}_e=-G(T_e-T_l)+S(\boldsymbol{r},t) \tag{7.5}$$

$$m\frac{\partial\boldsymbol{v}}{\partial t}+m\boldsymbol{v}\cdot\nabla_r\boldsymbol{v}+\left[k_B\left(1+\frac{T_e}{C_e}\frac{\partial C_e}{\partial T_e}\right)-e\beta\right]\nabla T_e=-\frac{eT_e\boldsymbol{v}}{\mu_0 T_l} \tag{7.6}$$

These equations determine the temporal and special profile of both electron temperature T_e and mean velocity $\boldsymbol{v}$. In these equations, e and m are the charge and mass of electrons, and k_B is the Boltzmann constant. The parameter μ_0 is 4.8×10^{-3} $\mathrm{m^2s^{-1}V^{-1}}$. The parameter β is defined as $\beta\equiv-1.42\times10^{-4}(T_e/T_F)$ V/K for free electrons where T_F is fermi temperature. Figure 7.1 plots a temporal profile of electron temperature at the front surface of an 80 nm gold film irradiated by a 28 J/m^2, 800 nm, 150 fs laser pulse.[125] This demonstrates agreement between the semi-classical and the phenomenological 2T models for a low-laser fluence.

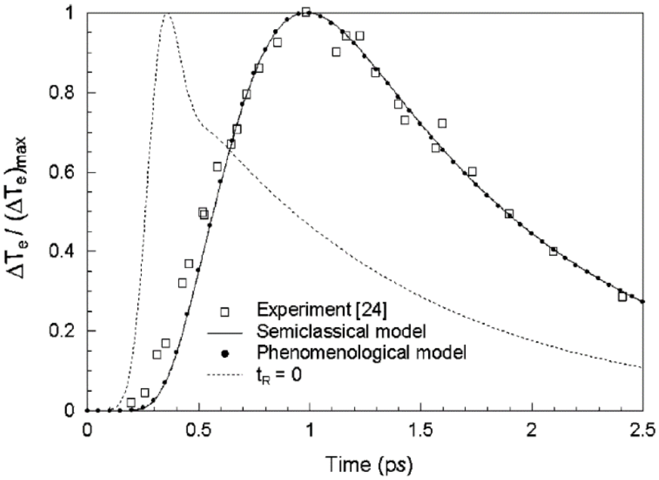

Figure 7.1. Comparison of the change in electron temperature at the front surface of an 80 nm gold film irradiated by a 2.8 mJ/cm^2, 800 nm, 150 fs laser pulse. From Chen et al.[125]

7.2.3 Two-Temperature Model for Ultrafast Magnetization Dynamics

A magnetic alloy system actually contains three interacting components: spins, electrons and phonons, as shown in Figure 7.2.[56] Similarly, a three-temperature (3T) model has been suggested by Agranat et al.[126] The 3T model consists of three reservoirs, namely, spins, electrons, and phonons and interactions between them exhibit different strength and origins. Particularly, the spin system can interact with the other two reservoirs by spin-lattice interaction, spin-orbit coupling, Stoner excitation, inelastic electron-spin-wave scattering, and spin-flip scattering. However, the mechanisms responsible for ultrafast dynamics, e.g. ultrafast demagnetization, remain a subject of active debates. In this study, the complex 3T model is simplified into a 2T model by the assumption that spins and electrons are strongly coupled together, and equilibrate within a very short time, e.g. 20 fs, which corresponds to a spin-orbit coupling of 50 meV.

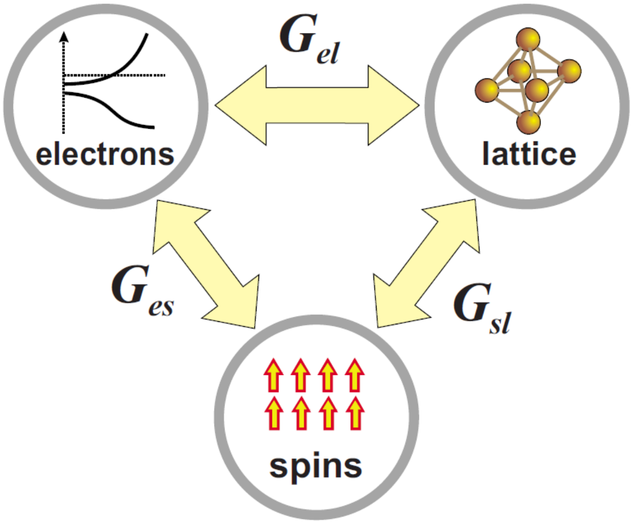

Figure 7.2. Interacting reservoirs: electrons, spins, and lattice, from Kirilyuk et al.[56]

Since issues in the present research are only related to low fluence lasers, the simple phenomenological 2T model serves well for this purpose. First of all, since only a small lateral dimension, i.e. usually tens of nanometers, is investigated atomistically compared to a common laser spot size as 5 μm, the original 3D equations are thus simplified into a set of 1D equations:

$$C_e \frac{\partial T_e}{\partial t} = -\frac{\partial Q_e}{\partial x} - G(T_e - T_l) + S(x,t) \tag{7.7}$$

$$\tau_e \frac{\partial Q_e}{\partial t} + Q_e = -K_e \frac{\partial T_e}{\partial x} \tag{7.8}$$

$$C_l \frac{\partial T_l}{\partial t} = -\frac{\partial Q_l}{\partial x} + G(T_e - T_l) \tag{7.9}$$

$$\tau_l \frac{\partial Q_l}{\partial t} + Q_l = -K_l \frac{\partial T_l}{\partial x} \tag{7.10}$$

These partial differential equations can be solved by the finite difference equations. Given time grid Δt and depth grid h, temperature and heat flux can be discretized as $T_i^f \equiv T(ih, f\Delta t), i =$

$0, 2, \dots, N$and $Q_j^f \equiv Q(jh, f\Delta t), j = 1, 3, \dots, N-1$. Therefore, the discretized equations can be written as:

$$C_{i,e}^{f-1}\frac{T_{i,e}^{f}-T_{i,e}^{f-1}}{\Delta t}=-\frac{Q_{i+1,e}^{f}-Q_{i-1,e}^{f}}{2h}-G_i^{f-1}\left(T_{i,e}^{f-1}-T_{i,l}^{f-1}\right)+S_i^{f-1} \tag{7.11}$$

$$T_{j,e}^{f-1}\frac{Q_{j,e}^{f}-Q_{j,e}^{f-1}}{\Delta t}+Q_{j,e}^{f-1}=-K_{j,e}^{f-1}\frac{T_{j+1,e}^{f-1}-T_{j-1,e}^{f-1}}{2h} \tag{7.12}$$

$$C_{i,l}^{f-1}\frac{T_{i,l}^{f}-T_{i,l}^{f-1}}{\Delta t}=-\frac{Q_{i+1,l}^{f}-Q_{i-1,l}^{f}}{2h}+G_i^{f-1}\left(T_{i,e}^{f-1}-T_{i,l}^{f-1}\right) \tag{7.13}$$

$$T_{j,l}^{f-1}\frac{Q_{j,l}^{f}-Q_{j,l}^{f-1}}{\Delta t}+Q_{j,l}^{f-1}=-K_{j,l}^{f-1}\frac{T_{j+1,l}^{f-1}-T_{j-1,l}^{f-1}}{2h} \tag{7.14}$$

These equations can be rearranged to a set of updating equations as follows:

$$Q_{j,e}^{f}=\left(1-\frac{\Delta t}{\tau_{j,e}^{f-1}}\right)Q_{j,e}^{f-1}-\frac{\Delta t}{\tau_{j,e}^{f-1}}\frac{K_{j,e}^{f-1}}{2h}\left(T_{j+1,e}^{f-1}-T_{j-1,e}^{f-1}\right) \tag{7.15}$$

$$Q_{j,l}^{f}=\left(1-\frac{\Delta t}{\tau_{j,l}^{f-1}}\right)Q_{j,l}^{f-1}-\frac{\Delta t}{\tau_{j,l}^{f-1}}\frac{K_{j,l}^{f-1}}{2h}\left(T_{j+1,l}^{f-1}-T_{j-1,l}^{f-1}\right) \tag{7.16}$$

$$\begin{aligned}T_{i,e}^{f}=T_{i,e}^{f-1}-\frac{\Delta t}{C_{i,e}^{f-1}}\frac{1}{2h}\left(Q_{i+1,e}^{f}-Q_{i-1,e}^{f}\right)-\frac{\Delta t}{C_{i,e}^{f-1}}G_i^{f-1}\left(T_{i,e}^{f-1}-T_{i,l}^{f-1}\right)\\+\frac{\Delta t}{C_{i,e}^{f-1}}S_i^{f-1}\end{aligned} \tag{7.17}$$

$$T_{i,l}^{f}=T_{i,l}^{f-1}-\frac{\Delta t}{C_{i,l}^{f-1}}\frac{1}{2h}\left(Q_{i+1,l}^{f}-Q_{i-1,l}^{f}\right)+\frac{\Delta t}{C_{i,l}^{f-1}}G_i^{f-1}\left(T_{i,e}^{f-1}-T_{i,l}^{f-1}\right) \tag{7.18}$$

Where the thermal conductivity and relaxation time are defined as:

$$K_{j,e}^{f}\equiv\frac{1}{2}\left(K_{j-1,e}^{f}+K_{j+1,e}^{f}\right) \tag{7.19}$$

$$K_{j,l}^{f} \equiv \frac{1}{2}\left(K_{j-1,l}^{f} + K_{j+1,l}^{f}\right) \tag{7.20}$$

$$\tau_{j,e}^{f} \equiv \frac{1}{2}\left(\tau_{j-1,e}^{f} + \tau_{j+1,e}^{f}\right) \tag{7.21}$$

$$\tau_{j,l}^{f} \equiv \frac{1}{2}\left(\tau_{j-1,l}^{f} + \tau_{j+1,l}^{f}\right) \tag{7.22}$$

For this study, the heat capacity of electrons is estimated by $C_e = \gamma T_e$, where γ is 7.0×10^2 J m^{-3} K^{-2}.[58] The thermal conductivity of electrons in the RE-TM alloy has been reported as $K_e = \sigma_0 T_e / T_l$, where $\sigma_0 = 4.5$ W m^{-1} K^{-1}.[127] The electron relaxation time τ_e is about 0.04 ps in the TbFeCo alloys.[128] For parameters of the lattice, this research employed $C_l = 2.3 \times 10^6$ J m^{-3} K^{-1}, $K_l = 1.5$ W m^{-1} K^{-1} and $\tau_l = 0.8$ ps.[129] Moreover, the electron-phonon coupling strength is expressed in terms of electron and lattice temperatures:

$$G = G_{rt}\left(\frac{A_e}{B_l}(T_e + T_l) + 1\right) \tag{7.23}$$

Where $G_{rt} = 1.7 \times 10^{18}$ W m^{-3} K^{-1}, $A_e = 6.6 \times 10^6$ K^{-2} s^{-1} and $B_l = 3.4 \times 10^{12}$ K^{-1} s^{-1} for the RE-TM alloy. It should be noted that these parameters were evaluated through a simple approach, where the alloy components were assumed to contribute the same number of electrons to the metallic bonding in the alloy as in their pure forms. This simplified method provides the best estimation without performing in-depth electronic structure calculations, which is out of the scope of this study. The laser irradiation is generally given by a Gaussian form as indicated by the following equation:

$$S(x,t) = \sqrt{\frac{4\ln 2}{\pi}}\frac{1-R}{\delta t_p} I_0 \exp\left(-\frac{x}{\delta} - 4\ln 2\frac{\left(t-t_p\right)^2}{t_p^2}\right) \tag{7.24}$$

Here R is the reflectivity, δ is the penetration depth, t_p is the FWHM of the Gaussian temporal profile, and I_0 is the fluence of the laser beam. All the related parameters are summarized in Table 7.1. With all of these values, the temperatures of the electrons and lattice were calculated for a 15 nm thick RE-TM alloy thin film in a time scale of picoseconds. Figure 7.3 demonstrates the temporal profiles under femtosecond lasers of different fluences.

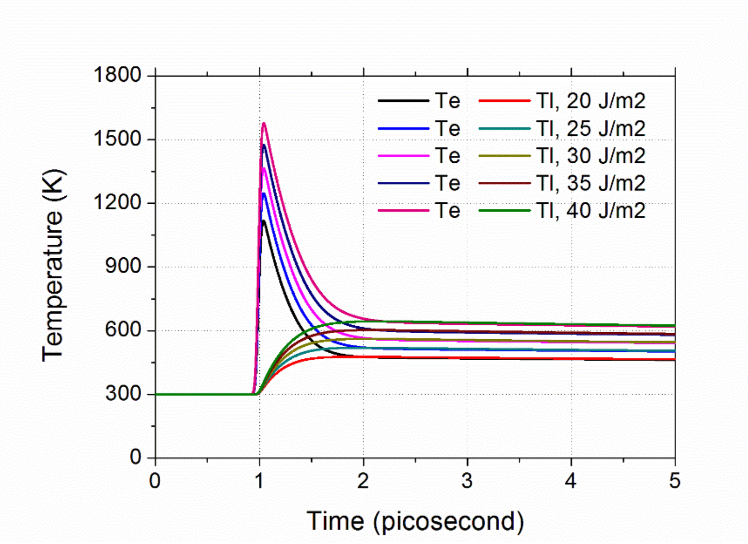

Figure 7.3. Temporal profiles of electron and lattice temperatures were calculated under femtosecond lasers of different fluences.

Table 7.1. Parameters of the phenomenological two-temperature model for RE-TM alloy thin films.

Name	Value	Name	Value
γ	7.0×10^{2} J m^{-3} K^{-2}	A_e	6.6×10^{6} K^{-2} s^{-1}
σ_0	4.5 W m^{-1} K^{-1}	B_l	3.4×10^{12} K^{-1} s^{-1}
τ_e	0.04 ps	R	0.93
C_l	2.3×10^{6} J m^{-3} K^{-1}	δ	15.3 nm
K_l	1.5 W m^{-1} K^{-1}	t_p	50 fs
τ_l	0.8 ps	h	1 nm
G_{rt}	1.7×10^{18} W m^{-3} K^{-1}	Δt	0.1 fs

Figure 7.3 suggests an estimation that after the laser irradiation, the temperatures of electrons and lattice reach equilibrium within 1.0 ps, which is defined as the time scale of the first 3 stages of the laser heating effect as introduced in Chapter 2. Now, to better understand the final stage, i.e. the cooling stage, lateral heat diffusion is estimated by a simplified 2D model that assumes no energy dissipate vertically. Since the cooling stage generally relates to a time scale longer than a few picoseconds, the simple heat equation is applied as:

$$\frac{\partial T}{\partial t} = D\nabla^2 T \tag{7.25}$$

Where D is defined as heat diffusivity $D \equiv K/C$. In the temperature range of interest, the heat diffusivity of RE-TM alloys can be estimated as 2.5×10^{-6} m^2 s^{-1}.[129] Assuming a Gaussian distribution of laser power, the initial temperature profile after the first 1.0 ps can be expressed as:

$$T(r, \phi, t = 0) = \Delta T \exp\left(-\frac{r^2}{2d^2}\right) \tag{7.26}$$

Where d is the laser diameter, e.g. 5 μm. With large enough size of sample surface, e.g. 5 mm, a simplified model can be solved analytically as:

$$T(\boldsymbol{x}, t) = \frac{1}{4\pi Dt}\int \exp\left(-\frac{(\boldsymbol{x} - \boldsymbol{x}')^2}{4Dt}\right) T(\boldsymbol{x}', 0) d^2x' \tag{7.27}$$

Especially, the temperature in the center of the laser spot can be expressed as:

$$T(\mathbf{0}, t) = \frac{\Delta T}{1 + \frac{2Dt}{d^2}} \tag{7.28}$$

Consequently, about 100 μs is needed to cool down the center part of the laser spot to 5% of the temperature difference when only lateral heat diffusion is considered. This time is much longer than the time scale of interest, usually tens of picoseconds. This estimation confirms the correctness of the previous 1D assumption.

To correctly estimate the time scale of the final cooling stage, the substrate, i.e. a 350 nm thick SiO_2 layer, should be taken into account as well. The heat capacity and thermal conductivity of SiO_2 can be found in past literature as $C_{SiO_2} = 2.2 \times 10^6$ J m^{-3} K^{-1} and $K_{SiO_2} = 1.4$ W m^{-1} K^{-1}. Thus, the heat diffusivity of SiO_2 is about 6.4×10^{-7} m^2 s^{-1}. To give an easy estimation of the cooling time, the RE-TM alloy can be assumed to have the same diffusivity as that of SiO_2, while the interface has no resistance of heat diffusion. Without lateral dimensions, this problem can be simplified to a 1D heat diffusion problem. For a simple step-like initial temperature distribution:

$$T(x, t = 0) = \begin{cases} \Delta T, & x < 15\, nm \\ 0, & 15\, nm < x < 365\, nm \end{cases} \tag{7.29}$$

The time-dependent temperature profile can be analytically expressed as:

$$\begin{aligned} T(x,t) &= \frac{\Delta T}{\sqrt{4\pi D t}} \int_{-x_0}^{x_0} \exp\left(-\frac{(x - x')^2}{4Dt}\right) dx' \\ &= \frac{\Delta T}{2}\left(\operatorname{erf}\left(\frac{x_0 - x}{\sqrt{4Dt}}\right) + \operatorname{erf}\left(\frac{x_0 + x}{\sqrt{4Dt}}\right)\right) \end{aligned} \tag{7.30}$$

Especially, the surface temperature is given by:

$$T(0,t) = \Delta T \operatorname{erf}\left(\frac{x_0}{\sqrt{4Dt}}\right) \tag{7.31}$$

This offers an estimation of 50 ns to cool the surface temperature down to 5% of the temperature difference. Moreover, within this time scale, the heat will not dissipate through the 350 nm thick SiO_2 layer.

Comparing both lateral and vertical heat diffusions, it becomes clear that the heat energy mainly transfers downwards into the substrate during the final cooling stage. The time scale difference between the lateral and vertical directions is due to a large laser spot size compared to a nanometer thin film thickness. More importantly, within the scale of 1.0 ps, only 1.6% of energy dissipates into the substrate. This means that an adiabatic boundary is an appropriate estimation for the first 1.0 ps. However, since about 13% of energy dissipates into the substrate within 20 ps, the 2T model cannot be considered as adiabatic for tens of picoseconds. In this study, an analytical boundary temperature can be calculated from Equation 7.30 as:

$$T_{boundary}(t) = T_0 + \frac{\Delta T}{2}\mathrm{erf}\left(\frac{x_0}{\sqrt{D_{SiO_2}t}}\right) \tag{7.32}$$

Where T_0 is the ambient temperature, e.g. 300 K, ΔT is the temperature difference after 1.0 ps, and x_0 is represented by the thickness of the film. With this boundary temperature, the cooling rate could be corrected, as shown in Figure 7.4. Within 10 ps after laser incidence, the temperature profiles calculated with boundaries of adiabatic, corrected or fixed at 300 K, were essentially the same, which indicated a minimum boundary effect to the ultrafast magnetic dynamics within 10 ps.

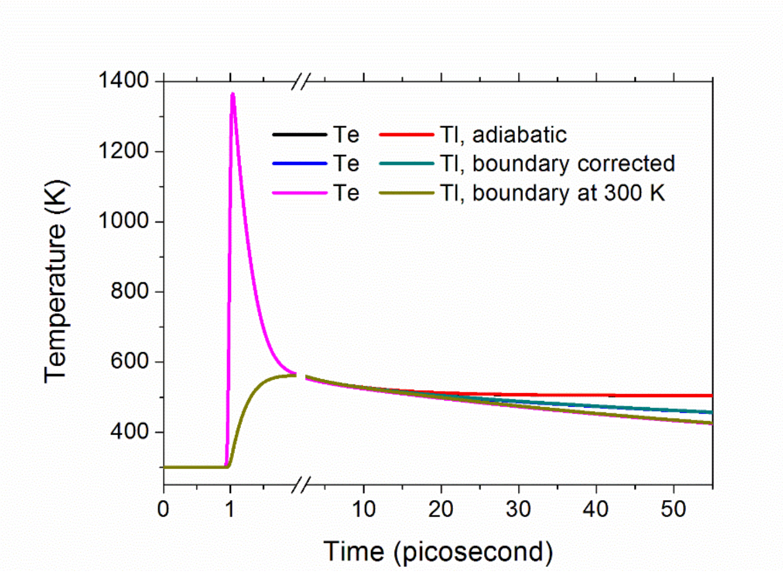

Figure 7.4. Temporal profiles of electron and lattice temperatures were calculated with boundaries of adiabatic, corrected, and fixed at 300 K.

The following simulations mainly focus on a time scale as large as a few picoseconds. Beyond that, the thin films are in the final cooling stage. Their magnetic properties are then reaching thermal equilibrium without any temperature stimulus near or above their Curie temperature. Therefore, the cooling of thin films will be safely omitted after 50 ps in order to save computational costs. However, it is important to note that the real cooling time is just estimated to be as long as 50 ns.

7.3 Ultrafast Magnetization Reversal of RE-TM Alloys

7.3.1 All-Optical Switching and Ultrafast Magnetization Reversal

RE-TM alloys have been investigated for their magneto-optical recording in the 1980's.[97] Recently, there are rising interests in this system because of its unique ultrafast magnetization dynamics. Especially, all-optical switching (AOS) has been discovered[12,67]: the magnetization of RE-TM alloys can be reversed, purely driven by circularly polarized femtosecond laser pulses, which implies an ultrafast mechanism for novel spintronic devices. Not only in RE-TM alloys, but the AOS has also been experimentally recognized in RE-TM multilayers and synthetic ferrimagnetic multilayers.[14]

7.3.2 Ultrafast Magnetization Reversal of Amorphous $Gd_{25}Fe_{75}$ Alloys

Even though the AOS has been experimentally proven in many ferrimagnetic systems, the underlying physics remains elusive. The sub-picosecond time scale makes this problem more difficult than conventional spin dynamic problems. One possible way to consider the thermal effect of ultrafast laser pulses is to solve the dynamics based on a phenomenological two-temperature model, as discussed in the previous section. Compared to the more complete three-temperature model, the spin temperature is regarded to be the same as that of the electron in the two-temperature model, given their fast relaxation time.

As a first step, an atomistic Heisenberg model of pure Fe and Gd was built on the FCC lattice similar to that in Chapter 4. The lattice space consisted of 32 × 32 × 32 sites in total. Periodic boundary conditions were employed to all axes, given the dimension of each edge to only be about 6 nm. No external field was applied throughout the study of this chapter. To be compared with experimental and numerical results from peer groups, the same set of parameters were applied as in Ostler et al.'s research[94], which are summarized in Table 7.2.

Table 7.2. Parameters for modeling ultrafast magnetization dynamics. From Ostler et al.[94]

Parameter	Value	Parameter	Value
μ_{Gd}	7.63 μ_B	λ_{Gd}	0.05
μ_{Fe}	2.217 μ_B	λ_{Fe}	0.05
J_{Gd-Gd}	1.26×10^{-21} J/link	γ_{Gd}	1.76×10^{11} radT^{-1}s^{-1}
J_{Fe-Fe}	2.83×10^{-21} J/link	γ_{Fe}	1.85×10^{11} radT^{-1}s^{-1}
J_{Gd-Fe}	-1.09×10^{-21} J/link	Lattice	32 × 32 × 32
D	8.07×10^{-24} J/atom	Boundary Condition	Periodic

As shown in Figure 7.5, both of the pure Fe and Gd exhibited an ultrafast demagnetization by a 50 fs laser at 20 J/m^2 fluence. However, the relaxation time of Fe was shorter than that of Gd, making the magnetization of Fe able to reduce and recover in a shorter span of time. Moreover, by increasing laser fluence, the demagnetization effect tended to be stronger for both Fe and Gd, which meant a longer time for magnetization recovery. Finally, it was clear that no ultrafast switching could be observed for the laser fluence less than 50 J/m^2.

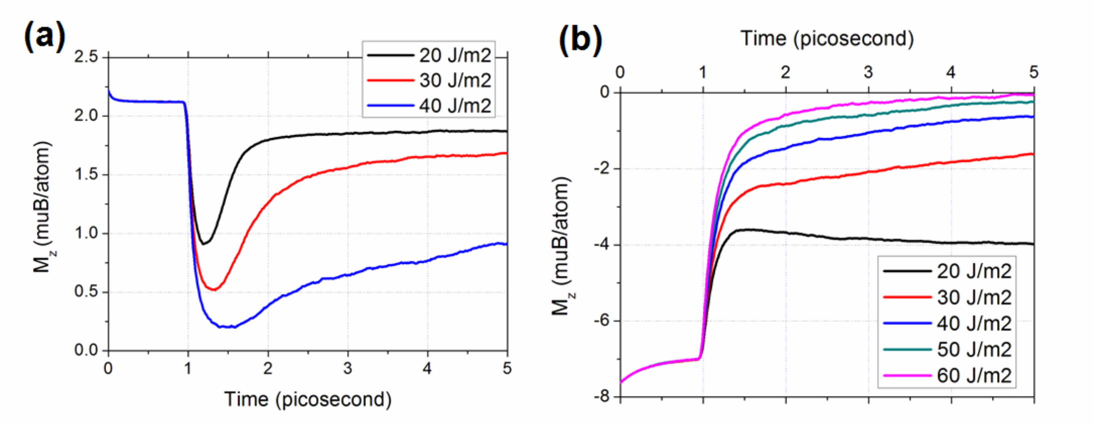

Figure 7.5. Ultrafast demagnetization of Fe (a) and Gd (b) was simulated by a 50 fs laser under different fluences.

Next, the amorphous $Gd_{25}Fe_{75}$ alloys were generated based on a similar pseudo amorphous structure presented in Chapter 4. The temporal magnetization profiles were simulated under the same 50 fs laser pulses with a fluence of 30 J/m^2. As is shown in Figure 7.6, the laser pulses pumped up electron temperature to about 1500 K in 0.1 ps, which was well above the compensation temperature and even over its Curie temperature. This thermal stimulus drove the spins of both Gd and Fe sublattices out of their equilibrium and demagnetized both sublattices, the same as exhibited with pure Fe and Gd. However, due to the distinct relaxation time of the Gd and Fe sublattices, a transient ferromagnetic-like state was created.[94] During this transient state, Fe spins were flipped over and aligned parallel to the spins of Gd. This reversal had been explained by a two-mageon mode that assisted the magnetization reversal of Gd.[95] Meanwhile, as heat transferred from the electrons to lattice, the electron temperature dropped quickly and the reversed magnetization of both sublattices recovered to its original magnitude. The perpendicular magnetic anisotropy of the RE-TM alloys made the equilibrated state stable at an ambient temperature of 300 K.

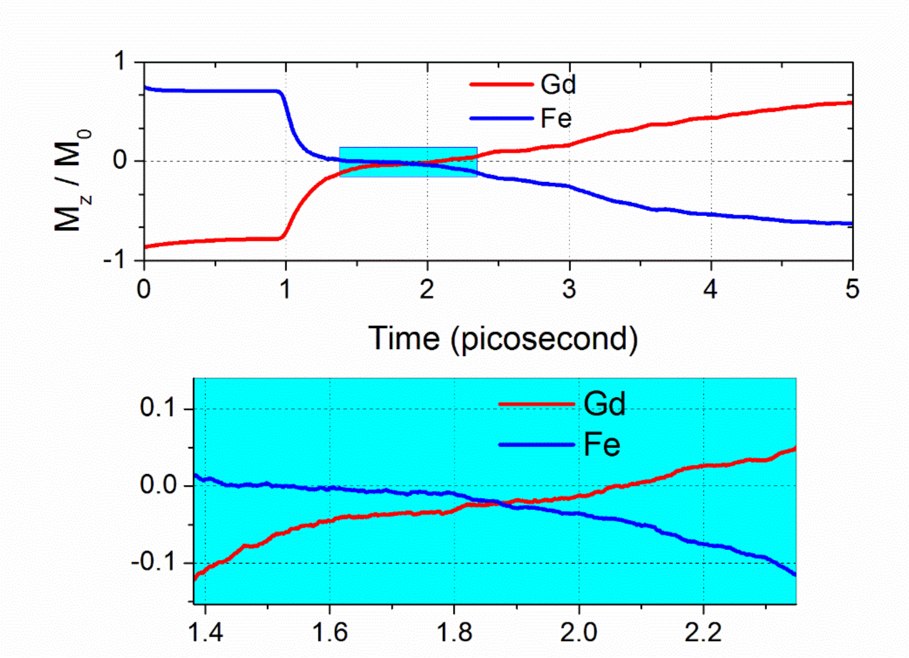

Figure 7.6. Ultrafast magnetization reversal of an amorphous $Gd_{25}Fe_{75}$ alloy was simulated by a 50 fs laser of 30 J/m^2 fluence. The zoom-in figure shows a transient ferromagnetic-like state.

The amorphous $Gd_{25}Fe_{75}$ alloy was also studied under an increasing laser fluence as shown in Figure 7.7. The magnetization reversal could only be induced by a laser with a large enough fluence, for example, 30 J/m^2. However, as the fluence continued increasing, the magnetization recovery took a longer time due to more laser energy transferred to the alloy. For an extreme case of a very large fluence, assuming the sample were not melted by such a strong laser, the magnetization would be completely demagnetized and the magnetization reversal would occur by a 50% chance without the help of any external field.

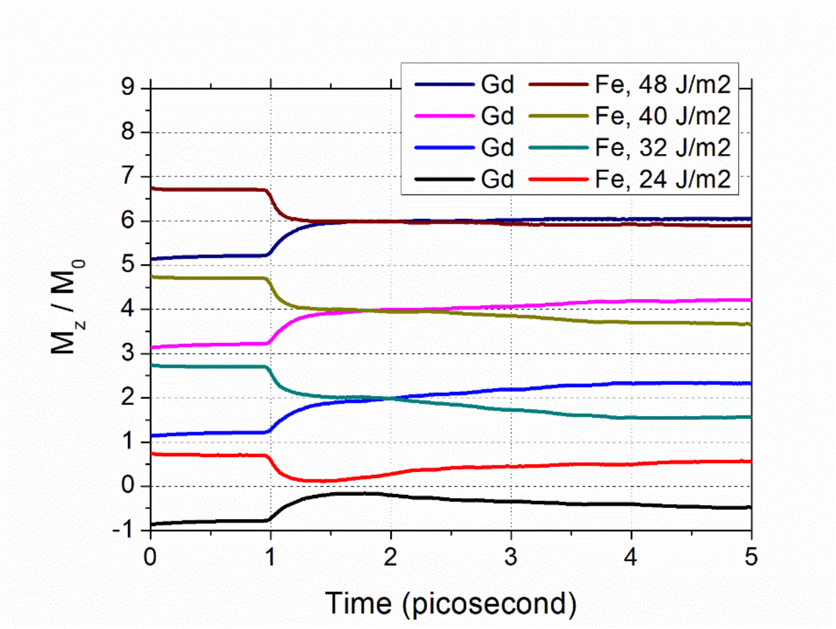

Figure 7.7. Ultrafast magnetization dynamics were simulated of an amorphous $Gd_{25}Fe_{75}$ alloy by 50 fs lasers with an increasing fluence from 24 J/m^2 to 48 J/m^2.

Moreover, multiple independent runs were performed with different random number seeds under the fluence of 35 J/m^2 as shown in Figure 7.8. These results verified the determinism of this heat-induced magnetization reversal. This fact implies a unique mechanism of ferrimagnetic materials exists that is responsible for the deterministic process, since no directional preference is stimulated by a random heat source, for example, an ultrafast laser source. Figure 7.8 (a) provides a zoom-in plot of the ferrimagnetic transient state for each run.

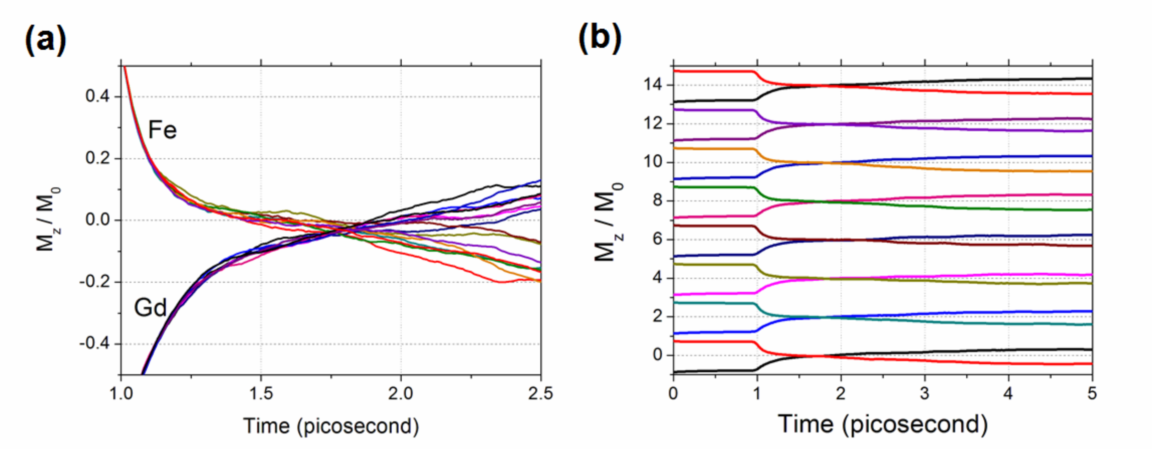

Figure 7.8. Ten independent runs of ultrafast magnetization reversal were performed of an amorphous $Gd_{25}Fe_{75}$ alloy by a 50 fs laser of 35 J/m^2 fluence. Different random seeds were generated for the random number generator of each run. A zoom-in plot of transient ferromagnetic-like state is shown in (a) for each run.

Furthermore, as expected, the determinism suffered from the elevated randomness under a higher laser fluence, e.g. 50 J/m^2. As is shown in Figure 7.9, the reversal became highly ambiguous due to a longer recovery time. Zoom-in plots are provided in Figure 7.9 (a).

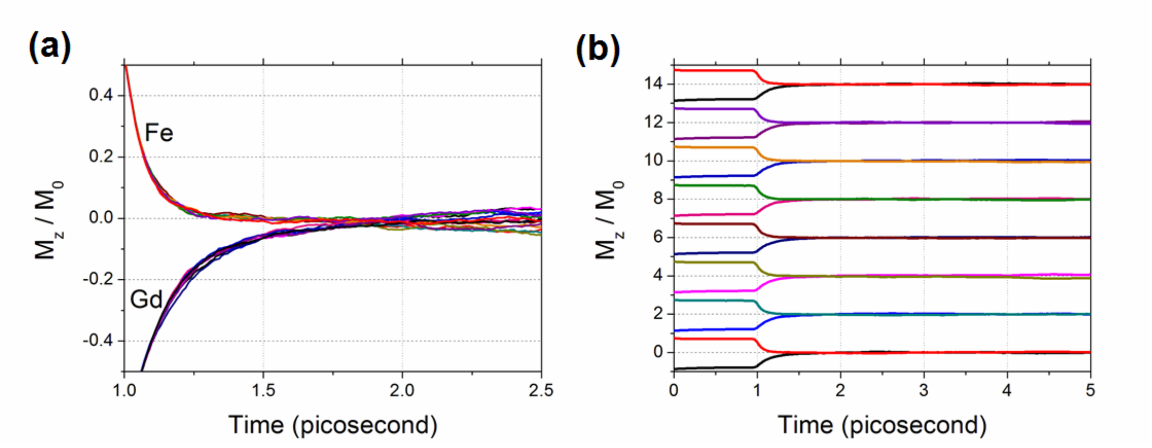

Figure 7.9. Ten independent runs of ultrafast magnetization dynamics were performed of an amorphous $Gd_{25}Fe_{75}$ alloy by a 50 fs laser of 50 J/m^2 fluence. Different random seeds were generated for the random number generator of each run. A zoom-in plot is shown in (a) for each run.

Finally, as a demonstration, a serial of laser pulses were input on this simple atomistic model with a repetition rate of 20 MHz. As seen in Figure 7.10, the deterministic magnetization reversal happened within 10 ps after the incidence of each laser pulse. This implies applications of the heat-induced ultrafast magnetization reversal for novel spintronic devices.

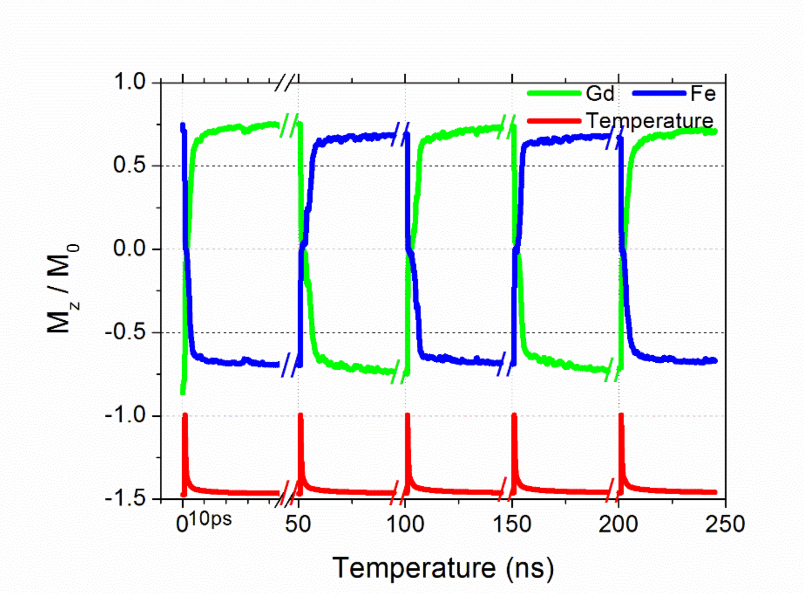

Figure 7.10. Ultrafast magnetization reversal of an amorphous $Gd_{25}Fe_{75}$ alloy by 50 fs laser pulses of 30 J/m^2 fluence with a repetition rate of 20 MHz.

7.3.3 Compositional and Fluence Dependence of Reversal Probability

As reported by both numerical and experimental results, the ultrafast magnetization reversal happened only for a certain range of compositions. As shown in Figure 7.11, the reversal was only observed for Gd 25 at. % with a laser fluence of 35 J/m^2.

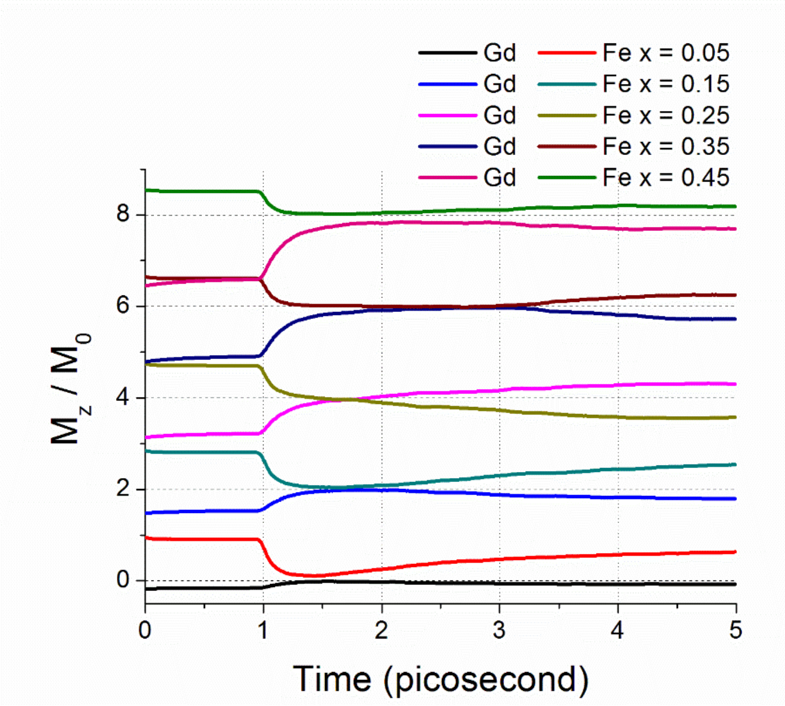

Figure 7.11. Ultrafast magnetization dynamics were simulated of amorphous Gd_xFe_{1-x} alloys by a 50 fs laser of 35 J/m^2 fluence.

On the other hand, the fluence dependence was revealed in Figure 7.12, where amorphous alloys of Gd 25 at. % and Gd 30 at. % were simulated under an increasing fluence near 30 J/m^2. Based on the results of these runs, the laser threshold could be roughly determined as 28.0 J/m^2 and 28.5 J/m^2 for $Gd_{25}Fe_{75}$ and $Gd_{30}Fe_{70}$ respectively. However, due to the stochastic feature near threshold fluence, a quantitative picture of fluence dependence is highly desirable.

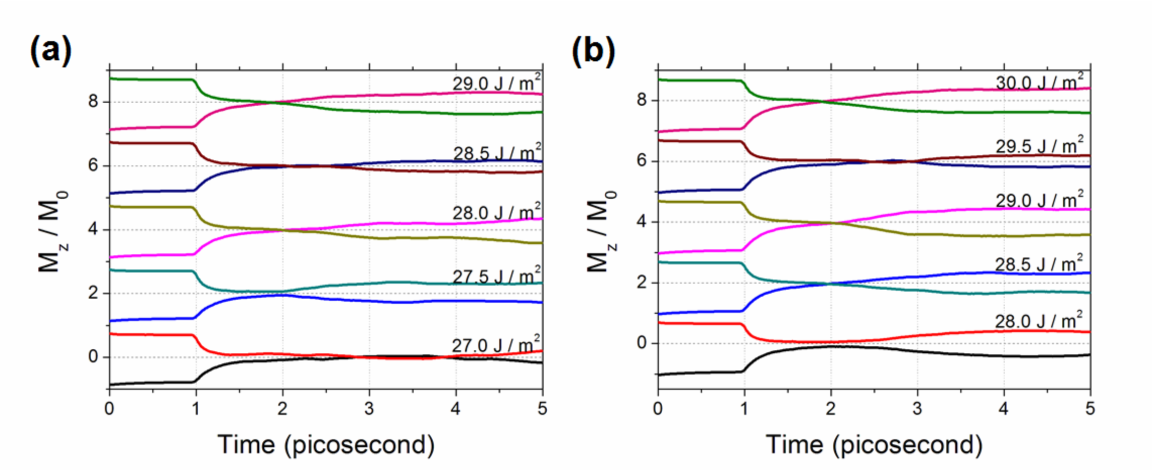

Figure 7.12. Ultrafast magnetization dynamics of Gd 25 at. % (a) and 30 at. % (b) were simulated by 50 fs laser pulses of an increasing fluence near 30 J/m^2.

The reversal probability was thus chosen as a quantitative figure of merit for the present study:

$$P_R \equiv \frac{N_{reversed}}{N_{total}} \tag{7.33}$$

With the help of the high performance computing clusters, e.g. the Rivanna, it is possible to run hundreds of independent jobs and analyze the results in a reasonable amount of time. Here, for each condition, a total of 256 independent runs (with different random number seeds) were performed on the Rivanna. By the completion time, the reversal probability was calculated as the number of the reversed cases over the number of total cases, i.e. 256.

As Figure 7.13 shows, the reversal probability vs. Gd at. % was plotted for the laser fluence of 30 J/m^2. An obvious compositional dependence was revealed quantitatively by a bell shape curve, the reversal being strictly forbidden for Gd at. % below than 15% or higher than 40%. To the contrary, within a range from 25% to 35%, the reversal probability was higher than 90%, which was moderately deterministic. For Gd at. 27.5%, the maximum reversal probability of 97% was reached. For the rest of the concentration, intermediate reversal probability were observed from 10% to 80%.

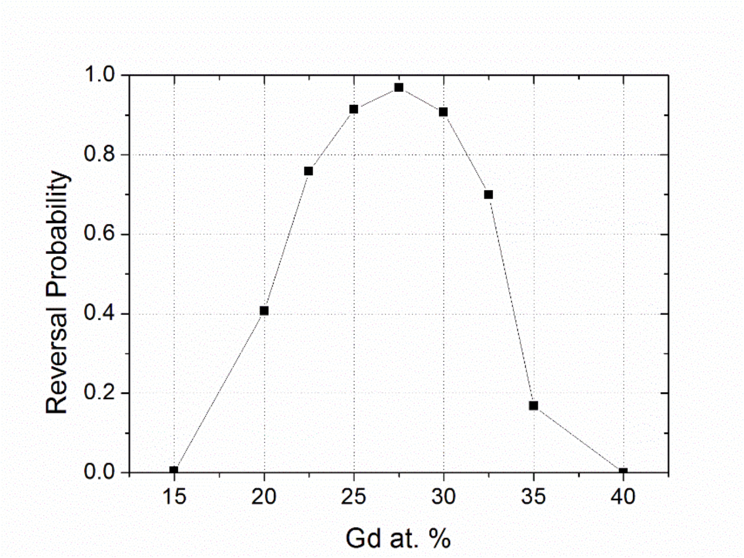

Figure 7.13. Reversal probability vs. Gd at. %. Each data point was analyzed from a total of 256 parallel independent runs. A 50 fs laser was used with 30 J/m^2 fluence.

Figure 7.14 presents a combined picture of both compositional and fluence dependence of the reversal probability. In this figure, a series of curves are presented for variations of Gd at. % from 15% to 35%. For each curve, there existed a window of laser fluence, under which the reversal probability had a maximum. For example, the reversal probability of Gd at. 27.5% quickly ramped up to 90% from 25 J/m^2 to 30 J/m^2, which indicated a reasonable threshold fluence of 30 J/m^2. This deterministic reversal (over 90%) lasted from 30 J/m^2 to 40 J/m^2. After that, the reversal probability dropped slowly. It should be noted that instead of dropping to 50% for a full demagnetization, this probability would reduce below 50% again for fluence higher than 55 J/m^2. This suggests there exists a more complicated response to the laser stimulation under a high fluence laser, other than a simple thermal demagnetization.

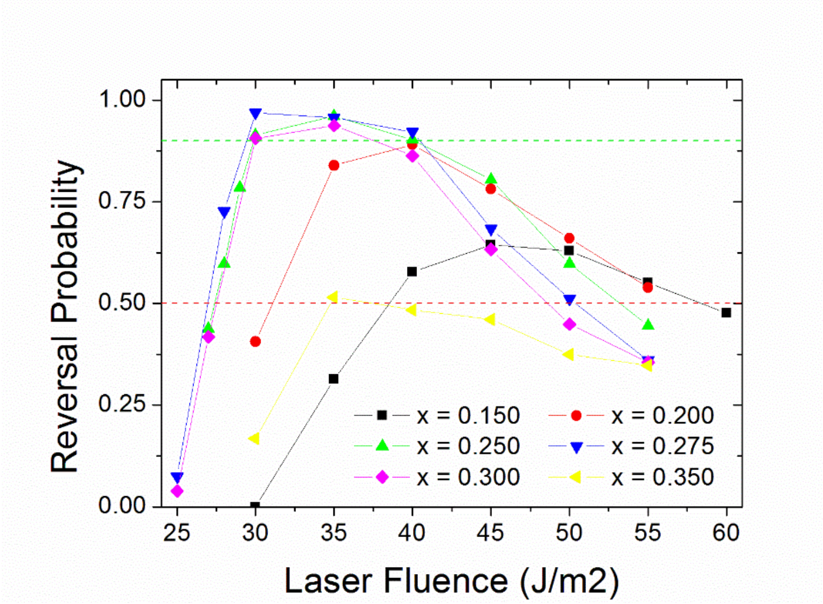

Figure 7.14. Reversal probability vs. laser fluence of amorphous Gd_xFe_{1-x} alloys. Each data point was analyzed from a total of 256 parallel independent runs.

More importantly, the deterministic reversal in the present study only existed for a certain range of compositions. Specifically, Gd 15 at. % and 35 at. % were not able to provide a deterministic reversal for the whole range of fluence. This phenomenon was explained by the lack of compensation temperature in past research.[98] However, an observation of the deterministic reversal in Gd 20 at. % provided a contradictory. As shown in Figure 7.15, no compensation temperature existed for this Gd 20 at. % either. This numerical result was also supported by experimental work of Mangin et al.[14], where ultrafast reversal was observed even without compensation.

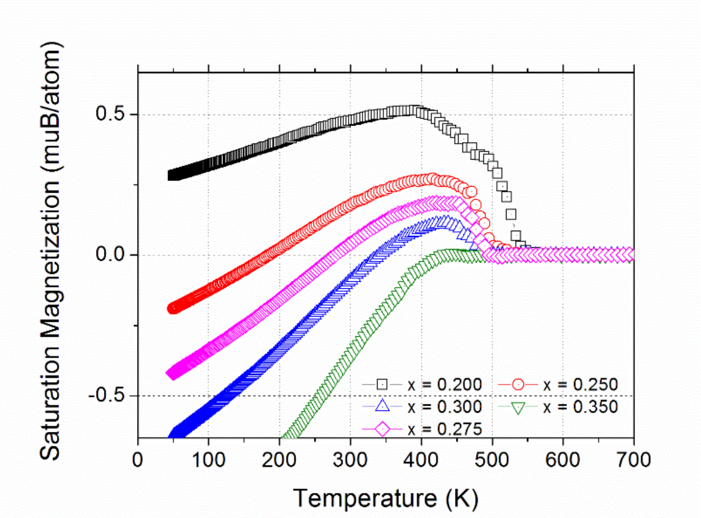

Figure 7.15. Saturation magnetization vs. temperature curves of amorphous Gd_xFe_{1-x} alloys. The curves were simulated by the parallel tempering functionality of the MMP.

7.3.4 Reversal Probability and Gd-Fe Pair Ratio

The method, which stems from the research presented in Chapter 5, can be used to quantitatively explore the dependence of ultrafast reversal on different Gd-Fe pair ratios. The present study generated atomistic amorphous structures with a variation of Gd-Fe pair ratios on FCC lattices, similar to the pseudo model in Chapter 4. Due to the restriction of the crystal FCC lattice, a nanoscale compositional separation could be noted for low Gd-Fe pair ratios, e.g. 0.2, as shown in Figure 7.16.

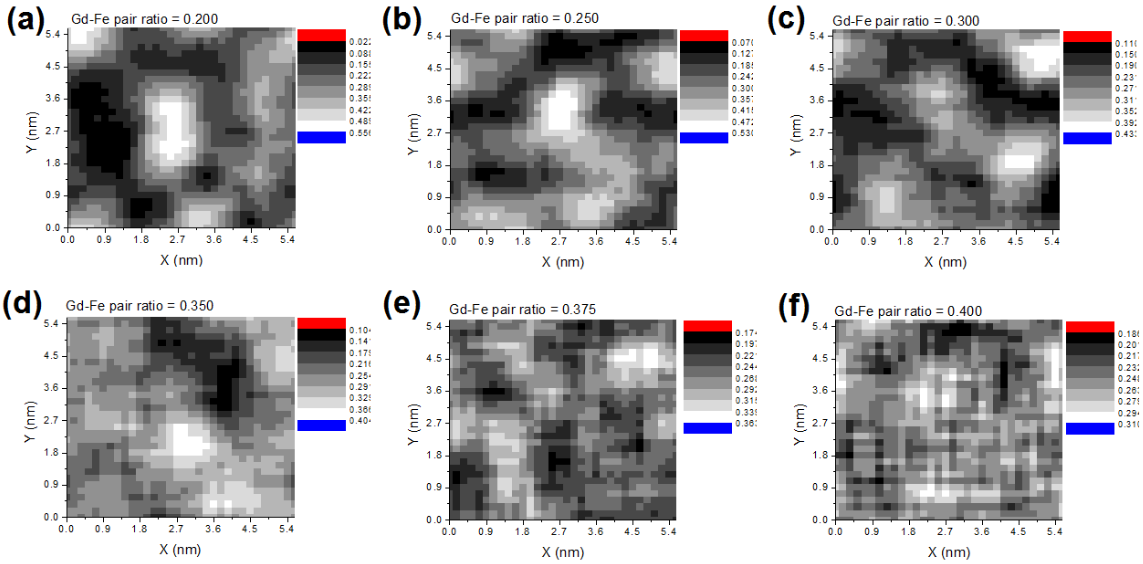

Figure 7.16. 2D compositional maps of amorphous $Gd_{25}Fe_{75}$ alloys with a variation of Gd-Fe pair ratios. Color bar indicates Gd at. %.

Figure 7.17 presents testing results of all structures under fluence of 35 J/m^2. Fortunately, all structures were able to be successfully reversed for this run. However, the switching time was clearly pushed away for lower Gd-Fe pair ratio. This implies a variation of reversal probability for these structures.

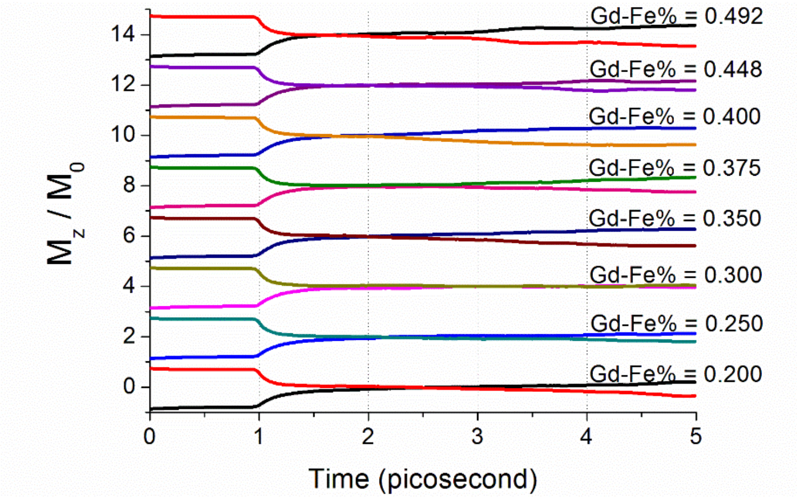

Figure 7.17. Ultrafast magnetization dynamics of amorphous $Gd_{25}Fe_{75}$ alloys with different Gd-Fe pair ratio. These curves were simulated just once by a 50 fs laser pulse of 35 J/m^2 fluence.

As demonstrated in Figure 7.18, the quantitative reversal probability is plotted as a function of the Gd-Fe pair ratio. The deterministic reversal only occurred for a Gd-Fe pair ratio ranging from 0.35 to 0.45. As the pair ratio decreased, the reversal probability reduced, which was likely due to the nanoscale phase segregation. However, the reversal probability unexpectedly decreased for higher Gd-Fe pair ratios. This implies an optimal antiferromagnetic interaction strength between Gd and Fe sublattices needs to be present in order to obtain the most efficient reversal.

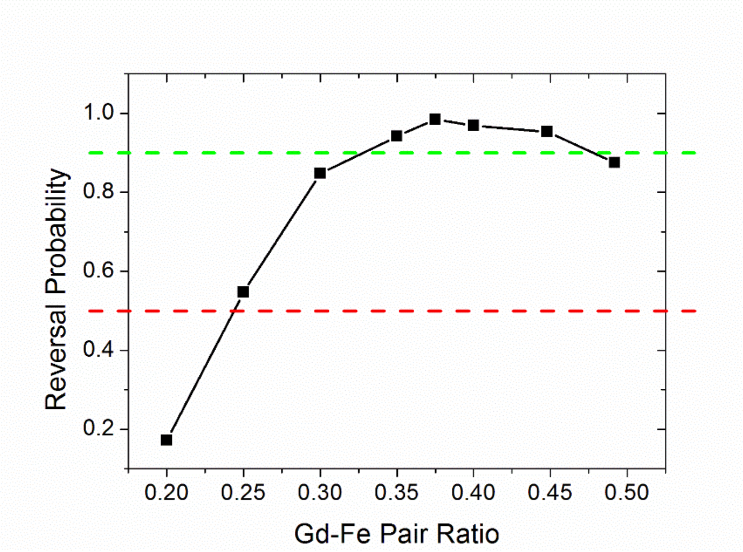

Figure 7.18. Reversal probability vs. Gd-Fe pair ratio of amorphous $Gd_{25}Fe_{75}$ alloys. Each point was analyzed from a total of 265 parallel independent runs. A 50 fs laser was used with fluence of 35 J/m^2.

7.4 Ultrafast Magnetization Reversal of $[Gd(t)/Fe(3t)]_n$ Mutilayers

The previous study presents examination of the ultrafast magnetization reversal in amorphous $Gd_{25}Fe_{75}$ alloys and highlights its dependence on laser fluence, atomic concentration, and Gd-Fe pair ratio. However, in order to engineer the properties of this ultrafast magnetization reversal, layered structures are usually more practical than amorphous alloys. Therefore, a series of $[Gd(t)/Fe(3t)]_n$ multilayers were investigated in order to verify the influence of the layer period variation. Composition was kept the same, i.e. Gd 25 at. %, throughout the current study, by choosing layer period of Gd vs. that of Fe as 1:3. Cross-sections of the multilayers are plotted in Figure 7.19.

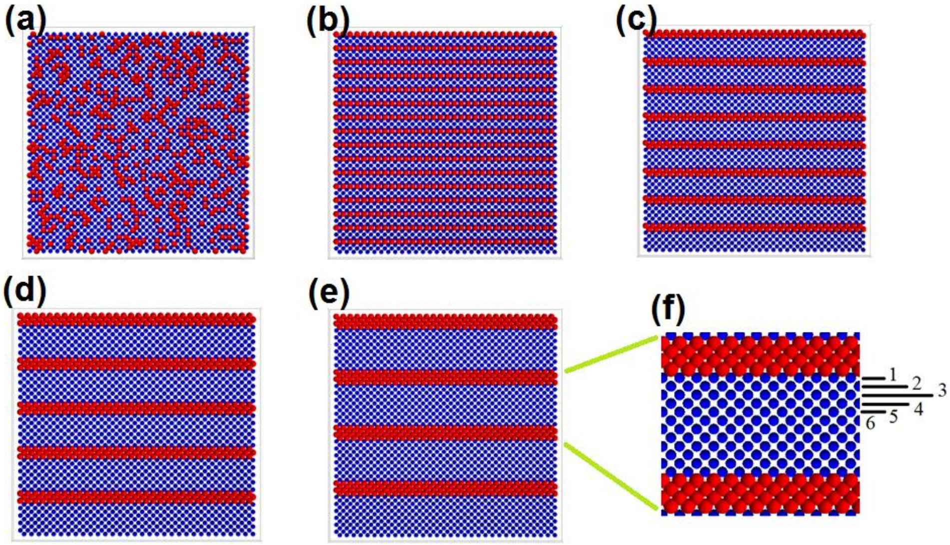

Figure 7.19. Cross-sectons of (a) amorphous $Gd_{25}Fe_{75}$ alloy, (b) $[Gd(1)/Fe(3)]_{16}$, (c) $[Gd(2)/Fe(6)]_{8}$, (d) $[Gd(3)/Fe(9)]_{5}$, (e) $[Gd(4)/Fe(12)]_{4}$, and (f) a zoom-in plot of unit layers in (e).

As shown in Figure 7.20, the magnetization reversal tended to be harder with a constant laser fluence of 35 J/m^2, when the layer period became larger. Specifically, the $[Gd(3)/Fe(9)]_5$ failed to provide a deterministic reversal.

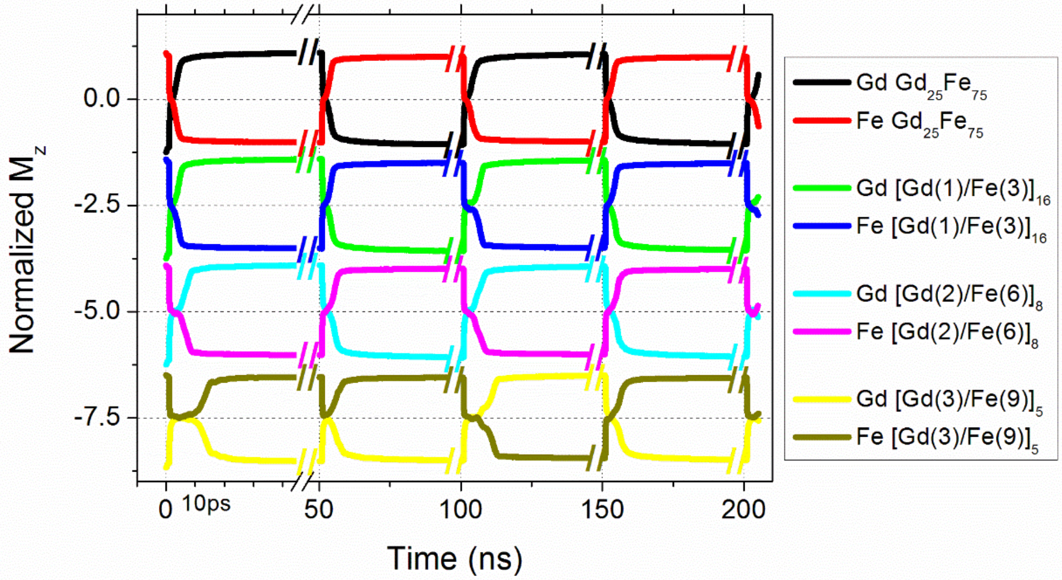

Figure 7.20. Ultrafast magnetization dynamics of amorphous $Gd_{25}Fe_{75}$ alloy and $[Gd(t)/Fe(3t)]_n$ multilayers. 50 fs laser pulses were used with a constant fluence of 35 J/m^2.

This is confirmed by a numerical study with an increasing laser fluence in Figure 7.21. For the multilayers of $[Gd(4)/Fe(12)]_4$, the fluence threshold could be estimated as 42 J/m^2, which corresponded to the third laser pulse. This threshold was higher than 30 J/m^2 of the amorphous $Gd_{25}Fe_{75}$ alloys.

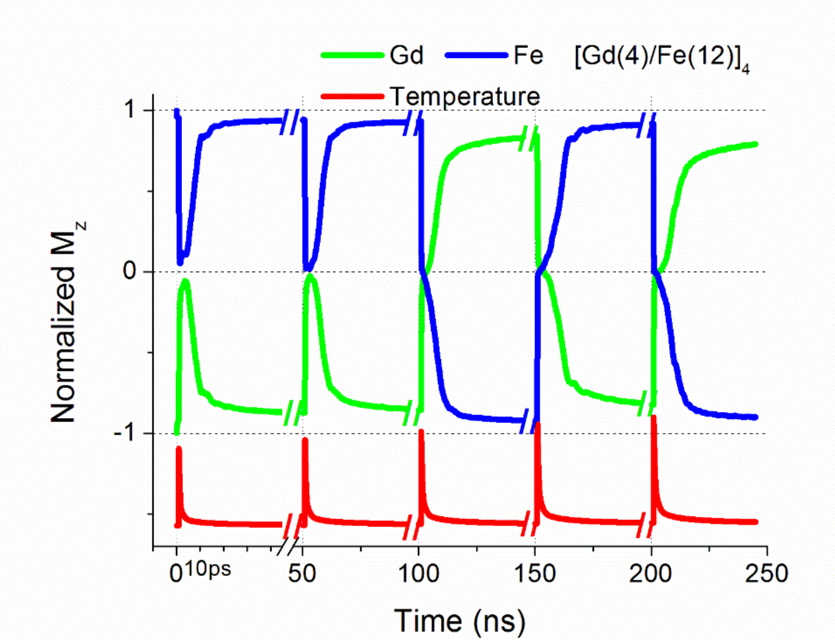

Figure 7.21. Ultrafast magnetization dynamics of [Gd(4)/Fe(12)]$_4$ multilayers. 50 fs laser pulses were used with an increasing laser fluence.

7.5 Concluding Remarks

This chapter characterized the ultrafast optical response of the RE-TM films by a simplified phenomenological two-temperature model. The highly non-equilibrium temperature of the electrons has been applied as an ultrafast heat stimulus (about 1 ps) to examine the ultrafast magnetization dynamics of the RE-TM system, particularly, ferrimagnetic GdFe, by atomistic simulations.

All-optical switching (AOS) has been realized numerically in the simple pseudo amorphous GdFe structures. The determinism of the magnetization reversal has been quantitatively studied as a function of relevant conditions, such as laser fluence, atomic concentration, and Gd-Fe pair ratio. This has numerically revealed that there exists a window for the deterministic magnetization reversal, where the reversal probability is greater than 90%. The highest reversal probability has been obtained as 97% for amorphous $Gd_{27.5}Fe_{72.5}$ with a Gd-Fe pair ratio of 0.375, driven by 50 fs laser pulses with fluence of 30 J/m^2. Finally, the fluence threshold was demonstrated in Gd/Fe multilayers. Higher laser fluence was shown to be necessary to deterministically drive the Gd/Fe multilayers with an increasing layer period.

CHAPTER 8 CONCLUSION AND FUTURE WORK

As a summary of this dissertation, in Chapter 4, the fundamentals of the magnetic numerical modeling were introduced, including the atomistic Heisenberg model, the Monte Carlo Metropolis/parallel tempering algorithms, the atomistic Landau-Lifshitz-Gilbert (LLG) method, and the micromagnetic Landau-Lifshitz-Bloch (LLB) method. These basic methods were then programmed from ground up in C++, and combined into a magnetic modeling package (MMP). Employing the MMP, consistent results were reproduced for the pseudo amorphous GdFe alloys compared with past research.

In Chapter 5, a large perpendicular magnetic anisotropy (PMA) has been verified for a wide range of temperatures in both the single-sputtered and the co-sputtered amorphous TbFeCo thin films. The temperature dependence of the saturation magnetization has been measured by a vibrating sample magnetometer (VSM) experimentally, showing a tunable compensation temperature near the room temperature. Specifically, an obvious thickness dependence has been confirmed in both the single-sputtered and the co-sputtered sample sets of increasing thicknesses, where higher compensation temperatures have been consistently observed for thicker films.

An atomistic model, based on an ab-initio amorphous structure, has been proposed to better understand the experimental thickness dependence. A depth profile of the Tb-Fe pair ratio has been introduced by a minimum modification through a random pair swap and a random close pack. This model effectively explains the thickness dependence of both sample sets on equal footing. Consistent temperature dependent magnetization curves have been predicted and compared to the experimental observations. This study numerically confirmed the possibility of depth profiles of heterogeneous structures in the sputtered amorphous thin films.

Furthermore, polarized neutron reflectometry measurements have been proposed to examine both compositional and magnetic depth profiles of the sputtered samples. These experiments will correlate with the numerical simulations, and provide direct verification of the speculated heterogeneity.

Chapter 6 provides experimental evidence of exchange bias (EB) in the co-sputtered amorphous Tb(Sm)FeCo thin films. The EB is closely related to the two growth-induced nanoscale phases distributed throughout the film, which were observed using scanning transmission electron microscopy (STEM) and atom probe tomography (APT). This exchange-biased thin film has many appealing properties such as the large PMA and room-temperature capability. Moreover, the amorphous thin film requires no epitaxial growth and specific substrates. The bistable magneto-resistance (MR) states associated with the EB were proven to be stable at room temperature and switchable by sweeping the magnetic field.

A numerical study of the EB in the ferrimagnetic core-and-matrix geometry has been performed atomistically by the MMP. This simple model predicted the temperature response of the ferrimagnetic EB, which agreed with the empirical experimental results. Larger scale numerical models for the experimental nanoscale phase-separated system have been proposed in the micromagnetic frame. The micromagnetic formulation, together with the stochastic LLG method, has led to preliminary results that were qualitatively consistent to the experimental observations, thus providing numerical supports for the EB when induced by nanoscale two-phase separation. Further study has also been proposed to employ this micromagnetic model with the stochastic LLB method, in order to predict accurate temperature dependence of the ferrimagnetic EB in a phase-separated system.

Chapter 7 characterized the ultrafast optical response of the RE-TM films by a simplified phenomenological two-temperature model. The highly non-equilibrium temperature of the electrons has been applied as an ultrafast heat stimulus (about 1 ps) to examine the ultrafast magnetization dynamics of the RE-TM system, particularly, ferrimagnetic GdFe, by atomistic simulations.

All-optical switching (AOS) has been realized numerically in the simple pseudo amorphous GdFe structures. The determinism of the magnetization reversal has been quantitatively studied as a function of relevant conditions, such as laser fluence, atomic concentration, and Gd-Fe pair ratio. This has numerically revealed that there exists a window for the deterministic magnetization reversal, where the reversal probability is greater than 90%. The highest reversal probability has been obtained as 97% for amorphous $Gd_{27.5}Fe_{72.5}$ with a Gd-Fe pair ratio of 0.375, driven by 50 fs laser pulses with fluence of 30 J/m^2.

Further experiments utilizing femtosecond laser pulses have been proposed to directly verify the numerical findings, especially the optimized window for a deterministic ultrafast magnetization reversal of an amorphous RE-TM alloy. Finally, the fluence threshold was numerically demonstrated in Gd/Fe multilayers. Higher laser fluence was shown to be necessary to deterministically drive the Gd/Fe multilayers with an increasing layer period.

REFERENCE

1. Baibich, M. N. *et al.* Giant magnetoresistance of (001) Fe/(001) Cr magnetic superlattices. *Phys. Rev. Lett.* **61,** 2472–2475 (1988).

2. Binasch, G., Grünberg, P., Saurenbach, F. & Zinn, W. Enhanced magnetoresistance in layered magnetic structures with antiferromagnetic interlayer exchange. *Phys. Rev. B* **39,** 4828–4830 (1989).

3. Ikeda, S. *et al.* Tunnel magnetoresistance of 604% at 300 K by suppression of Ta diffusion in CoFeB/MgO/CoFeB pseudo-spin-valves annealed at high temperature. *Appl. Phys. Lett.* **93,** 82508 (2008).

4. Wolf, S. A. *et al.* Spintronics: a spin-based electronics vision for the future. *Science (80-.).* **294,** 1488–95 (2001).

5. Ralph, D. C. & Stiles, M. D. Spin transfer torques. *J. Magn. Magn. Mater.* **320,** 1190–1216 (2008).

6. Apalkov, D. *et al.* Spin-Transfer Torque Magnetic Random Access Memory (STT-MRAM). *ACM J. Emerg. Technol. Comput. Syst.* **9,** 1–35 (2013).

7. Charap, S. H., Pu-Ling Lu & Yanjun He. Thermal stability of recorded information at high densities. *IEEE Trans. Magn.* **33,** 978–983 (1997).

8. Nishimura, N. *et al.* Magnetic tunnel junction device with perpendicular magnetization films for high-density magnetic random access memory. *J. Appl. Phys.* **91,** 5246–5249 (2002).

9. Beaurepaire, E., Merle, J.-C., Daunois, A. & Bigot, J.-Y. Ultrafast Spin Dynamics in Ferromagnetic Nickel. *Phys. Rev. Lett.* **76,** 4250 (1996).

10. Prejbeanu, I. L. *et al.* Thermally assisted MRAM. *Handb. Spintron.* **19,** 1065–1100 (2007).

11. Kryder, M. H. *et al.* Heat Assisted Magnetic Recording. *Proc. IEEE* **96,** 1810–1835 (2008).

12. Hassdenteufel, A. *et al.* Thermally assisted all-optical helicity dependent magnetic

switching in amorphous Fe100-xTbx alloy films. *Adv. Mater.* **25,** 3122–3128 (2013).

13. Schubert, C. *et al.* All-optical helicity dependent magnetic switching in an artificial zero moment magnet. *Appl. Phys. Lett.* **104,** 82406 (2014).

14. Mangin, S. *et al.* Engineered materials for all-optical helicity-dependent magnetic switching. *Nat. Mater.* **13,** 286–292 (2014).

15. Parkin, S. S. P., Hayashi, M. & Thomas, L. Magnetic Domain-Wall Racetrack Memory. *Science (80-.).* **320,** 190–194 (2008).

16. Yu, X. Z. *et al.* Skyrmion flow near room temperature in an ultralow current density. *Nat. Commun.* **3,** 988 (2012).

17. Sampaio, J., Cros, V., Rohart, S., Thiaville, A. & Fert, A. Nucleation, stability and current-induced motion of isolated magnetic skyrmions in nanostructures. *Nat. Nanotechnol.* **8,** 839–44 (2013).

18. Lee, J. C. T. *et al.* Synthesizing skyrmion bound pairs in Fe-Gd thin films. *Appl. Phys. Lett.* **109,** (2016).

19. Néel, L. * PROPRIETES MAGNETIQUES DES FERRITES-FERRIMAGNETISME ET ANTIFERROMAGNETISME. in *Annales de Physique* **3,** 137–198 (1948).

20. Coey, J. M. D. *Magnetism and Magnetic Materials*. *Journal of Magnetism and Magnetic Materials* (Cambrige University Press, 2010). doi:10.1017/CBO9780511845000

21. Elezzabi, A. Y. & Freeman, M. R. Ultrafast magneto-optic sampling of picosecond current pulses. *Appl. Phys. Lett.* **68,** 3546–3548 (1996).

22. Atoneche, F. *et al.* Large ultrafast photoinduced magnetic anisotropy in a cobalt-substituted yttrium iron garnet. *Phys. Rev. B* **81,** 214440 (2010).

23. Mimura, Y., Imamura, N., Kobayashi, T., Okada, A. & Kushiro, Y. Magnetic properties of amorphous alloy films of Fe with Gd, Tb, Dy, Ho, or Er. *J. Appl. Phys.* **49,** 1208–1215 (1978).

24. Hansen, P., Clausen, C., Much, G., Rosenkranz, M. & Witter, K. Magnetic and magneto-optical properties of rare-earth transition-metal alloys containing Gd, Tb, Fe, Co. *J. Appl. Phys.* **66,** 756–767 (1989).

25. Sayama, J., Asahi, T., Mizutani, K. & Osaka, T. Newly developed SmCo5 thin film with perpendicular magnetic anisotropy. *J. Phys. D. Appl. Phys.* **37,** L1–L4 (2004).

26. Wurmehl, S., Kandpal, H. C., Fecher, G. H. & Felser, C. Valence electron rules for prediction of half-metallic compensated-ferrimagnetic behaviour of Heusler compounds with complete spin polarization. *J. Phys. Condens. Matter* **18,** 6171–6181 (2006).

27. Balke, B., Fecher, G. H., Winterlik, J. & Felser, C. Mn3Ga, a compensated ferrimagnet with high Curie temperature and low magnetic moment for spin torque transfer applications. *Appl. Phys. Lett.* **90,** 152504 (2007).

28. Tsunashima, S. Magneto-optical recording. *J. Phys. D. Appl. Phys.* **34,** R87–R102 (2001).

29. Chen, E. *et al.* Advances and future prospects of spin-transfer torque random access memory. in *IEEE Transactions on Magnetics* **46,** 1873–1878 (2010).

30. Nakayama, M. *et al.* Spin transfer switching in TbCoFe∕CoFeB∕MgO∕CoFeB∕TbCoFe magnetic tunnel junctions with perpendicular magnetic anisotropy. *J. Appl. Phys.* **103,** 07A710 (2008).

31. Leamy, H. J. & Dirks, A. G. Microstructure and magnetism in amorphous rare-earth-transition-metal thin films. II. Magnetic anisotropy. *J. Appl. Phys.* **49,** 3430 (1978).

32. Takeno, Y., Kaneko, K. & Goto, K. Magnetic properties of amorphous (Tb1-xGdx)30Fe70 thin films. *Jpn. J. Appl. Phys.* **30,** 1701–1704 (1991).

33. Coey, J. M. D., Chappert, J., Rebouillat, J. P. & Wang, T. S. Magnetic structure of an amorphous rare-earth transition-metal alloy. *Phys. Rev. Lett.* **36,** 1061–1064 (1976).

34. Harris, V. G., Aylesworth, K. D., Das, B. N., Elam, W. T. & Koon, N. C. Structural origins of magnetic anisotropy in sputtered amorphous Tb-Fe films. *Phys. Rev. Lett.* **69,** 1939–1942 (1992).

35. Harris, V. G. & Pokhil, T. Selective-Resputtering-Induced Perpendicular Magnetic Anisotropy in Amorphous TbFe Films. *Phys. Rev. Lett.* **87,** 67207 (2001).

36. Meiklejohn, W. H. & Bean, C. P. New magnetic anisotropy. *Phys. Rev.* **102,** 1413–1414 (1956).

37. Nogués, J. *et al.* Exchange bias in nanostructures. *Physics Reports* **422,** 65–117 (2005).

38. Skumryev, V. *et al.* Beating the superparamagnetic limit with exchange bias. *Nature* **423,** 850–853 (2003).

39. Ali, M. *et al.* Antiferromagnetic layer thickness dependence of the IrMn/Co exchange-bias system. *Phys. Rev. B* **68,** 214420 (2003).

40. Malozemoff, A. P. Random-field model of exchange anisotropy at rough ferromagnetic-antiferromagnetic interfaces. *Phys. Rev. B* **35,** 3679–3682 (1987).

41. Offi, F. *et al.* Induced Fe and Mn magnetic moments in Co-FeMn bilayers on Cu (001). *Phys. Rev. B* **67,** 94419 (2003).

42. Ohldag, H., Shi, H., Arenholz, E., Stöhr, J. & Lederman, D. Parallel versus Antiparallel Interfacial Coupling in Exchange Biased Co = FeF 2. *Physical Review Letters* **96,** 27203 (2006).

43. Fitzsimmons, M. R. *et al.* Pinned magnetization in the antiferromagnet and ferromagnet of an exchange bias system. *Phys. Rev. B* **75,** 214412 (2007).

44. Webb, D. J., Marshall, A. F., Toxen, A. M., Geballe, T. H. & White, R. M. Observation of giant exchange anisotropy. *IEEE Trans. Magn.* **24,** 2013–2015 (1988).

45. Romer, S. *et al.* Temperature dependence of large exchange-bias in TbFe-Co/Pt. *Appl. Phys. Lett.* **101,** 222404 (2012).

46. Yang, D. Z. *et al.* Positive exchange biasing in GdFe/NiCoO bilayers with antiferromagnetic coupling. *Phys. Rev. B* **71,** 144417 (2005).

47. Mangin, S., Montaigne, F. & Schuhl, A. Interface domain wall and exchange bias phenomena in ferrimagnetic/ferrimagnetic bilayers. *Phys. Rev. B* **68,** 140404 (2003).

48. Nayak, A. K. *et al.* Design of compensated ferrimagnetic Heusler alloys for giant tunable exchange bias. *Nat. Mater.* **14,** 679–684 (2015).

49. Machavarapu, R. & Jakob, G. Exchange bias effect in the martensitic state of Ni-Co-Mn-Sn film. *Appl. Phys. Lett.* **102,** 232406 (2013).

50. Teichert, N. *et al.* Exchange bias effect in martensitic epitaxial Ni-Mn-Sn thin films applied to pin CoFeB/MgO/CoFeB magnetic tunnel junctions. *Appl. Phys. Lett.* **106,** 192401 (2015).

51. Zeng, H., Li, J., Liu, J. P., Wang, Z. L. & Sun, S. Exchange-coupled nanocomposite magnets by nanoparticle self-assembly. *Nature* **420,** 395–398 (2002).

52. Ohkoshi, M., Tamari, K., Harada, M., Honda, S. & Kusuda, T. Microstructure and exchange-anisotropy of Co-CoO Films With Perpendicular Magnetization. *IEEE Transl. J. Magn. Japan* **1,** 37–38 (1985).

53. Dieny, B. *et al.* Giant magnetoresistive in soft ferromagnetic multilayers. *Phys. Rev. B* **43,** 1297–1300 (1991).

54. Hauet, T., Mangin, S., McCord, J., Montaigne, F. & Fullerton, E. E. Exchange-bias training effect in TbFe / GdFe: Micromagnetic mechanism. *Phys. Rev. B* **76,** 144423 (2007).

55. Radu, F., Abrudan, R., Radu, I., Schmitz, D. & Zabel, H. Perpendicular exchange bias in ferrimagnetic spin valves. *Nat. Commun.* **3,** 715 (2012).

56. Kirilyuk, A., Kimel, A. V. & Rasing, T. Ultrafast optical manipulation of magnetic order. *Rev. Mod. Phys.* **82,** 2731–2784 (2010).

57. Stöhr, J. & Siegmann, H. C. *Magnetism: From fundamentals to nanoscale dynamics*. *Magnetism: From Fundamentals to Nanoscale Dynamics* **152,** (Springer Berlin Heidelberg, 2006).

58. Lin, Z., Zhigilei, L. V. & Celli, V. Electron-phonon coupling and electron heat capacity of metals under conditions of strong electron-phonon nonequilibrium. *Phys. Rev. B* **77,** 75133 (2008).

59. Wu, C. Computational investigation of short pulse laser-induced modification of surface microstructure and photoacoustic control of surface diffusion. (University of Virginia, 2013).

60. Hohlfeld, J. *et al.* Electron and lattice dynamics following optical excitation of metals. *Chem. Phys.* **251,** 237–258 (2000).

61. Vaterlaus, A., Beutler, T. & Meier, F. Spin-lattice relaxation time of ferromagnetic gadolinium determined with time-resolved spin-polarized photoemission. *Phys. Rev. Lett.* **67,** 3314–3317 (1991).

62. Carpene, E. *et al.* Dynamics of electron-magnon interaction and ultrafast demagnetization in thin iron films. *Phys. Rev. B* **78,** 174422 (2008).

63. Scholl, A., Baumgarten, L., Jacquemin, R. & Eberhardt, W. Ultrafast Spin Dynamics of Ferromagnetic Thin Films Observed by fs Spin-Resolved Two-Photon Photoemission. *Phys. Rev. Lett.* **79,** 5146–5149 (1997).

64. Stamm, C. *et al.* Femtosecond modification of electron localization and transfer of angular momentum in nickel. *Nat. Mater.* **6,** 740–3 (2007).

65. Wietstruk, M. *et al.* Hot-electron-driven enhancement of spin-lattice coupling in Gd and Tb 4f ferromagnets observed by femtosecond x-ray magnetic circular dichroism. *Phys. Rev. Lett.* **106,** 127401 (2011).

66. Koopmans, B. *et al.* Explaining the paradoxical diversity of ultrafast laser-induced demagnetization. *Nat. Mater.* **9,** 259–265 (2010).

67. Stanciu, C. D. *et al.* All-optical magnetic recording with circularly polarized light. *Phys. Rev. Lett.* **99,** 47601 (2007).

68. Kimel, A. V. All-optical switching: Three rules of design. *Nat. Mater.* **13,** 225–6 (2014).

69. Lambert, C.-H. *et al.* All-optical control of ferromagnetic thin films and nanostructures. *Science (80-.).* **345,** 1337–40 (2014).

70. Sproul, W. D., Rudnik, P. J., Graham, M. E. & Rohde, S. L. High rate reactive sputtering in an opposed cathode closed-field unbalanced magnetron sputtering system. *Surf. Coatings Technol.* **43–44,** 270–278 (1990).

71. Kelly, P. J. & Arnell, R. D. Magnetron sputtering: a review of recent developments and applications. *Vacuum* **56,** 159–172 (2000).

72. Daillant, Jean, Gibaud, A. *X-Ray and Neutron reflection: principles and applications*. (Springer-Verlag Berlin Heidelberg, 1999). doi:10.1007/978-3-540-88588-7

73. Nag, S. *et al.* Phase separation in immiscible silver-copper alloy thin films. *J. Mater. Sci.* **44,** 3393–3401 (2009).

74. Devaraj, A. *et al.* Nanoscale phase separation in epitaxial Cr-Mo and Cr-V alloy thin films studied using atom probe tomography: Comparison of experiments and simulation. *J.*

Appl. Phys. **116,** 193512 (2014).

75. Puthucode, A. *et al.* De-vitrification of nanoscale phase-separated amorphous thin films in the immiscible copper–niobium system. *Philos. Mag.* **94,** 1622–1641 (2014).

76. Kuchibhatla, S. V. N. T. *et al.* Three-dimensional chemical imaging of embedded nanoparticles using atom probe tomography. *Nanotechnology* **23,** 215704 (2012).

77. Foner, S. Versatile and sensitive vibrating-sample magnetometer. *Rev. Sci. Instrum.* **30,** 548–557 (1959).

78. Cullity, B. D. & Graham, C. D. *Introduction to Magnetic Materials (2nd Edition)*. *Materials Today* **12,** (IEEE Press and John Wiley & Sons, Inc. Hoboken, New Jersey, 2009).

79. Ising, E. Beitrag zur theorie des ferromagnetismus. *Zeitschrift für Phys. A Hadron. Nucl.* **31,** 253–258 (1925).

80. Evans, R. F. L. *et al.* Atomistic spin model simulations of magnetic nanomaterials. *J. Phys. Condens. Matter* **26,** 103202 (2014).

81. Metropolis, N., Rosenbluth, A. W., Rosenbluth, M. N., Teller, A. H. & Teller, E. Equation of State by Fast Computing Machines. *J. Chem. Phys.* **21,** 1087–1092 (1953).

82. Earl, D. J. & Deem, M. W. Parallel Tempering: Theory, Applications, and New Perspectives. *Phys. Chem. Chem. Phys.* **7,** 3910–3916 (2005).

83. Kone, A. & Kofke, D. A. Selection of temperature intervals for parallel-tempering simulations. *J. Chem. Phys.* **122,** 206101 (2005).

84. Gilbert, T. L. A phenomenological theory of damping in ferromagnetic materials. *IEEE Trans. Magn.* **40,** 3443–3449 (2004).

85. Brown, W. F. Thermal Fluctuations of Fine Ferromagnetic Particles. *IEEE Trans. Magn.* **15,** 1196–1208 (1979).

86. Grinstein, G. & Koch, R. H. Coarse graining in micromagnetics. *Phys. Rev. Lett.* **90,** 207201 (2003).

87. Garanin, D. A. Fokker-Planck and Landau-Lifshitz-Bloch Equations for Classical

Ferromagnets. *Phys. Rev. B* **55,** 9 (1997).

88. Evans, R. F. L. *et al.* Stochastic form of the Landau-Lifshitz-Bloch equation. *Phys. Rev. B* **85,** 14433 (2012).

89. Press, W. H., Teukolsky, S. A., Vetterling, W. T. & Flannery, B. P. *Numerical Recipes 3rd Edition: The Art of Scientific Computing*. *Cambridge University Press. Cambridge, NY* (Cambrige University Press, 2007).

90. Marsaglia, G. & Tsang, W. W. The Ziggurat Method for Generating Random Variables. *J. Stat. Softw.* **5,** 1–7 (2000).

91. Cooley, J. W. & Tukey, J. W. An Algorithm for Machine Calculation of Complex Fourier Series. *Math. Comput.* **19,** 297–301 (1965).

92. Hayashi, N., Saito, K. & Nakatani, Y. Calculation of Demagnetizing Field Distribution Based on Fast Fourier Transform of Convolution. *Jpn. J. Appl. Phys.* **35,** 6065–6073 (1996).

93. Ostler, T. A. *et al.* Crystallographically amorphous ferrimagnetic alloys: Comparing a localized atomistic spin model with experiments. *Phys. Rev. B* **84,** 24407 (2011).

94. Radu, I. *et al.* Transient ferromagnetic-like state mediating ultrafast reversal of antiferromagnetically coupled spins. *Nature* **472,** 205–208 (2011).

95. Barker, J. *et al.* Two-magnon bound state causes ultrafast thermally induced magnetisation switching. *Sci. Rep.* **3,** 3262 (2013).

96. Ostler, T. A. Computer Simulations of Ultrafast Magnetisation Reversal. 160 (2012).

97. Tanaka, F., Tanaka, S. & Imamura, N. Magneto-optical recording characteristics of TbFeCo media by magnetic field modulation method. *Jpn. J. Appl. Phys.* **26,** 231–235 (1987).

98. Stanciu, C. D. *et al.* Ultrafast spin dynamics across compensation points in ferrimagnetic GdFeCo: The role of angular momentum compensation. *Phys. Rev. B* **73,** 220402 (2006).

99. Hebler, B., Hassdenteufel, A., Reinhardt, P., Karl, H. & Albrecht, M. Ferrimagnetic Tb-Fe Alloy Thin Films: Composition and Thickness Dependence of Magnetic Properties and All-Optical Switching. *Front. Mater.* **3,** 8 (2016).

100. Anuniwat, N., Ding, M., Poon, S. J., Wolf, S. A. & Lu, J. Strain-induced enhancement of coercivity in amorphous TbFeCo films. *J. Appl. Phys.* **113,** 43905 (2013).

101. Dirks, A. G. & Leamy, H. J. Columnar microstructure in vapor-deposited thin films. *Thin Solid Films* **47,** 219–233 (1977).

102. Thornton, J. A. The microstructure of sputter-deposited coatings. *Journal of Vacuum Science & Technology A: Vacuum, Surfaces, and Films* **4,** 3059 (1986).

103. Li, W., Yan, X., Aberle, A. G. & Venkataraj, S. Effect of deposition pressure on the properties of magnetron-sputter-deposited molybdenum back contacts for CIGS solar cells. in *Japanese Journal of Applied Physics* **54,** 08KC14 (IOP Publishing, 2015).

104. Zhong, L., Wang, J., Sheng, H., Zhang, Z. & Mao, S. X. Formation of monatomic metallic glasses through ultrafast liquid quenching. *Nature* **512,** 177–80 (2014).

105. Desmond, K. W. & Weeks, E. R. Random close packing of disks and spheres in confined geometries. *Phys. Rev. E* **80,** 51305 (2009).

106. Desmond, K. W. & Weeks, E. R. Influence of particle size distribution on random close packing of spheres. *Phys. Rev. E* **90,** 22204 (2014).

107. Lage, E. *et al.* Exchange biasing of magnetoelectric composites. *Nat. Mater.* **11,** 523–529 (2012).

108. Kools, J. C. S. Exchange-biased spin-valves for magnetic storage. *IEEE Trans. Magn.* **32,** 3165–3184 (1996).

109. Gider, S., Runge, B.-U., Marley, A. C. & Parkin, S. S. P. The Magnetic Stability of Spin-Dependent Tunneling Devices. *Science (80-.).* **281,** 797–799 (1998).

110. Kuch, W. *et al.* Tuning the magnetic coupling across ultrathin antiferromagnetic films by controlling atomic-scale roughness. *Nat. Mater.* **5,** 128–133 (2006).

111. Ziese, M. *et al.* Size and shape dependence of the exchange-bias field in exchange-coupled ferrimagnetic bilayers. *Eur. Phys. J. B* **45,** 223–230 (2005).

112. Estrader, M. *et al.* Robust antiferromagnetic coupling in hard-soft bi-magnetic core/shell nanoparticles. *Nat. Commun.* **4,** 2960 (2013).

113. Khan, M., Dubenko, I., Stadler, S. & Ali, N. Exchange bias behavior in Ni-Mn-Sb Heusler alloys. *Appl. Phys. Lett.* **91,** 72510 (2007).

114. Hopkins, P. E., Ding, M. & Poon, J. Contributions of electron and phonon transport to the thermal conductivity of GdFeCo and TbFeCo amorphous rare-earth transition-metal alloys. *J. Appl. Phys.* **111,** 103533 (2012).

115. Li, X. *et al.* Exchange bias and bistable magneto-resistance states in amorphous TbFeCo thin films. *Appl. Phys. Lett.* **108,** 1–6 (2016).

116. Malmhäll, R. Extraordinary Hall resistivity in amorphous terbium–iron thin films and its temperature dependence. *J. Appl. Phys.* **54,** 5128 (1983).

117. Cheng, X. M. *et al.* Antisymmetric magnetoresistance in magnetic multilayers with perpendicular anisotropy. *Phys. Rev. Lett.* **94,** 17203 (2005).

118. Granovsky, A. B., Vedyayev, A. V. & Brouers, F. Extraordinary Hall effect (EHE) of ferromagnetic composites in the effective medium approximation. *J. Magn. Magn. Mater.* **136,** 229–232 (1994).

119. Miltényi, P. *et al.* Tuning exchange bias. *Appl. Phys. Lett.* **75,** 2304–2306 (1999).

120. Nogués, J., Leighton, C. & Schuller, I. K. Correlation between antiferromagnetic interface coupling and positive exchange bias. *Physical Review B* **61,** 1315–1317 (2000).

121. Bezerra-Neto, M. M. *et al.* Complex magnetic structure of clusters and chains of Ni and Fe on Pt(111). *Sci. Rep.* **3,** 3054 (2013).

122. Ma, C. T., Li, X. & Poon, S. J. Micromagnetic simulation of ferrimagnetic TbFeCo films with exchange coupled nanophases. *J. Magn. Magn. Mater.* **417,** 197–202 (2016).

123. Gattass, R. R. & Mazur, E. Femtosecond laser micromachining in transparent materials. *Nat. Photonics* **2,** 219–225 (2008).

124. Chen, J. K. & Beraun, J. E. Numerical study of ultrashort laser pulse interactions with metal films. *Numer. Heat Transf. Part A Appl.* **40,** 1–20 (2001).

125. Chen, J. K., Tzou, D. Y. & Beraun, J. E. A semiclassical two-temperature model for ultrafast laser heating. *Int. J. Heat Mass Transf.* **49,** 307–316 (2006).

126. Agranat, M. B., Ashitkov, S. I., Granovskii, A. B. & Rukman, G. I. Interaction Between Picosecond Laser Pulses and the Electron, Spin and Phonon Subsystems of Nickel. *Zh. Eksp. Teor. Fiz.* **86,** 1376–1379 (1984).

127. You, L., Kato, T., Tsunashima, S. & Iwata, S. Dynamic heating in micron- and submicron-patterned TbFe films. *Jpn. J. Appl. Phys.* **47,** 146–149 (2008).

128. Majchrzak, E. & Dziatkiewicz, J. Analysis of ultrashort laser pulse interactions with metal films using a two-temperature model. *J. Appl. Math. Comput. Mech.* **14,** 31–39 (2015).

129. Kim, J.-W., Lee, K.-D., Jeong, J.-W. & Shin, S.-C. Ultrafast spin demagnetization by nonthermal electrons of TbFe alloy film. *Appl. Phys. Lett.* **94,** 192506 (2009).

APPENDIX A. The Reversibility of the Monte Carlo Algorithms

The reversibility of the Monte Carlo methods can be understood by a detailed balance condition. Given that the time series of spin configurations is a Markov chain, the master equation can be written as follows.

$$P_{k+1}(\alpha) = P_k(\alpha) + \sum_{\alpha'} \big(\mathcal{T}(\alpha' \to \alpha) P_k(\alpha') - \mathcal{T}(\alpha \to \alpha') P_k(\alpha)\big) \qquad \text{(A.1)}$$

Where α and α' are arbitrary configurations, $P_k(\alpha)$ represents the probability for the configuration α at the kth step and $\mathcal{T}(\alpha' \to \alpha)$ indicates the probability of transition from α' to α. The first term on the right hand site is the contribution of the case when no transition happens at the kth step. The second term describes the contribution of transitions from any α' to α. The third term counts for transition from α to any α' out. As $k \to +\infty$, the series of configurations is converging to the thermodynamic equilibrium. In the classical problem, it follows the Boltzmann distribution.

$$P_k(\alpha) \to P_{eq}(\alpha) = Z^{-1} \exp\left(-\frac{\mathcal{H}(\alpha)}{k_B T}\right), \quad k \to +\infty \qquad \text{(A.2)}$$

Then, Equation A.1 can be arranged to the following form, also known as the detailed balance condition

$$\frac{\mathcal{T}(\alpha \to \alpha')}{\mathcal{T}(\alpha' \to \alpha)} = \exp\left(-\frac{1}{k_B T}\big(\mathcal{H}(\alpha') - \mathcal{H}(\alpha)\big)\right) \qquad \text{(A.3)}$$

The Monte Carlo Metropolis sampling may have a transition probability as

$$\mathcal{T}(\alpha \to \alpha') = \begin{cases} 1, & if\ \mathcal{H}(\alpha') \le \mathcal{H}(\alpha) \\ \exp\left(-\frac{1}{k_B T}\big(\mathcal{H}(\alpha') - \mathcal{H}(\alpha)\big)\right), & if\ \mathcal{H}(\alpha') > \mathcal{H}(\alpha) \end{cases} \qquad \text{(A.4)}$$

It is easy to derive Equation 4.15 from Equation A.4.

For the parallel tempering algorithm, the configurations are swapped between different temperatures with the temperature-dependent transition probability. The temperature-dependent detailed balance condition can be derived from the same master equation A.1.

$$\frac{\mathcal{T}(\{\alpha,T\} \to \{\alpha,T'\})}{\mathcal{T}(\{\alpha,T'\} \to \{\alpha,T\})} = \exp\left(-\frac{\mathcal{H}(\alpha)}{k_B}\left(\frac{1}{T'}-\frac{1}{T}\right)\right) \tag{A.5}$$

Then the swapping probability $\mathcal{T}(\{\alpha,T;\alpha',T'\} \to \{\alpha,T';\alpha',T\})$ should has the relation

$$\begin{aligned}&\frac{\mathcal{T}(\{\alpha,T;\alpha',T'\} \to \{\alpha,T';\alpha',T\})}{\mathcal{T}(\{\alpha,T';\alpha',T\} \to \{\alpha,T;\alpha',T'\})}\\ &\qquad = \frac{\mathcal{T}(\{\alpha,T\} \to \{\alpha,T'\})}{\mathcal{T}(\{\alpha,T'\} \to \{\alpha,T\})} \cdot \frac{\mathcal{T}(\{\alpha',T'\} \to \{\alpha',T\})}{\mathcal{T}(\{\alpha',T\} \to \{\alpha',T'\})}\\ &\qquad = \exp\left(\frac{1}{k_B}\big(\mathcal{H}(\alpha')-\mathcal{H}(\alpha)\big)\left(\frac{1}{T'}-\frac{1}{T}\right)\right)\end{aligned} \tag{A.6}$$

Thus, the swapping probability can be proposed as

$$\begin{aligned}&\mathcal{T}(\{\alpha,T;\alpha',T'\} \to \{\alpha,T';\alpha',T\})\\ &= \begin{cases} 1, & if\ \big(\mathcal{H}(\alpha')-\mathcal{H}(\alpha)\big)\left(\frac{1}{T'}-\frac{1}{T}\right) \geq 0 \\ \exp\left(\frac{1}{k_B}\big(\mathcal{H}(\alpha')-\mathcal{H}(\alpha)\big)\left(\frac{1}{T'}-\frac{1}{T}\right)\right), & if\ \big(\mathcal{H}(\alpha')-\mathcal{H}(\alpha)\big)\left(\frac{1}{T'}-\frac{1}{T}\right) < 0 \end{cases}\end{aligned} \tag{A.7}$$

It is easy to verify Equation A.7 is consistent with Equation 4.18.

APPENDIX B. The Fokker-Planck Equation of the Stochastic Atomistic LLG Equation

The stochastic Atomistic LLG equation of a multi-spin system can be expressed as

$$\frac{d\boldsymbol{S}^i}{dt} = -\frac{\mu_0\gamma_i}{1+\alpha_i^2}\boldsymbol{S}^i \times \left(\boldsymbol{H}^i_{eff0} + \boldsymbol{\xi}^i\right) - \frac{\alpha_i\mu_0\gamma_i}{1+\alpha_i^2}\boldsymbol{S}^i \times \left(\boldsymbol{S}^i \times \left(\boldsymbol{H}^i_{eff0} + \boldsymbol{\xi}^i\right)\right) \qquad \text{(B.1)}$$

Where the random fluctuation field satisfies

$$\langle \xi^i_\mu(t) \rangle = 0 \qquad \text{(B.2)}$$

$$\langle \xi^i_\mu(t)\xi^j_\nu(t') \rangle = 2\kappa_i\delta_{ij}\delta_{\mu\nu}\delta(t-t') \qquad \text{(B.3)}$$

Equation B.1 can be rearranged into the following form.

$$\frac{dS^i_\mu}{dt} = f^i_\mu + g^i_{\mu\lambda}\xi_\lambda \qquad \text{(B.4)}$$

$$f^i_\mu = -\frac{\mu_0\gamma_i}{1+\alpha_i^2}\left(\epsilon_{\mu\nu\lambda}S^i_\nu H^i_{eff0,\lambda} + \alpha_i\epsilon_{\mu\nu\lambda}\epsilon_{\lambda\rho\sigma}S^i_\nu S^i_\rho H^i_{eff0,\sigma}\right) \qquad \text{(B.5)}$$

$$g^i_{\mu\lambda} = -\frac{\mu_0\gamma_i}{1+\alpha_i^2}\left(\epsilon_{\mu\nu\lambda}S^i_\nu + \alpha_i S^i_\mu S^i_\lambda - \alpha_i\delta_{\lambda\mu}\right) \qquad \text{(B.6)}$$

The Fokker-Planck equation for Equation B.4 can be derived based on the Stratonovich integration.

$$\frac{\partial P(\boldsymbol{S}^i,t)}{\partial t} = -\sum_i \left(\frac{\partial}{\partial S^i_\alpha}\left(f^i_\alpha P(\boldsymbol{S}^i,t)\right) - \kappa_i \frac{\partial}{\partial S^i_\alpha}\left(g^i_{\alpha\beta}\frac{\partial}{\partial S^i_\alpha}\left(g^i_{\sigma\beta}P(\boldsymbol{S}^i,t)\right)\right)\right) \qquad \text{(B.7)}$$

Where $P(\boldsymbol{S}^i,t)$ is the probability density. Express the above equation into the following vector form.

$$\frac{\partial}{\partial t}P = \sum_i \frac{\mu_0\gamma_i}{1+\alpha_i^2}\frac{\partial}{\partial \boldsymbol{S}^i}\left(\left(\boldsymbol{S}^i \times \boldsymbol{H}_{eff0}^i + \alpha_i \boldsymbol{S}^i \times \left(\boldsymbol{S}^i \times \boldsymbol{H}_{eff0}^i\right) - \mu_0\gamma_i\kappa_i\boldsymbol{S}^i \times \left(\boldsymbol{S}^i \times \frac{\partial}{\partial \boldsymbol{S}^i}\right)\right)P\right) \tag{B.8}$$

Where the effective field is defined as $\boldsymbol{H}_{eff0}^i \equiv -\frac{1}{\mu_0\mu_i}\frac{\partial \mathcal{H}}{\partial \boldsymbol{S}^i}$. Consider the thermodynamic equilibrium state by the Boltzmann distribution.

$$P_{eq} = Z^{-1}\exp\left(-\frac{\mathcal{H}}{k_BT}\right) \tag{B.9}$$

Then, the differentiation of the probability density to spin can be calculated as

$$\frac{\partial}{\partial \boldsymbol{S}^i}P_{eq} = \frac{\mu_0\mu_i}{k_BT}P_{eq}\boldsymbol{H}_{eff0}^i \tag{B.10}$$

Substitute Equation B.10 back to Equation B.8, we can have a relation of κ_i as the following equation.

$$\kappa_i = \frac{\alpha_i k_BT}{\mu_0^2\gamma_i\mu_i} \tag{B.11}$$

Specifically, for modeling with a discrete integration scheme, the random field should be redefined as a time average of a stochastic integration of $\boldsymbol{\xi}^i$.

$$\tilde{\boldsymbol{\xi}}^i(t) \equiv \frac{1}{\Delta t}\int_t^{t+\Delta t} ds\boldsymbol{\xi}^i(s) \tag{B.12}$$

$$\langle\tilde{\xi}_\mu^i(t)\rangle = 0 \tag{B.13}$$

$$\langle\tilde{\xi}_\mu^i(t)\tilde{\xi}_\nu^j(t')\rangle = \frac{2\alpha_i k_BT}{\mu_0^2\gamma_i\mu_i\Delta t}\delta_{\mu\nu}\delta_{ij}\delta(t-t') \tag{B.14}$$

Equation B.14 indicates a relation between the random fluctuation field and the temperature, which is very important when simulating spin systems at a finite temperature.

APPENDIX C. Spin Distribution Assumption

To evaluate the transverse relaxation term in Equation 4.26, we need to make an additional assumption of spin distribution function $P(\boldsymbol{S})$ as shown in Equation 4.27. It is easy to verify that

$$\int d^3S\, P = 1 \tag{C.1}$$

Moreover, the spin polarization can be calculated in terms of the distribution parameter $\boldsymbol{w}$.

$$\begin{aligned}\boldsymbol{m} = \int d^3S\, P\boldsymbol{S} &= \frac{w}{4\pi \sinh w}\int_0^{2\pi} d\phi \int_{-1}^{1} d(\cos\theta)\exp(w\cos\theta)\begin{bmatrix}\cos\phi\sin\theta \\ \sin\phi\sin\theta \\ \cos\theta\end{bmatrix} \\ &= \begin{bmatrix}0 \\ 0 \\ \coth w - \dfrac{1}{w}\end{bmatrix} = B(w)\frac{\boldsymbol{w}}{w}\end{aligned} \tag{C.2}$$

Where $B(w)$ is the Langevin function. Now, let’s evaluate the second term on the right hand side of Equation 4.26.

$$\begin{aligned}\langle \boldsymbol{S}\times(\boldsymbol{S}\times\boldsymbol{H}_{eff})\rangle &= \int d^3S\, P\boldsymbol{S}\times(\boldsymbol{S}\times\boldsymbol{H}_{eff}) \\ &= \int d^3S\, P\left(\boldsymbol{S}(\boldsymbol{S}\cdot\boldsymbol{H}_{eff}) - \boldsymbol{H}_{eff}(\boldsymbol{S}\cdot\boldsymbol{S})\right) \\ &= \int d^3S\, P\boldsymbol{S}(\boldsymbol{S}\cdot\boldsymbol{H}_{eff}) - \boldsymbol{H}_{eff}\end{aligned} \tag{C.3}$$

Assume $\boldsymbol{H}_{eff} \equiv H_{eff}\begin{bmatrix}\cos\phi'\sin\theta' \\ \sin\phi'\sin\theta' \\ \cos\theta'\end{bmatrix}$,

$$
\begin{aligned}
&\int d^3S\, P\boldsymbol{S}\left(\boldsymbol{S}\cdot\boldsymbol{H}_{eff}\right) \\
&= \frac{w}{4\pi\sinh w}\int_0^{2\pi} d\phi \int_{-1}^{1} d\cos\theta\, \exp(w\cos\theta)\begin{bmatrix}\cos\phi\sin\theta\\ \sin\phi\sin\theta\\ \cos\theta\end{bmatrix} H_{eff}(\cos(\phi \\
&- \phi')\sin\theta\sin\theta' + \cos\theta\, cos\theta') \\
&= \frac{wH_{eff}}{4\pi\sinh w}\begin{bmatrix}\sin\theta'\int_0^{2\pi}\cos\phi\cos(\phi-\phi')\,d\phi\int_{-1}^{1}\exp(wt)\,(1-t^2)dt\\ \sin\theta'\int_0^{2\pi}\sin\phi\cos(\phi-\phi')\,d\phi\int_{-1}^{1}\exp(wt)\,(1-t^2)dt\\ \cos\theta'\int_0^{2\pi}d\phi\int_{-1}^{1}\exp(wt)\,t^2dt\end{bmatrix} \qquad \text{(C.4)} \\
&= H_{eff}\begin{bmatrix}\dfrac{\sin\theta'\cos\phi'\,B(w)}{w}\\ \dfrac{\sin\theta'\sin\phi'\,B(w)}{w}\\ \dfrac{\cos\theta\left(w-2B(w)\right)}{w}\end{bmatrix} = \frac{B(w)}{w}\boldsymbol{H}_{eff} + \left(1-\frac{3B(w)}{w}\right)\left(\boldsymbol{H}_{eff}\cdot\frac{\boldsymbol{w}}{w}\right)\frac{\boldsymbol{w}}{w}
\end{aligned}
$$

Finally, we can express the result in the parallel and perpendicular component in terms of $\boldsymbol{w}$.

$$
\begin{aligned}
\langle\boldsymbol{S}\times\left(\boldsymbol{S}\times\boldsymbol{H}_{eff}\right)\rangle &= \left(\frac{B(w)}{w}-1\right)\boldsymbol{H}_{eff} + \left(1-\frac{3B(w)}{w}\right)\left(\boldsymbol{H}_{eff}\cdot\frac{\boldsymbol{w}}{w}\right)\frac{\boldsymbol{w}}{w} \\
&= \left(\frac{B(w)}{w}-1\right)\left(\boldsymbol{H}_{eff}-\left(\boldsymbol{H}_{eff}\cdot\frac{\boldsymbol{w}}{w}\right)\frac{\boldsymbol{w}}{w}\right) \\
&- 2\frac{B(w)}{w}\left(\boldsymbol{H}_{eff}\cdot\frac{\boldsymbol{w}}{w}\right)\frac{\boldsymbol{w}}{w} \qquad \text{(C.5)} \\
&= \left(1-\frac{B(w)}{w}\right)\frac{\boldsymbol{w}}{w}\times\left(\frac{\boldsymbol{w}}{w}\times\boldsymbol{H}_{eff}\right) - 2\frac{B(w)}{w}\left(\boldsymbol{H}_{eff}\cdot\frac{\boldsymbol{w}}{w}\right)\frac{\boldsymbol{w}}{w}
\end{aligned}
$$

APPENDIX D. The Fokker-Planck Equation of a Multi-spin System

The Fokker-Planck equation of a multiple spin system is given by Equation B.7 or a rearranged version as

$$\frac{\partial P_{tot}(\{\boldsymbol{S}_i\},t)}{\partial t} = -\sum_i \frac{\partial}{\partial S_i^\alpha}\left[\left(f_i^\alpha - \kappa_i g_i^{\alpha\beta} g_i^{\sigma\beta}\frac{\partial}{\partial S_i^\sigma}\right)P_{tot}\right] \tag{D.1}$$

Integral on the both sides in terms of spin $\boldsymbol{S}_{i_0}$

$$\begin{aligned}\int \frac{\partial P_{tot}(\{\boldsymbol{S}_i\},\tau)}{\partial t} S_{i_0}^\gamma \prod_j d^3S_j \\ = \int -\sum_i \frac{\partial}{\partial S_i^\alpha}\left[\left(f_i^\alpha - \kappa_i g_i^{\alpha\beta} g_i^{\sigma\beta}\frac{\partial}{\partial S_i^\sigma}\right)P_{tot}\right] S_{i_0}^\gamma \prod_j d^3S_j\end{aligned} \tag{D.2}$$

As is shown, the new FPE is entangled in terms of different spins. To simplify the problem, we can introduce the mean field assumption, that is, $P_{tot}(\{\boldsymbol{S}_i\},t) = \prod_i P_i(\boldsymbol{S}_i,t)$, and for each spin the following equation is satisfied.

$$\frac{\partial P_i}{\partial \tau} = -\frac{\partial}{\partial S_i^\alpha}\left[\left(a_i^\alpha - \kappa_i b_i^{\alpha\beta} b_i^{\sigma\beta}\frac{\partial}{\partial S_i^\sigma}\right)P_i\right] \tag{D.3}$$

The left hand side is

$$\begin{aligned}\int \frac{\partial P_{tot}(\{\boldsymbol{S}_i\},t)}{\partial t} S_{i_0}^\gamma \prod_j d^3S_j \\ = \left(\prod_{j\neq i_0}\int P_j(\boldsymbol{S}_j,t)d^3S_j\right)\int \frac{\partial P_{i_0}(\boldsymbol{S}_{i_0},t)}{\partial t} S_{i_0}^\gamma d^3S_{i_0} \\ = \int \frac{\partial P_{i_0}(\boldsymbol{S}_{i_0},t)}{\partial t} S_{i_0}^\gamma d^3S_{i_0}\end{aligned} \tag{D.4}$$

The right hand side is

$$
\begin{aligned}
&\int -\sum_{i} \frac{\partial}{\partial S_i^\alpha}\left[\left(f_i^\alpha - \kappa_i g_i^{\alpha\beta} g_i^{\sigma\beta} \frac{\partial}{\partial S_i^\sigma}\right) P_{tot}\right] S_{i_0}^\gamma \prod_j d^3 S_j \\
&\qquad = \sum_{i \neq i_0} \Bigg(\int - \frac{\partial}{\partial S_i^\alpha} \Bigg[\Bigg(f_i^\alpha \\
&\qquad - \kappa_i g_i^{\alpha\beta} g_i^{\sigma\beta} \frac{\partial}{\partial S_i^\sigma} \Bigg) P_i \Bigg] d^3 S_i \Bigg) \left(\int S_{i_0}^\gamma P_{i_0} d^3 S_{i_0} \right) \left(\prod_{k \neq i, k \neq i_0} \int P_k d^3 S_k \right) \\
&\qquad + \left(\int - \frac{\partial}{\partial S_{i_0}^\alpha} \left[\left(f_{i_0}^\alpha - \kappa_{i_0} g_{i_0}^{\alpha\beta} g_{i_0}^{\sigma\beta} \frac{\partial}{\partial S_{i_0}^\sigma} \right) P_{i_0} \right] S_{i_0}^\gamma \, d^3 S_{i_0} \right) \left(\prod_{k \neq i_0} \int P_k d^3 S_k \right) \\
&\qquad = \sum_{i \neq i_0} \left(\int \frac{\partial P_i}{\partial t} d^3 S_i \right) m_{i_0}^\gamma + \int - \frac{\partial}{\partial S_{i_0}^\alpha} \left[\left(f_{i_0}^\alpha - \kappa_{i_0} g_{i_0}^{\alpha\beta} g_{i_0}^{\sigma\beta} \frac{\partial}{\partial S_{i_0}^\sigma} \right) P_{i_0} \right] S_{i_0}^\gamma \, d^3 S_{i_0} \\
&\qquad = \int - \frac{\partial}{\partial S_{i_0}^\alpha} \left[\left(f_{i_0}^\alpha - \kappa_{i_0} g_{i_0}^{\alpha\beta} g_{i_0}^{\sigma\beta} \frac{\partial}{\partial S_{i_0}^\sigma} \right) P_{i_0} \right] S_{i_0}^\gamma \, d^3 S_{i_0}
\end{aligned}
\tag{D.5}
$$

Finally,

$$
\int \frac{\partial P_{i_0}(\boldsymbol{S}_{i_0}, \tau)}{\partial t} S_{i_0}^\gamma d^3 S_{i_0} = \int - \frac{\partial}{\partial S_{i_0}^\alpha} \left[\left(f_{i_0}^\alpha - \kappa_{i_0} g_{i_0}^{\alpha\beta} g_{i_0}^{\sigma\beta} \frac{\partial}{\partial S_{i_0}^\sigma} \right) P_{i_0} \right] S_{i_0}^\gamma \, d^3 S_{i_0} \tag{D.6}
$$

This implies that with the mean field assumption, the Fokker-Planck equation of a multi-spin system can be simplified to the form of a single spin system.

APPENDIX E. Stochastic LLB Equation

As suggested by Evans et al[88], the stochastic LLB equation can be formulated by introducing Gaussian random field and Gaussian random torque as shown in Equation 4.37, 4.38 and 4.39. Now, define

$$a^i \overset{\text{def}}{=} -\frac{\gamma\mu_0}{1+\alpha^2}\epsilon_{ijk} m^j H_{eff}^{\prime,k} + b_\perp^{ij} H_{eff}^{\prime,j} + \frac{\gamma\mu_0}{1+\alpha^2}\frac{\alpha_\parallel}{m^2} m^i m^j H_{eff}^{\prime,j} \tag{E.1}$$

$$b_\perp^{ij} \overset{\text{def}}{=} -\frac{\gamma\mu_0}{1+\alpha^2}\frac{\alpha_\perp}{m^2}\left(m^i m^j - \delta_{ij} m^2\right) \tag{E.2}$$

$$b_\parallel^{ij} \overset{\text{def}}{=} \delta_{ij} \tag{E.3}$$

Therefore, the stochastic LLB equation can be simplified as

$$\frac{dm^i}{dt} = a^i + b_\alpha^{ij} \xi_\alpha^j \tag{E.4}$$

Define Gaussian white noise ζ_α^i, then

$$\frac{dm^i}{dt} = a^i + \sqrt{2\kappa_\perp} b_\perp^{ij} \zeta_\perp^j + \sqrt{2\kappa_\parallel} b_\parallel^{ij} \zeta_\parallel^j \tag{E.5}$$

Since Gaussian white noise is the formal derivative of a Wiener process, define Wiener process $W_\alpha^j(t)$, then

$$dm^i = a^i dt + \sqrt{2\kappa_\perp} b_\perp^{ij} dW_\perp^j + \sqrt{2\kappa_\parallel} b_\parallel^{ij} dW_\parallel^j \tag{E.6}$$

The $m^i(t)$ can be treated as a Stratonovich process

$$m^i(t) \equiv m^i(0) + \int_0^\tau a^i ds + \int_0^\tau \sqrt{2\kappa_\perp} b_\perp^{ij} \circ dW_\perp^j(s) + \int_0^\tau \sqrt{2\kappa_\parallel} b_\parallel^{ij} \circ dW_\parallel^j(s) \tag{E.7}$$

Its Fokker-Planck equation can be derived as

$$\frac{\partial P}{\partial t} = -\frac{\partial}{\partial m^i}\left(a^i P\right) + \frac{\partial}{\partial m^i}\left(\sqrt{\kappa_\perp} b_\perp^{ik} \frac{\partial}{\partial m^j}\left(\sqrt{\kappa_\perp} b_\perp^{jk} P\right)\right) + \frac{\partial}{\partial m^i}\left(\sqrt{\kappa_\parallel} b_\parallel^{ik} \frac{\partial}{\partial m^j}\left(\sqrt{\kappa_\parallel} b_\parallel^{jk} P\right)\right) \tag{E.8}$$

Based on the definition of a^i and b_α^{ij}, we can derive some useful equations.

$$\frac{\partial m}{\partial m^j} = \frac{m^j}{m} \tag{E.9}$$

$$b_\perp^{ik} b_\perp^{jk} = -\left(\frac{\gamma\mu_0}{1+\alpha^2}\right)^2 \frac{\alpha_\perp^2}{m^2}\left(m^i m^j - \delta_{ij} m^2\right) = \frac{\gamma\mu_0}{1+\alpha^2} \alpha_\perp b_\perp^{ij} \tag{E.10}$$

$$b_\perp^{ik} \frac{\partial}{\partial m^j}\left(f(m) b_\perp^{jk}\right) = 0 \tag{E.11}$$

$$[\boldsymbol{m} \times (\boldsymbol{m} \times \boldsymbol{v})]^i = -\frac{1+\alpha^2}{\gamma\mu_0} \frac{m^2}{\alpha_\perp} b_\perp^{ij} v^j \tag{E.12}$$

$$v^i = \frac{m^j v^j m^i}{m^2} + \frac{1+\alpha^2}{\gamma\mu_0} \frac{b_\perp^{ij} v^j}{\alpha_\perp} \tag{E.13}$$

Note that the last two equations provide the idea that $\boldsymbol{m}$, $\boldsymbol{m} \times \boldsymbol{v}$, and $\boldsymbol{m} \times (\boldsymbol{m} \times \boldsymbol{v})$ are orthogonal basis for an arbitrary vector $\boldsymbol{v}$ as long as $\boldsymbol{m} \nparallel \boldsymbol{v}$.

Assume the stationary solution of the stochastic LLB equation follows the classical Boltzmann distribution, the derivative of probability distribution has the property

$$\frac{\partial}{\partial m^j} P_{eq} = \beta\mu N H_{eff}^{\prime,j} P_{eq} \tag{E.14}$$

Substitute into the FPE

$$0 \equiv -\frac{\partial}{\partial m^i}\left(a^i P_{eq} - \sqrt{\kappa_\perp} b_\perp^{ik} \frac{\partial}{\partial m^j}\left(\sqrt{\kappa_\perp} b_\perp^{jk} P_{eq}\right) - \sqrt{\kappa_\parallel} b_\parallel^{ik} \frac{\partial}{\partial m^j}\left(\sqrt{\kappa_\parallel} b_\parallel^{jk} P_{eq}\right)\right) \tag{E.15}$$

The first term in the parenthesis

$$a^i P_{eq} = \left(-\frac{\gamma\mu_0}{1+\alpha^2}\epsilon_{ijk} m^j H_{eff}^{\prime,k} + b_\perp^{ij} H_{eff}^{\prime,j} + \frac{\gamma\mu_0}{1+\alpha^2}\frac{\alpha_\parallel}{m^2} m^i m^j H_{eff}^{\prime,j}\right) P_{eq} \tag{E.16}$$

The second term

$$-\sqrt{\kappa_\perp} b_\perp^{ik} \frac{\partial}{\partial m^j}\left(\sqrt{\kappa_\perp} b_\perp^{jk} P_{eq}\right) = -\kappa_\perp \beta\mu N \frac{\gamma\mu_0}{1+\alpha^2}\alpha_\perp b_\perp^{ij} H_{eff}^{\prime,j} P_{eq} \tag{E.17}$$

The third term

$$\begin{aligned} -\sqrt{\kappa_\parallel} b_\parallel^{ik} \frac{\partial}{\partial m^j}\left(\sqrt{\kappa_\parallel} b_\parallel^{jk} P_{eq}\right) &= -\kappa_\parallel \beta\mu N H_{eff}^{\prime,i} P_{eq} \\ &= -\kappa_\parallel \beta\mu N \left(\frac{m^j H_{eff}^{\prime,j} m^i}{m^2} + \frac{1+\alpha^2}{\gamma\mu_0}\frac{b_\perp^{ij} H_{eff}^{\prime,j}}{\alpha_\perp}\right) P_{eq} \end{aligned} \tag{E.18}$$

Collect terms based on the orthogonal basis, we have

$$\begin{aligned} &\left(\frac{\gamma\mu_0}{1+\alpha^2}\frac{\alpha_\parallel}{m^2} m^i m^j H_{eff}^{\prime,j} - \kappa_\parallel \beta\mu N \frac{m^j H_{eff}^{\prime,j} m^i}{m^2}\right) P_{eq} \\ &\quad - \left(\frac{\gamma\mu_0}{1+\alpha^2}\epsilon_{ijk} m^j H_{eff}^{\prime,k}\right) P_{eq} \\ &\quad + \left(b_\perp^{ij} H_{eff}^{\prime,j} - \kappa_\perp \beta\mu N \frac{\gamma\mu_0}{1+\alpha^2}\alpha_\perp b_\perp^{ij} H_{eff}^{\prime,j} \right. \\ &\quad \left. - \kappa_\parallel \beta\mu N \frac{1+\alpha^2}{\gamma\mu_0}\frac{b_\perp^{ij} H_{eff}^{\prime,j}}{\alpha_\perp}\right) P_{eq} \end{aligned} \tag{E.19}$$

Now, let the first and third terms be zero

$$\frac{\gamma\mu_0}{1+\alpha^2}\frac{\alpha_\parallel}{m^2} m^i m^j H_{eff}^{\prime,j} - \kappa_\parallel \beta\mu N \frac{m^j H_{eff}^{\prime,j} m^i}{m^2} = 0 \tag{E.20}$$

$$b_\perp^{ij} H_{eff}^{\prime,j} - \kappa_\perp \beta\mu N \frac{\gamma\mu_0}{1+\alpha^2}\alpha_\perp b_\perp^{ij} H_{eff}^{\prime,j} - \kappa_\parallel \beta\mu N \frac{1+\alpha^2}{\gamma\mu_0}\frac{b_\perp^{ij} H_{eff}^{\prime,j}}{\alpha_\perp} = 0 \tag{E.21}$$

It is easy to check that

$$0 \equiv \frac{\partial}{\partial m^i}\left(\left(\frac{\gamma\mu_0}{1+\alpha^2}\epsilon_{ijk}m^j H_{eff}^{\prime,k}\right)P_{eq}\right) \tag{E.22}$$

Finally, the fluctuation-dissipation theorem can be derived as

$$\kappa_\parallel = \frac{\gamma\mu_0}{1+\alpha^2}\frac{\alpha_\parallel}{\beta\mu N} \tag{E.23}$$

$$\kappa_\perp = \frac{1+\alpha^2}{\gamma\mu_0}\frac{\alpha_\perp - \alpha_\parallel}{\beta\mu N} \tag{E.24}$$

APPENDIX F. Random Number Generator Code

```
/* Ran.h                                                                   */
/* random number generator including both uniform and normal distributions */
/* Xiaopu Li (xl6ba@virginia.edu) Mar 10 2016                              */

// type preparations
#ifdef _MSC_VER
typedef __int64 Llong; // 64 bit integer
typedef unsigned __int64 Ullong;
#else
typedef long long int Llong; // 64 bit integer
typedef unsigned long long int Ullong;
#endif

// head begins
#ifndef RAN_H
#define RAN_H
#include <cmath>

struct Ran {
  Ullong u, v, w;
  unsigned int kn[128];
  double wn[128], fn[128];

  // constructor sets the seed and creates the tables
  Ran(Ullong j) : v(4101842887655102017LL), w(1) {
    u = j ^ v; int64();
    v = u; int64();
    w = v; int64();


    const double m = 2147483648.0, vn = 9.91256303526217e-3;
    double dn = 3.442619855899, tn = dn, q = vn / std::exp(-0.5*dn*dn);
    kn[0] = (unsigned int)((dn / q) * m);
    kn[1] = 0;
    wn[0] = q / m;
    wn[127] = dn / m;
    fn[0] = 1.0;
    fn[127] = std::exp(-0.5*dn*dn);
    for (int i = 126; i >= 1; --i) {
      dn = std::sqrt(-2.0 * std::log(vn / dn + fn[i+1]));
      kn[i+1] = (unsigned int)((dn / tn) * m);
      tn = dn;
      fn[i] = std::exp(-0.5*dn*dn);
      wn[i] = dn / m;
    }

  }


/*******************************************************************************/
// Uniform distribution generator
// Based on Chapter 7, Numerical Recipes, the Art of Scientific Computing (3rd)

  inline Ullong int64() {
    u = u * 2862933555777941757LL + 7046029254386353087LL;
    v ^= v >> 17; v ^= v << 31; v ^= v >> 8;
```

```
    w = 4294957665U*(w & 0xffffffff) + (w >> 32);
    Ullong x = u ^ (u << 21); x ^= x >> 35; x ^= x << 4;
    return (x + v) ^ w;
  }
  inline double doub() { return 5.42101086242752217E-20 * int64(); }
  inline unsigned int int32() { return (unsigned int)int64(); }
/********************************************************************************/



/********************************************************************************/
// Ziggurat standard normal distribution generator
// Based on "Marsaglia G and Tsang W-W 2000 J. Stat. Softw. 5 1-7"
  inline double norm() {
    int h = int32();
    int i = h & 127;
    unsigned int absh = unsigned((h>0)? h : -h);
    return (absh < kn[i])? h*wn[i] : fix(h, i);
  }


  inline double fix(int h, int i) {
    const double r = 3.442619855899;
    // case 1: return an x from the tail
    if (i == 0) {
      double x, y;
      do {
    x = -std::log(doub()) * 0.2904765161;
    y = -std::log(doub());
      }
      while(y + y < x * x);
      return (h > 0) ? r+x : -r-x;
    }
    // case 2: reject if it is not in the desired area, redo norm() again
    double x = h*wn[i];
    if (fn[i] + doub() * (fn[i-1] - fn[i]) < exp(-0.5*x*x)) return x;
    else return norm();
  }
/********************************************************************************/
};


#endif
// head ends
```

APPENDIX G. Demagnetizing Field with Free Boundary Conditions

For the case with one or more free boundaries, the padding-zero technique[92] has to be used to ease the inconvenience. For example, the demagnetizing field is given in the following equation with periodic boundaries along x and y axes but a free boundary along z axis.

$$h_{D,l,m,n}^{\alpha} = \sum_{i=-\infty}^{+\infty} \sum_{j=-\infty}^{+\infty} \sum_{k=0}^{n_z} \mu_{i,j,k} K_{l-i,m-j,n-k}^{\alpha\beta} S_{i,j,k}^{\beta} \tag{G.1}$$

A periodic demagnetizing tensor is defined as:

$$\widetilde{K}_{i,j,k} \equiv \begin{cases} \displaystyle\sum_{\lambda_x=-\infty}^{+\infty} \sum_{\lambda_y=-\infty}^{+\infty} K_{i+\lambda_x n_x, j+\lambda_y n_y, k}, & when\ k = 0, \ldots, n_z - 1 \\ 0, & when\ k = n_z \\ \displaystyle\sum_{\lambda_x=-\infty}^{+\infty} \sum_{\lambda_y=-\infty}^{+\infty} K_{i+\lambda_x n_x, j+\lambda_y n_y, k-2n_z}, & when\ k = n_z + 1, \ldots, 2n_z - 1 \end{cases} \tag{G.2}$$

And it is easy to verify the periodicity as:

$$\widetilde{K}_{i,j,k} = \widetilde{K}_{i+n_x, j+n_y, k+2n_z} \tag{G.3}$$

An extended periodic lattice is defined with padding zeros as:

$$\widetilde{\boldsymbol{\mathcal{M}}}_{i,j,k} \equiv \begin{cases} \boldsymbol{\mathcal{M}}_{i,j,k} \equiv \mu_{i,j,k} \boldsymbol{S}_{i,j,k}, & when\ k = 0, \ldots, n_z - 1 \\ 0, & when\ k = n_z, \ldots, 2n_z - 1 \end{cases} \tag{G.4}$$

This lattice satisfies a similar periodic relation as:

$$\widetilde{\boldsymbol{\mathcal{M}}}_{i,j,k} = \widetilde{\boldsymbol{\mathcal{M}}}_{i+n_x, j+n_y, k+2n_z} \tag{G.5}$$

Thus, the extended demagnetizing field is calculated in the following equation.

$$\tilde{h}_{D,l,m,n}^{\alpha} = \sum_{i=0}^{n_x-1} \sum_{j=0}^{n_y-1} \sum_{k=0}^{2n_z-1} \widetilde{K}_{l-i,m-j,n-k}^{\alpha\beta} \widetilde{\mathcal{M}}_{i,j,k}^{\beta} \tag{G.6}$$

The x and y components is then ignored for simplicity. The demagnetizing field is rearranged into the form of the following equation, for $n = 0, 1, \dots, n_z - 1$.

$$\begin{aligned}
\tilde{h}^{\alpha}_{D,n} = \sum_{k=0}^{2n_z-1} \tilde{K}^{\alpha\beta}_{n-k} \tilde{\mathcal{M}}^{\beta}_{k} = \sum_{k=0}^{n_z-1} \tilde{K}^{\alpha\beta}_{n-k} \mathcal{M}^{\beta}_{k} &= \sum_{k=0}^{n} \tilde{K}^{\alpha\beta}_{n-k} \mathcal{M}^{\beta}_{k} + \sum_{k=n}^{n_z-1} \tilde{K}^{\alpha\beta}_{n-k} \mathcal{M}^{\beta}_{k} \\
&= \sum_{k=0}^{n} \tilde{K}^{\alpha\beta}_{n-k} \mathcal{M}^{\beta}_{k} + \sum_{k=n}^{n_z-1} \tilde{K}^{\alpha\beta}_{2n_z+n-k} \mathcal{M}^{\beta}_{k} \qquad \text{(G.7)} \\
&= \sum_{k=0}^{n} K^{\alpha\beta}_{n-k} \mathcal{M}^{\beta}_{k} + \sum_{k=n}^{n_z-1} K^{\alpha\beta}_{n-k} \mathcal{M}^{\beta}_{k} = \sum_{k=0}^{n_z-1} K^{\alpha\beta}_{n-k} \mathcal{M}^{\beta}_{k} = h^{\alpha}_{D,n}
\end{aligned}$$

Equation G.7 confirms the correctness of the zero padding technique. Therefore, the demagnetizing field can be calculated by a standard discrete Fourier transform (DFT) algorithm as:

$$\begin{gathered}
h^{\alpha}_{D,l,m,n} = \tilde{h}^{\alpha}_{D,l,m,n} = DFT^{-1}\left\{DFT\left\{\tilde{K}^{\alpha\beta}_{l,m,n}\right\} DFT\left\{\tilde{\mathcal{M}}^{\beta}_{l,m,n}\right\}\right\}, \\
for\; n = 0, \dots, n_z - 1
\end{gathered} \qquad \text{(G.8)}$$

APPENDIX H. Derivation of Semi-classical Two-Temperature Model

The probability density function is defined as:

$$dN \equiv f(\boldsymbol{x}, \boldsymbol{p}, t) d^3x d^3p \tag{H.1}$$

Where dN is the number of molecules that are located within the volume element d^3x centering at $\boldsymbol{x}$, and have a momentum within the momentum space element d^3p centering at $\boldsymbol{p}$ at a specific time t. If no collision allowed:

$$f(\boldsymbol{x}, \boldsymbol{p}, t) d^3x d^3p = f\left(\boldsymbol{x} + \frac{\boldsymbol{p}}{m}\Delta t, \boldsymbol{p} + \boldsymbol{F}\Delta t, t + \Delta t\right) d^3x d^3p \tag{H.2}$$

If collisions are allowed:

$$\begin{aligned} \left(\frac{\partial f}{\partial t}\right)_{coll} \Delta t d^3x d^3p \\ &= f\left(\boldsymbol{x} + \frac{\boldsymbol{p}}{m}\Delta t, \boldsymbol{p} + \boldsymbol{F}\Delta t, t + \Delta t\right) d^3x d^3p \\ &- f(\boldsymbol{x}, \boldsymbol{p}, t) d^3x d^3p \end{aligned} \tag{H.3}$$

The collision frequency is given by a limit over an infinitesimal time interval:

$$\begin{aligned} \left(\frac{\partial f}{\partial t}\right)_{coll} &= \lim_{\Delta t \to 0} \frac{1}{\Delta t}\left(f\left(\boldsymbol{x} + \frac{\boldsymbol{p}}{m}\Delta t, \boldsymbol{p} + \boldsymbol{F}\Delta t, t + \Delta t\right) - f(\boldsymbol{x}, \boldsymbol{p}, t)\right) \\ &= \lim_{\Delta t \to 0} \frac{1}{\Delta t}\left(\left(\frac{\boldsymbol{p}}{m} \cdot \nabla_{\boldsymbol{x}} f + \boldsymbol{F} \cdot \nabla_{\boldsymbol{p}} f + \frac{\partial f}{\partial t}\right)\Delta t + o(\Delta t^2)\right) \end{aligned} \tag{H.4}$$

This gives the Boltzmann transport equation as:

$$\left(\frac{\partial f}{\partial t}\right)_{coll} = \frac{\boldsymbol{p}}{m} \cdot \nabla_{\boldsymbol{x}} f + \boldsymbol{F} \cdot \nabla_{\boldsymbol{p}} f + \frac{\partial f}{\partial t} \tag{H.5}$$

The Boltzmann transport equation can also be expressed with the Einstein notation as:

$$(\partial_t f)_{coll} = \partial_t f + \frac{p_i}{m}\partial_{x_i} f + F_i \partial_{p_i} f \tag{H.6}$$

For a specific system, physical quantities are easily calculated through integrals of the probability density function, for example:

$$n(\boldsymbol{x}, t) = \int f(\boldsymbol{x}, \boldsymbol{p}, t) d^3 p \tag{H.7}$$

$$\rho(\boldsymbol{x}, t) = mn \tag{H.8}$$

$$\langle A \rangle = \frac{1}{n} \int A f(\boldsymbol{x}, \boldsymbol{p}, t) d^3 p \tag{H.9}$$

Assuming arbitrary $g \equiv g(\boldsymbol{p})$, both sides of Equation H.6 are multiplied by g and then integrated over the momentum space:

$$\partial_t(n\langle g \rangle) + \frac{1}{m}\partial_{x_i}(n\langle g p_i \rangle) - nF_i \langle \partial_{p_i} g \rangle = \partial_t(n\langle g \rangle)_{coll} \tag{H.10}$$

Next, the conservation equations can be derived as follows: First, when assuming $g = m$, the density conservation equation is derived as:

$$\partial_t \rho + \partial_{x_i}(\rho v_i) = (\partial_t \rho)_{coll} \tag{H.11}$$

Since, momentum and velocity are defined as $\boldsymbol{p} \equiv m\boldsymbol{u}$, $\boldsymbol{v} \equiv \langle \boldsymbol{u} \rangle = \frac{1}{m}\langle \boldsymbol{p} \rangle$, by assuming $g = \boldsymbol{p} = m\boldsymbol{u}$, the momentum conservation equation is derived as:

$$\partial_t(\rho v_i) + \partial_{x_j}\left(P_{ij} + \rho v_i v_j\right) - nF_i = \partial_t(\rho v_i)_{coll} \tag{H.12}$$

Where:

$$P_{ij} = \rho\langle (u_i - v_i)(u_j - v_j) \rangle \tag{H.13}$$

Additionally, by assuming $g = \frac{1}{2}m\boldsymbol{u}^2$, the energy conservation equation is given by the following equation.

$$\partial_t\left(\varepsilon + \frac{1}{2}\rho v_i^2\right) + \partial_{x_i}\left(Q_i + \varepsilon v_i + \frac{1}{2}\rho v_i v_j v_j + P_{ij}v_j\right) - nF_i v_i$$
$$= \partial_t\left(\varepsilon + \frac{1}{2}\rho v_i^2\right)_{coll} \tag{H.14}$$

Where:

$$\varepsilon = \frac{1}{2}\rho\langle(u_i - v_i)(u_i - v_i)\rangle \tag{H.15}$$

$$Q_i = \frac{1}{2}\rho\langle(u_i - v_i)(u_j - v_j)(u_j - v_j)\rangle \tag{H.16}$$

Moreover, given the definition of $\xi \equiv \varepsilon/\rho + \frac{1}{2}\boldsymbol{v}^2$, the energy conservation equation can be rearranged into the following form:

$$\partial_t(\rho\xi) + \partial_{x_i}\left(Q_i + \rho\xi v_i + P_{ij}v_j\right) - nF_i v_i = \partial_t(\rho\xi)_{coll} \tag{H.17}$$

The other two can be derived as:

$$\partial_t v_i + \frac{1}{\rho}\partial_{x_j}P_{ij} + v_j\partial_{x_j}v_i - \frac{F_i}{m} = (\partial_t v_i)_{coll} \tag{H.18}$$

$$\partial_t\xi + v_i\partial_{x_i}\xi + \frac{1}{\rho}\partial_{x_i}\left(P_{ij}v_j\right) + \frac{1}{\rho}\partial_{x_i}Q_i - \frac{F_i v_i}{m} = (\partial_t\xi)_{coll} \tag{H.19}$$

Especially, for Equation H.19, it can be further simplified as:

$$\partial_t\frac{\varepsilon}{\rho} + v_i\partial_{x_i}\frac{\varepsilon}{\rho} + \frac{1}{\rho}P_{ij}\partial_{x_i}v_j + \frac{1}{\rho}\partial_{x_i}Q_i = \left(\partial_t\frac{\varepsilon}{\rho}\right)_{coll} \tag{H.20}$$

Based on the general Boltzmann transport Equation H.6, distribution function of electrons under Lorentz force can be expressed as:

$$(\partial_t f)_{coll} = \partial_t f + \frac{p_i}{m}\partial_{x_i}f + eE_i\partial_{p_i}f \tag{H.21}$$

Where magnetic field is neglected. The conservation equations for density, momentum and energy, are derived as:

$$\partial_t \rho + \partial_{x_i}(\rho v_i) = (\partial_t \rho)_{coll} \tag{H.22}$$

$$\partial_t v_i + v_j \partial_{x_j} v_i + \frac{1}{\rho}\partial_{x_j} P_{i\,j} - \frac{eE_i}{m} = (\partial_t v_i)_{coll} \tag{H.23}$$

$$\partial_t \xi + v_i \partial_{x_i} \xi + \frac{1}{\rho}\partial_{x_i}\left(P_{ij} v_j\right) + \frac{1}{\rho}\partial_{x_i} Q_i - \frac{eE_i v_i}{m} = (\partial_t \xi)_{coll} \tag{H.24}$$

Generally, metals have parameters as:

$$P_{ij} = n(T_e) k_B T_e \delta_{ij} \tag{H.25}$$

$$E_i = \beta(T_e)\partial_{x_i} T_e \tag{H.26}$$

$$(\partial_t v_i)_{coll} = -\frac{v_i}{\tau_k} \tag{H.27}$$

The momentum conservation Equation H.23 is rearranged as:

$$\partial_t v_i + v_j \partial_{x_j} v_i + \frac{1}{m}\left[k_B\left(1 + \frac{T_e}{n}\frac{\partial n}{\partial T_e}\right) - e\beta\right]\partial_{x_i} T_e = -\frac{v_i}{\tau_k} \tag{H.28}$$

Given $C_e = \frac{3}{2} n k_B$, the momentum conservation equation can be further expressed as:

$$\partial_t v_i + v_j \partial_{x_j} v_i + \frac{1}{m}\left[k_B\left(1 + \frac{T_e}{C_e}\frac{\partial C_e}{\partial T_e}\right) - e\beta\right]\partial_{x_i} T_e = -\frac{v_i}{\tau_k} \tag{H.29}$$

Assuming temperature dependence of energy $\xi = \frac{3k_B T_e}{2m} + \frac{v_i^2}{2}$, and temperature change due to collision $(\partial_t T_e)_{coll} = -\frac{T_e - T_l}{\tau_{e-p}}$, where τ_{e-p} is the characteristic time for electrons and phonons to reach equilibrium, the energy conservation Equation H.24 can be simplified as:

$$\partial_t T_e + v_i \partial_{x_i} T_e + \frac{2}{3} T_e \partial_{x_i} v_i + \frac{1}{C_e}\partial_{x_i} Q_i = -\frac{T_e - T_l}{\tau_{e-p}} \tag{H.30}$$

Interaction constant G is defined as $G \equiv C_e/\tau_{e-p}$. The final energy conservation relation is derived with an additional source term as:

$$C_e \partial_t T_e = -\partial_{x_i} Q_i - G(T_e - T_l) + S(\boldsymbol{x}, t) - C_e \left(v_i \partial_{x_i} T_e + \frac{2}{3} T_e \partial_{x_i} v_i \right) \quad \text{(H.31)}$$

Thus, the semi-classical two-temperature model is given by the following equations:

$$C_e \frac{\partial T_e}{\partial t} = -\nabla \cdot \boldsymbol{Q}_e - G(T_e - T_l) + S(\boldsymbol{x}, t) - C_e \left(\boldsymbol{v} \cdot \nabla T_e + \frac{2}{3} T_e \nabla \cdot \boldsymbol{v} \right) \quad \text{(H.31)}$$

$$\frac{\partial \boldsymbol{v}}{\partial t} + \boldsymbol{v} \cdot \nabla \boldsymbol{v} + \frac{1}{m} \left[k_B \left(1 + \frac{T_e}{C_e} \frac{\partial C_e}{\partial T_e} \right) - e\beta \right] \nabla T_e = -\frac{\boldsymbol{v}}{\tau_k} \quad \text{(H.29)}$$

$$\tau_e \frac{\partial \boldsymbol{Q}_e}{\partial t} + \boldsymbol{Q}_e = -K_e \nabla T_e \quad \text{(H.32)}$$

$$C_l \frac{\partial T_l}{\partial t} = -\nabla \cdot \boldsymbol{Q}_l + G(T_e - T_l) \quad \text{(H.33)}$$

$$\tau_l \frac{\partial \boldsymbol{Q}_l}{\partial t} + \boldsymbol{Q}_l = -K_l \nabla T_l \quad \text{(H.34)}$$

Where the red parts indicate the additional terms compared to the phenomenological two-temperature model.